Multi-wavelength study of neutron stars in the Magellanic Clouds

Johanna Titus

January 2020

VJRJOH004

A thesis submitted in fulfilment for the
degree of Doctor of Philosophy
in
Astronomy

Department of Astronomy
UNIVERSITY OF CAPE TOWN

Supervisors: A/Prof. Vanessa McBride, Prof. Benjamin Stappers, Dr David Buckley

University of Cape Town

University of Cape Town

The copyright of this thesis vests in the author. No quotation from it or information derived from it is to be published without full acknowledgement of the source. The thesis is to be used for private study or non-commercial research purposes only.

Published by the University of Cape Town (UCT) in terms of the non-exclusive license granted to UCT by the author.

Abstract

Massive stars are essential drivers of galaxy evolution, as well as the synthesis of heavier elements, enriching the interstellar and intergalactic medium with metals through every cycle of star formation. Thus to understand the evolving universe, it is essential to quantify the formation and evolution of massive stars in different environments. Most massive stars are born in binaries, as such their evolution are significantly affected by episodes of mass transfer. In this thesis I explore neutron stars, one of the endpoints of massive stars' evolution, in a bid to further understand the effects of binarity on evolution. To start, I conduct an optical spectroscopic and timing study of candidate X-ray binaries in the Large Magellanic Cloud (LMC), resulting in a 50% increase in the confirmed population of accreting neutron stars in the LMC. Following this study, I carry out a targeted radio pulsar search in the Small Magellanic Cloud (SMC), leading to the discovery of new pulsars, corresponding to a population size increase of 40%. The new radio pulsars allow for further characterisation of the SMC pulsar population. To relate these observational incarnations of neutron stars (i.e. radio pulsars and accreting X-ray pulsars), I utilise a binary population synthesis code that enables the prediction of pulsars in the SMC under the assumption that all pulsars are products of massive binary evolution. The simulations successfully reproduce the observed radio pulsar population of the SMC. Ultimately, pairing observational results with simulations can establish practical guidelines for future surveys, and provide a basis for using different observed populations of neutron stars to constrain binary interactions and evolution.

Acknowledgements

I would like to express my deepest gratitude to my supervisors. Without their support and guidance, the completion of my thesis would not be possible. Dr Vanessa McBride, I am incredibly grateful that you always considered what I hoped to accomplish and helping me achieve my goals. I appreciate your encouragement, support, and guidance throughout my post-graduate career. Prof. Benjamin Stappers, I am thankful for your commitment to my development as an academic, and the opportunity you gave me to work alongside a wonderful pulsar group. To Dr David Buckley, I appreciate the conversations and insights during my project, as well as the introductions to potential collaborators. I would also like to thank Dr Silvia Toonen for her invaluable contribution during the last portion of my PhD.

Developing my writing proficiency would not have been possible without the UCT Astronomy writing circle led by Prof. Kate le Roux. I appreciate all the comments on my work, and the opportunity to read the writing of others. Thank you to all the writing circle members.

I wish to thank the SAAO for funding my PhD project, as well as Roslyn Daniels at UCT for assisting me with any queries. I also want to thank Kate Parsons and Michelle Brand for giving me a home away from home while I was in Manchester. I am incredibly grateful to you both for your thoughtfulness and care.

I extend my gratitude to my friends and family for their continuous support. It is often difficult to relate the struggles a PhD brings to people outside academia. Therefore, I would like to thank my old office mates, Julia and Jamie, for good conversations and sharing in the good and bad moments throughout my PhD. I also thank Vu, Carmen, and Nicole for helping me adjust to life in Cape Town, and your precious friendship. Riana and Frits, I am eternally grateful for your continuous support and kindness. To my parents and grandparents, thank you for loving me unconditionally and believing in me. I thank my brother for his financial support during my university career, and his valuable advice. Finally, I want to thank my husband for his patience, kindness, and extraordinary selflessness during the last two years. I am forever grateful for you, and love you to the Magellanic Clouds and back.

Declaration of Authorship

The work presented in this thesis was done under the supervision of Dr V. McBride, Prof. B. Stappers, Dr D. Buckley, and in collaboration with various people who provided data, and contributed to the analysis and discussion. This thesis contains research that has been published or submitted for publication:

Chapter 2: N. van Jaarsveld (Maiden name), D.A.H. Buckley, V.A. McBride, F. Haberl, G. Vasilopoulos, C. Maitra, A. Udalski, B. Miszalski, "*Identification of High Mass X-ray Binaries selected from XMM-Newton observations of the LMC*", 2018, MNRAS, 475, 3253 – 3261.

This chapter has been published in the Monthly Notices of the Royal Astronomical Society Journal (impact factor: 9). We conducted optical follow up studies of 19 Be/X-ray binaries candidates. The optical follow up studies included Hα spectra from Southern African Large Telescope (SALT), I band Optical Gravitational Lensing Experiment (OGLE) light curves, and blue spectra from the 1.9 m telescope in Sutherland. I have done the reduction and analysis of the Hα and blue spectra, as well as the timing study of the OGLE light curves. I wrote all the sections of the paper, except for section 2.1 which was written by Frank Haberl, and a portion of section 4.5 which was written by Brent Miszalski. From the optical studies we confirmed 9 new Be/X-ray binaries in the LMC.

Chapter 3: N. Titus, B.W. Stappers, V. Morello, M. Caleb, M.D. Filipovic, V.A. McBride, W.C.G. Ho, D.A.H. Buckley, "*Targeted search for young radio pulsars in the SMC: Discovery of two new pulsars*", 2019, MNRAS, 487, 4332 – 4342.

This chapter has been published in the Monthly Notices of the Royal Astronomical Society Journal (impact factor: 11). We carried out deep Parkes observations of 6 supernova remnants in the Small Magellanic Cloud to search for radio pulsars. I wrote an automated Python pipeline that wraps around PRESTO (pulsar searching software) to search the radio data for pulsars. I also wrote a pipeline for a fast folding algorithm (FFA) to search for longer period pulsars. I carried out the pulsar searching, as well as the various sensitivity calculations. I applied for the telescope time and made the observations. I wrote all the sections of the paper, except for section 2.1 which was mostly written by David Buckley. This work discovered two new radio pulsars in the SMC.

Chapter 4: N. Titus, S. Toonen, V.A. McBride, B.W. Stappers, D.A.H. Buckley, "*The radio pulsar population of the Small Magellanic Cloud*", submitted on 9 January 2020.

This chapter has been submitted to the Monthly Notices of the Royal Astronomical Society Journal. I carried out population synthesis studies with a binary population synthesis code called SeBa to recover the observed radio pulsar population of the SMC and predict the number of pulsars MeerKAT will detect during the approved TRAPUM survey. I personally executed the simulations, wrote the reduction pipeline, and did the analysis. I wrote all the sections of the paper.

Each of these chapters contain all the necessary information and can be read independently.

I confirm that I have been granted permission by the University of Cape Town's Doctoral Degrees Board to include the following publication(s) in my PhD thesis, and where co-authorships are involved, my co-authors have agreed that I may include the publication(s):

Chapter 2: N. van Jaarsveld (Maiden name), D.A.H. Buckley, V.A. McBride, F. Haberl, G. Vasilopoulos, C. Maitra, A. Udalski, B. Miszalski, "*Identification of High Mass X-ray Binaries selected from XMM-Newton observations of the LMC*", 2018, MNRAS, 475, 3253 – 3261.

Chapter 3: N. Titus, B.W. Stappers, V. Morello, M. Caleb, M.D. Filipovic, V.A. McBride, W.C.G. Ho, D.A.H. Buckley, "*Targeted search for young radio pulsars in the SMC: Discovery of two new pulsars*", 2019, MNRAS, 487, 4332 – 4342.

Chapter 4: N. Titus, S. Toonen, V.A. McBride, B.W. Stappers, D.A.H. Buckley, "*The radio pulsar population of the Small Magellanic Cloud*", submitted on 7 January 2020.

SIGNATURE: J. Titus
DATE: 28 January 2020
STUDENT NAME: Johanna Titus
STUDENT NUMBER: VJRJOH004

Plagiarism Declaration

I, Johanna Titus, know the meaning of plagiarism and declare that all of the work in the document, save for that which is properly acknowledged, is my own.

Date:	**Signed:**
28 January 2020	Signed by candidate

Contents

List of Figures

List of Tables

Chapter 1

Introduction

Since the early universe massive stars have been driving galaxy evolution by means of radiative and supernova (SN) feedback, enriching the interstellar medium (ISM) and intergalactic medium (IGM) with heavy elements. They also provide massive shocks to the ISM, aiding the formation of H_2 regions and the collapse of gas and dust clouds initiating further star formation (Loren et al. 1973, Talbot 1980, Kennicutt 1989, Wong & Blitz 2002). Thus understanding the evolution of massive stars in different environments and various galaxies with potentially different initial mass functions and other properties is crucial if we hope to understand our evolving universe.

1.1 Massive binary evolution

Recent star formation episodes (SFEs) produce massive O and B stars. Given that most massive stars occur in binaries (Sana et al. 2012; 2014) it is essential to consider the effect of binarity on their evolution. Mass transfer, in particular, has a significant impact on stars, and can lead to the formation of unique stellar products.

The following description of massive binary evolution highlights the relevant channels that favour the formation of neutron stars (NSs), and is depicted in Figure 1.1. Although the described channels will likely result in the formation of NSs, black holes (BHs) also form occasionally, and consequently affect the evolution of the binary. The conditions leading to the formation of either a BH or a NS depends on the massive star's initial mass, mass loss through stellar winds, metallicity (Fryer & Kalogera 2001, Heger et al. 2003), binarity (Linden et al. 2010), angular momentum (Georgy et al. 2009), nucleosynthesis, and neutrino transport for supernovae (Sukhbold et al. 2016). BHs in particular, are predicted to form when the

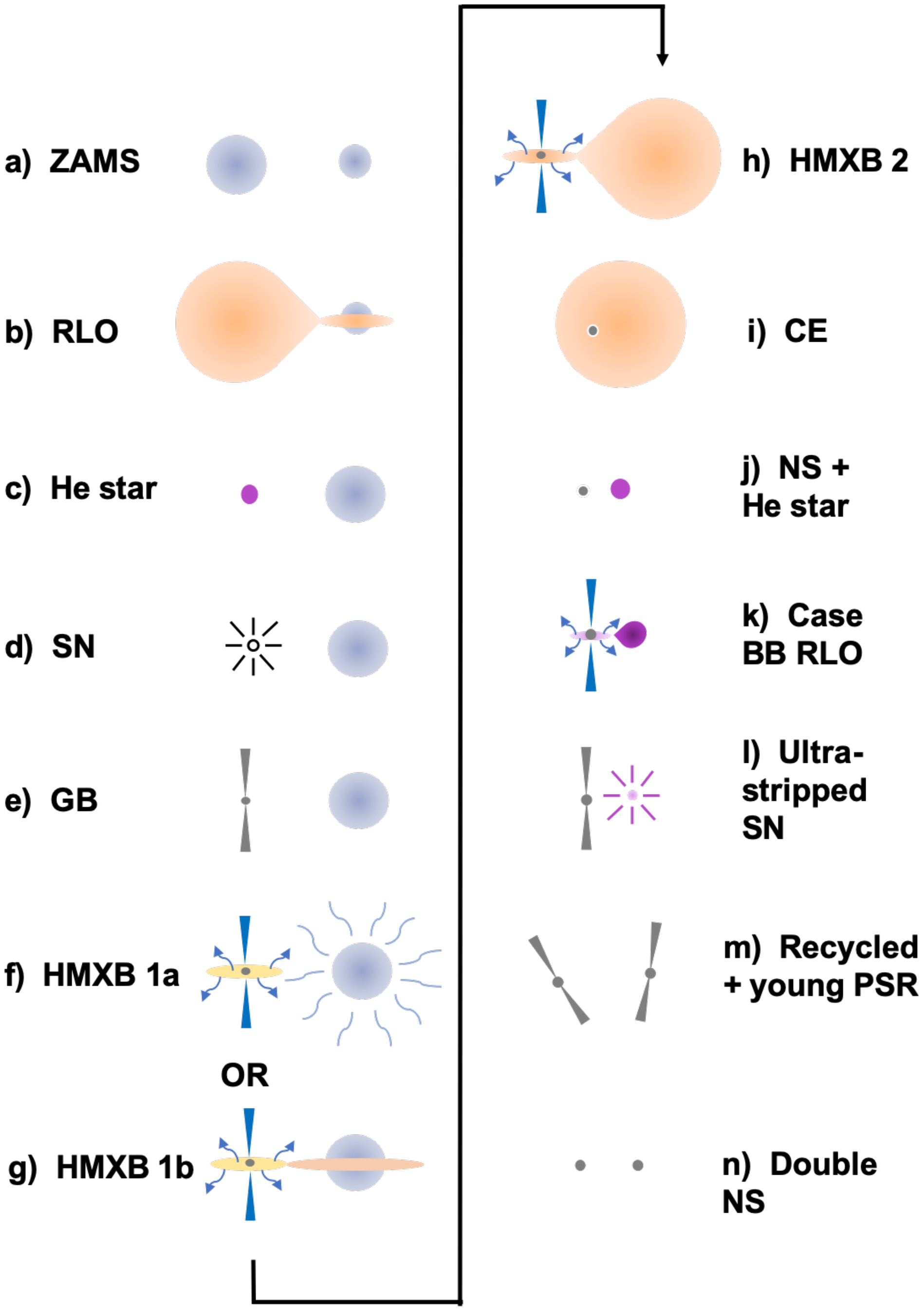

Figure 1.1: The evolution of massive binaries (adapted from Tauris et al. 2017). The zero age main sequence (*ZAMS*) stars are both OB stars. Here follows a list of abbreviations used: b) Roche lobe overflow – *RLO*; c) Helium star – *He star*; d) supernova – *SN*; e) gamma-ray binary – *GB*; f-h) high mass X-ray binary – *HMXB*; i) common envelope – *CE*; j) neutron star - He star binary – *NS + He star*; k) Binary of recycled and young radio pulsar – *Recycled + young PSR*.

initial star's mass exceeds 25 $M_\odot$ for a variety of metallicities (Heger et al. 2003). This prediction is limited to single stars, since mass transfer in a binary is complex and not trivial to solve.

If a binary consists of a pair of OB stars (Figure 1.1, a), the more massive star evolves faster and eventually fill its Roche lobe. The Roche lobe is defined as a equipotential surface (Figure 1.2) beyond which particles will no longer be gravitationally bound to the star (see Leahy & Leahy 2015 and references therein). Once the star fills its Roche lobe, mass and angular momentum are transferred to the companion via the inner Lagrange point (L_1), resulting in a spun-up companion (Figure 1.1, b). When the donor's hydrogen envelope is stripped a helium-rich core will remain. This core is also known as a He-star (Figure 1.1, c). If the He-star results in a core-collapse SN (Type Ib/c; Yoon et al. 2010) a NS will likely form. Core-collapse SN occur in high mass stars once the core is iron, and hence fusion can no longer provide energy. At this point insufficient radiation pressure is produced to balance the effect of gravity, and so the core contracts until the free electrons are captured by heavy nuclei and protons. Up to now the core has been supported by the free electrons through electron degeneracy pressure, however with their capture the electron degeneracy pressure is overcome and the core collapses producing shock waves, expelling the stars envelope. The initial SN will disrupt 80% of binaries (Eldridge et al. 2011), leading to both isolated OB stars (and in some cases, runaway) and NSs.

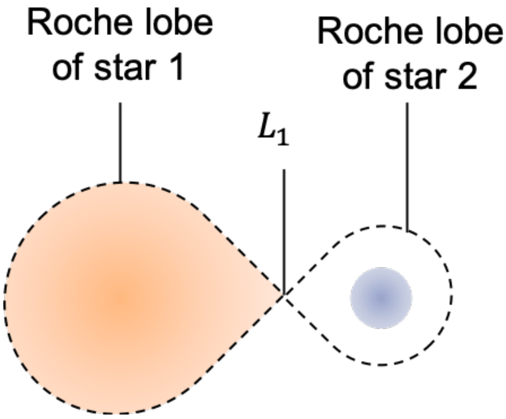

Figure 1.2: Roche lobe geometry of binary system where the more massive star 1 is filling its Roche lobe, and transferring mass to star 2 (not filling its Roche lobe) via the inner Lagrange point (L_1).

1.1.1 Radio pulsars

A NS can emit coherent, highly beamed radio emission if its spin period is fast enough and magnetic field is sufficiently strong (see Figure 1.4). Such NSs are referred to as radio pulsars. Since the first radio pulsar discovery by Hewish et al. (1968), numerous observational and theoretical campaigns have been undertaken to shed light on the physical processes producing the radio pulsar emission. Despite the dedication of many astronomers, the exact mechanism producing the highly beamed, coherent radio emission is still poorly understood; nonetheless a generic radio pulsar model has emerged. A radio pulsar can be modelled as a rotating magnetic dipole with a misaligned magnetic and rotational axis radiating energy. A magnetospheric plasma is generated by the pulsar's magnetic field and the extraction of charged particles from the NS surface. The charged particles are accelerated along the magnetic field lines, producing radio emission (see Gurevich & Istomin 2007 and references therein). With the plasma magnetically threaded, it co-rotates with the rapidly spinning NS. Co-rotation is maintained to a maximum radius where the plasma's speed is equal to the speed of light. This threshold defines a theoretical surface known as the *light cylinder* (Figure 1.3). The light cylinder divides the dipolar magnetic field into closed and open magnetic field line regions. The closed lines occur within the light cylinder where the plasma's speed does not exceed the speed of light. The field lines penetrating the light cylinder remain open to prevent the plasma from exceeding the speed of light, and defines the polar cap of the NS. Consequently, the charged particles accelerating from the polar cap along the open field lines allow for the formation of the observed, highly beamed coherent synchrotron radio emission.

Observations of isolated radio pulsars suggests that they will spin down, and lose their ability to generate radio emission within ~100 Myr (Faucher-Giguère & Kaspi 2006). Figure 1.4 is a canonical period – period derivative ($P-\dot{P}$) diagram, showing the parameter space within which the radio pulsar mechanism is active. Isolated radio pulsars evolve diagonally across from the top left to the bottom right of the $P-\dot{P}$ diagram as they spin down. Radio pulsars in binaries can go through a mass accretion phase that spins them up to millisecond spin periods (i.e. recycled millisecond pulsars) and are located in the bottom left corner of the $P-\dot{P}$ diagram. It also shows one possible *death line* determined by Bhattacharya et al. (1992) followed by the *graveyard* region (grey shaded region in Figure 1.4) where a NS cannot produce beamed radio emission. The radio emission ceases when the potential drop supported by the NS's magnetosphere is no longer sufficient to strip charge particles from the surface of the NS (Ruderman & Sutherland 1975).

Young radio pulsars are often associated with SN remnants (SNRs), and subsequently pulsar wind nebulae (PWNe) if their magnetic fields are of the order $\sim 10^{12} - 10^{13}$ G (Gaensler & Slane 2006). PWNe are powered by a central pulsar, generating a magnetised particle wind whose ultra-relativistic electrons and positron radiate synchrotron emission across the entire electromagnetic spectrum (Goldreich & Julian 1969, Pacini & Salvati 1973, Rees & Gunn 1974, Kennel & Coroniti 1984). The expanding pulsar wind creates a shock front when it collides

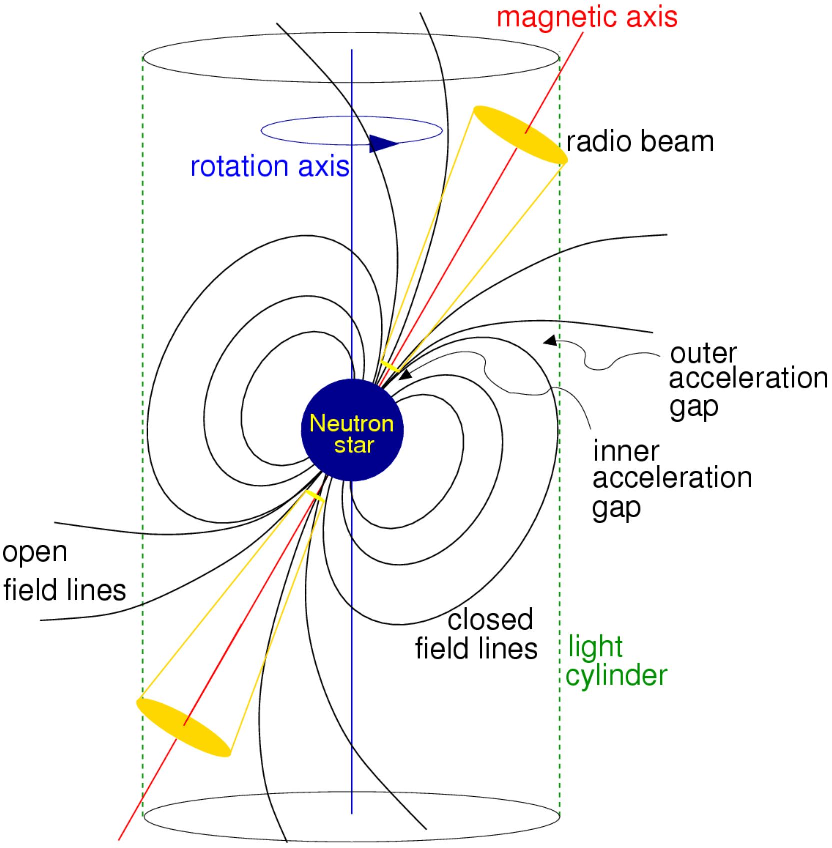

Figure 1.3: Canonical radio pulsar model of a rapidly rotating magnetic dipole (Lorimer & Kramer 2012).

with the ISM and forms a PWN in its wake emitting X-rays and radio emission.

1.1.2 Gamma-ray binaries

About ∼20% of all binaries survive the initial SN (Figure 1.1, d). The surviving binaries consist of rapidly spinning radio pulsar and massive companion. At this stage the binaries are thought to enter the gamma-ray binary (GB, Figure 1.1,e) phase during which the binaries emit radiation across the entire electromagnetic spectrum, peaking in the gamma-rays beyond 1 Mev. Initially the propeller effect (Illarionov & Sunyaev 1975) causes a centrifugal barrier produced by the rotating magnetosphere of the neutron star and prevents material from accreting onto the surface of the rapidly spinning young pulsar. At this point the pulsar will spin down dramatically due to substantial energy losses from the relativistic pulsar wind Figure 1.5). However, the stellar wind and radiation field of the OB companion will impose an additional torque on the pulsar's

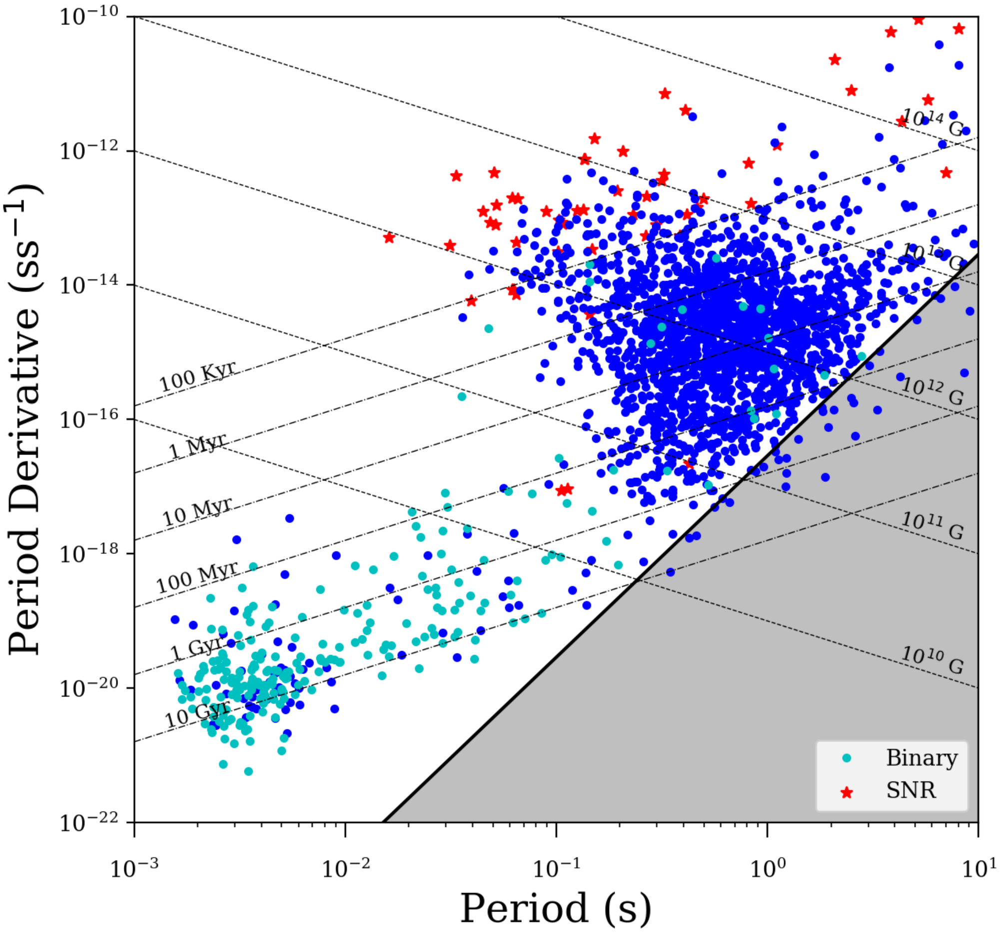

Figure 1.4: The canonical $P-\dot{P}$ diagram for radio pulsars showing constant characteristic age lines, as well as lines representing the minimum surface magnetic field of a radio pulsar. The red stars show radio pulsar, supernova remnant associations, the blue markers show isolated radio pulsars, and the cyan markers show the binary pulsars. The diagram shows the period (P), and period derivative ($\dot{P}$) regime that allows the formation of radio beams. Conversely, the black line shows a pulsar *death line* (Bhattacharya et al. 1992) followed by the grey region that highlights the graveyard region where the parameters are not favourable for the formation of radio beams. (Manchester et al. 2005; https://www.atnf.csiro.au/research/pulsar/psrcat).

magnetosphere, causing it to spin down further via electromagnetic braking. The interaction between the energetic pulsar wind particles and the OB companion generates non-thermal radiation across the whole electromagnetic spectrum generating a "binary pulsar wind nebula".

There is some evidence for the binary pulsar wind nebula scenario, although radio pulsations have not been detected in most GBs. The absence of the radio pulsations is likely a result of scattering caused by the stellar winds of the massive companions (Dubus 2013). The two GBs that show radio pulsations (PSR B1259−63/LS 2883, Johnston et al. 1992; and PSR J2032+4127/MT91 213, Lyne et al. 2015;) have extremely wide, eccentric orbits with orbital periods of ~3 (Wang et al. 2004) and ~40 years (Ho & Andersson 2017) respectively, which could be the reason radio pulsations are detected. In the absence of radio pulsations it is extremely difficult to determine if the compact object is a NS or a BH, since GBs can also be powered by non-thermal jet emission from an accreting BH (Massi et al. 2017). Dynamical determinations of the compact object mass are also challenging in the presence of a massive companion, since the spectral perturbations induced by the orbiting compact object may not easily be resolved. Thus, the nature of most compact objects are unknown. The GB phase is thought to be a short-lived phase (10^5 yr, Figure 1.5), consequently we do not expect to observe many of these binaries. This is consistent with observations, as only seven GBs have been detected to date (Dubus et al. 2017, Paredes & Bordas 2019).

Once the pulsar has spun down sufficiently, it approaches what is known as its equilibrium spin period, where it matches the speed of the in-falling material from the companion. At this point accretion will commence as the binary transitions to the high mass X-ray binary phase.

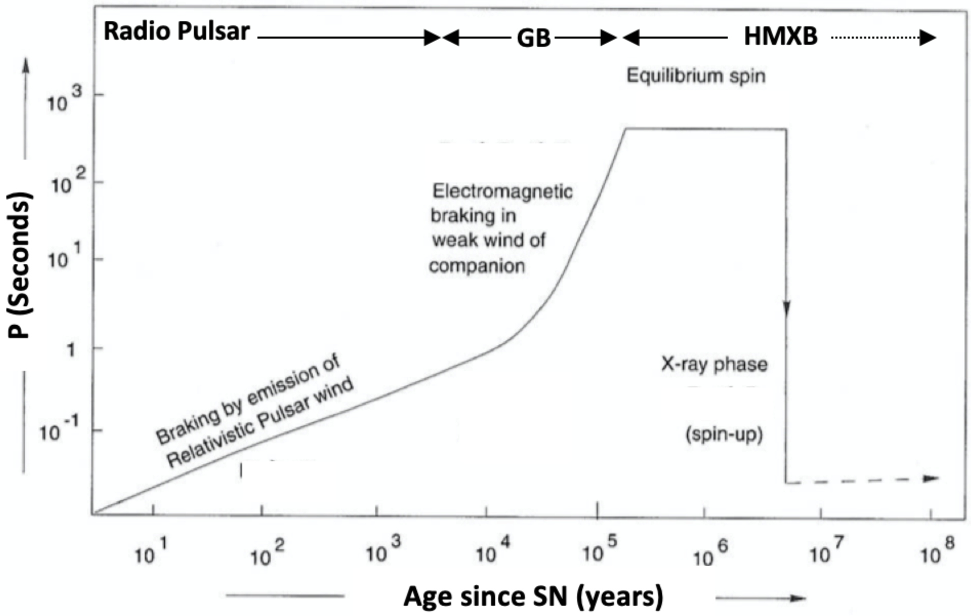

Figure 1.5: The evolution of the spin period of the young NS from a radio pulsar through to the Gamma-ray binary (GB) phase, and finally leading up to the High mass X-ray binary (HMXB) phase (adapted from Padmanabhan 2001).

1.1.3 High mass X-ray binaries

Following the GB phase the binary transitions to the high mass X-ray binary (HMXB) phase when the ram pressure of the in-falling matter overcomes the pulsar wind. The in-falling material can form an accretion disc, or alternatively, be threaded directly along the magnetic field lines onto the magnetic poles of the NS producing beamed X-ray emission (Pringle & Rees 1972). All HMXBs harbour NSs, except for the five BH HMXBs, namely Cygnus X-1 (Gies & Bolton 1986, Orosz et al. 2011), LMC X-3 (Hutchings et al. 1983; 1987), M 33 X-7, MWC 656 (Casares et al. 2014), LB-1 (Liu et al. 2019). The presence of a BH can alter the evolution of the binary significantly, and is explored in Section 4.2.2. The remainder of this section assumes the compact object is a NS, however the description also applies to the atypical BH HMXBs.

HMXBs include Be/X-ray binaries (BeXBs) and supergiant X-ray binaries (SGXBs). BeXBs (Figure 1.1, g) are transient X-ray sources ($L_X \sim 10^{36} - 10^{38}$ erg s^{-1}, Charles & Coe 2006)*, and typically consist of a NS in a wide ($P_{orb} > 15$ days), eccentric orbit around an emission line, non-supergiant Oe or Be companion. Although, the companions are known to have late O or early B spectral types, the majority have spectral types of B0 – B1 (Negueruela & Coe 2002, Coe et al. 2005, McBride et al. 2008, Antoniou et al. 2009, Maravelias et al. 2014). The "*e*" following the spectral type signifies the emission line spectrum of the companion. The emission originates from a circumstellar disc around the star that forms due to its rapid rotation. Packet (1981) showed that a companion would be spun up to near-critical rotation when its mass increases by as little as 5 – 10% during the initial mass transfer. Although the formation of the circumstellar disc is often associated with binary interactions, the OBe phenomena can be explained by two other scenarios: (1) stars born with large rotational velocities; (2) stellar structural changes that occur during the second half of an OB star's main sequence life time, i.e. an evolutionary effect of OB stars.

It is still unclear whether isolated OB stars are born with large rotational velocities or if it is an evolutionary effect. Fabregat & Torrejón (2000) found that the OBe phenomena is completely absent in Galactic clusters younger than 10 Myr, while Keller et al. (2000) found a similar trend for the Magellanic Clouds (MCs). This suggests the OBe phenomenon is related to the stars evolution. Conversely, Zorec & Briot (1997) found that Galactic B field stars are as abundant as Galactic Be field stars, providing no evidence for the evolutionary scenario. To clarify the evolutionary connection to the formation of OBe discs, more detailed studies are required. Although the exact mechanism responsible for the formation of a circumstellar disc is poorly understood, Rivinius et al. (2013) suggested the combination of non-radial pulsations with critical rotation velocities of OBe stars can lead to an equatorial outflow, forming a cir-

---

*The quiescent X-ray luminosity of BeXBs can be as low as 10^{33} erg s^{-1}.

cumstellar discs.

SGXBs are usually persistent X-ray sources in close binaries ($P_{\rm orb} < 40$ days), and occur in two distinct evolutionary stages which relates to the state of the supergiant companion. During the earlier evolutionary stage, the NS accretes material via strong stellar winds with $L_X \sim 10^{36} - 10^{38}$ erg s^{-1} (Chaty et al. 2019), while the companion is well within its Roche lobe (Figure 1.1, f). A subclass of wind-fed SGXBs has been identified, known as super-giant fast X-ray transients (SFXTs) with $L_X \sim 10^{35} - 10^{37}$ erg s^{-1} (Walter et al. 2015). Their unique short-lived, transient X-ray flares (lasting 100 – 10 000 s) are thought to be generated by a young NS accreting material from a supergiant OB star. Walter et al. (2015) suggests that the peculiar X-ray flares associated with SFXTs can be a result of clumpy winds from the companion. Apart from the clumpy winds, SFXTs have similar OB companions, orbital periods, and eccentricities when compared to *classical* SGXBs. The second evolutionary stage of SGXBs occur when the companion evolves and fills its Roche lobe (Figure 1.1, h). During this phase a persistent accretion disc will form around the NS, spinning it up while emitting copious X-rays with $L_X \sim 10^{38}$ erg s^{-1} (Chaty et al. 2019).

The majority of HMXBs are observed as either the BeXBs or wind-fed SGXB (Liu et al. 2005). To date only three Roche lobe overflow (disc fed) systems are known (Cen X-3, SMC X-1, LMC X-4). BeXBs and wind fed SGXBs are more common since these evolutionary stages last longer, while the disc fed systems become dynamically unstable, and can enter a common envelope (CE) phase (van den Heuvel 1976).

1.1.4 Double degenerate binaries

The evolution from the HMXB phase depends on the nature of the compact object and its orbital parameters. If the compact object is a BH, the Roche lobe overflow (RLO) will be stable for both wide and close binaries, avoiding a CE phase altogether (van den Heuvel et al. 2017, Pavlovskii et al. 2017). Such binaries result in the formation of a He-star and consequently a BH, producing a double BH binary. Close NS HMXBs enter a CE phase (Figure 1.1, i), but spiral in and merge with their companions forming hypothesised Thorne-Zytkow stars (Podsiadlowski et al. 1995). Only NS BeXBs with orbital periods exceeding a year are likely to survive the CE phase (Tauris et al. 2017).

The surviving binaries emerge from the CE phase consisting of a NS and a He star (Figure 1.1,j). The system can enter a second RLO phase when the He star fills its Roche lobe (Case BB RLO; Habets 1986, Tauris et al. 2015) if the orbital separation and eccentricity are small enough. The RLO initiates a relatively long phase of accretion onto the NS, producing a spun up, recycled radio pulsar. The resulting He star will end its life through an ultra-stripped SN explosion (Tauris et al. 2013, Suwa et al. 2015, Moriya et al. 2017). Tauris et al. (2017) showed that most binaries survive the second SN, however it depends on the orbital separation, eccentricity and the kick imparted to the newly formed compact object. The resulting double degenerate binary is a potential detectable gravitational wave source provided the orbital period is sufficiently short to spiral in within a Hubble time.

1.2 Magellanic Clouds

To understand how stellar evolution affects a galaxy, it is necessary to study a representative sample of the underlying stellar population. In most cases this is not possible, because of extinction in our Galaxy, or vast distances to other galaxies preventing the resolution of individual stars. However, the Small and Large Magellanic Cloud (SMC & LMC respectively) are close enough (60 & 50 kpc respectively, Graczyk et al. 2014; Pietrzyński et al. 2019) to resolve individual stars, providing an independent astrophysical laboratory outside of the Milky Way. Minimal extinction and known distances make the Magellanic Clouds (MCs) ideal for extensive studies of their stellar populations, and potentially, the environmental impact on star formation (SF, Dray 2006; Walter et al. 2015).

1.2.1 Star formation histories of the Magellanic Clouds

Harris & Zaritsky (2004; 2009) determined the complete global SF history (SFH) of the MCs using the StarFISH SFH reconstruction program (Harris & Zaritsky 2002) with the Magellanic Cloud Photometric Survey (MCPS, Zaritsky et al. 2004) data as an input. They found that approximately 50% of the stellar population of the SMC formed 8.4 Gyr ago, followed by a quiescence period until 3 Gyr ago. During the last 3 Gyr the SMC experienced an epoch of continuous SF with peaks at 2.5 Gyr, 400 Myr and 60 Myr. The SF episodes at 2.5 Gyr, 400 Myr are consistent with perigalactic passages of the Milky Way (MW), that seem to have prompted the respective SF episodes due to tidal interactions. Although some of the SF activity is attributed to perigalactic passages, there is some controversy associated with the MCs orbit around the MW. The general consensus is that the MCs have completed ~2 orbits (Shattow & Loeb 2009, Zhang et al. 2012, Diaz & Bekki 2011; 2012), however Besla (2015) argues the MCs are yet to complete an orbit around the MW. The LMC had a SF episode more than 12 Gyr ago followed by a quiescent epoch until 5 Gyr ago. Since then the SF rate peaked at 2 Gyr, 500 Myr, 100 Myr and 12 Myr ago. The 2 Gyr and 500 Myr SF episodes in the LMC are almost coincident with SF episodes in the SMC, indicating a shared history for at least several Gyr. Figure 1.6 shows the SFH and metallicity evolution of both the MCs.

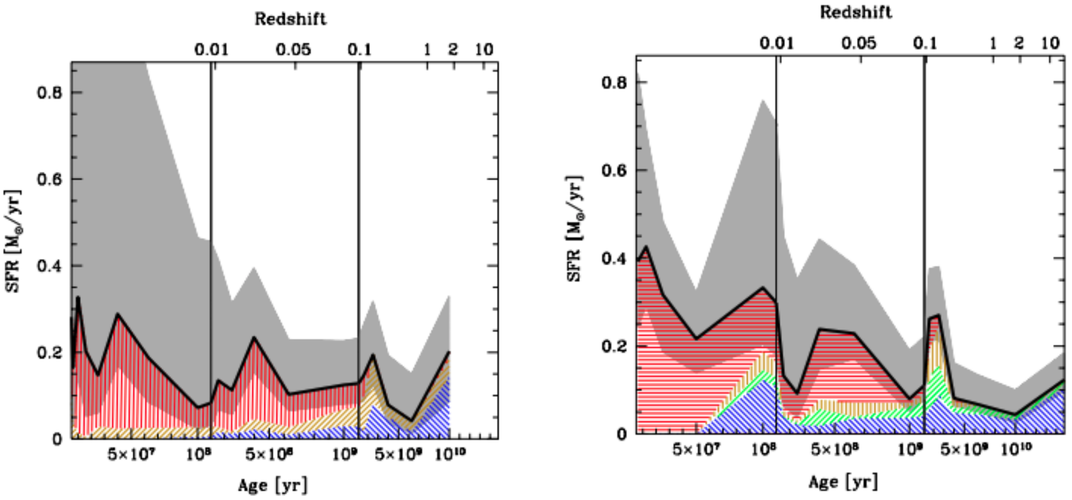

(a) SMC star formation history (Harris & Zaritsky 2004; 2009).

(b) LMC star formation history (Harris & Zaritsky 2009).

Figure 1.6: Magellanic Cloud star formation histories. The SFH is shown on a linear scale with three sections. The left panel highlights the first ~100 Myr, the middle panel extends up to 1~Gyr, while the third panel ends at ~14 Gyr. The best fit to the star formation rate (SFR) is shown with the solid black line, while its uncertainty is indicated by the shaded grey region. The metallicity at each age distribution is shown in blue (Z = 0.001), green (Z = 0.0025), orange (Z = 0.004), and red (Z = 0.008).

The most recent SF episodes (last 100 Myr) produced observable O and B stars. The short life cycles of massive OB stars (~1 – 10 Myr, Figure 1.7) imply that only the most recent SF episodes produce observable massive stars. Moreover, SF episodes also govern the observable post-SN evolutionary phases of massive stars. Various observational campaigns at different wavelengths target particular evolutionary phases of massive binary evolution. In particular radio observations target NSs that are in the radio pulsar phase, while X-ray observations identify accreting X-ray pulsars and BHs in the HMXB phase. Optical timing and spectral studies are often undertaken to identify the main sequence or supergiant companions, and thus infer the nature of the binary itself. Here follows a discussion of the various NS populations in the SMC and LMC.

1.2.2 Small Magellanic Cloud

The SMC has been the subject of many X-ray campaigns searching for SNRs, background active galactic nuclei, and X-ray pulsars. Many X-ray pulsars were identified with Chandra, RXTE, Swift, and XMM-Newton observations. The XMM-Newton telescope surveyed the bar

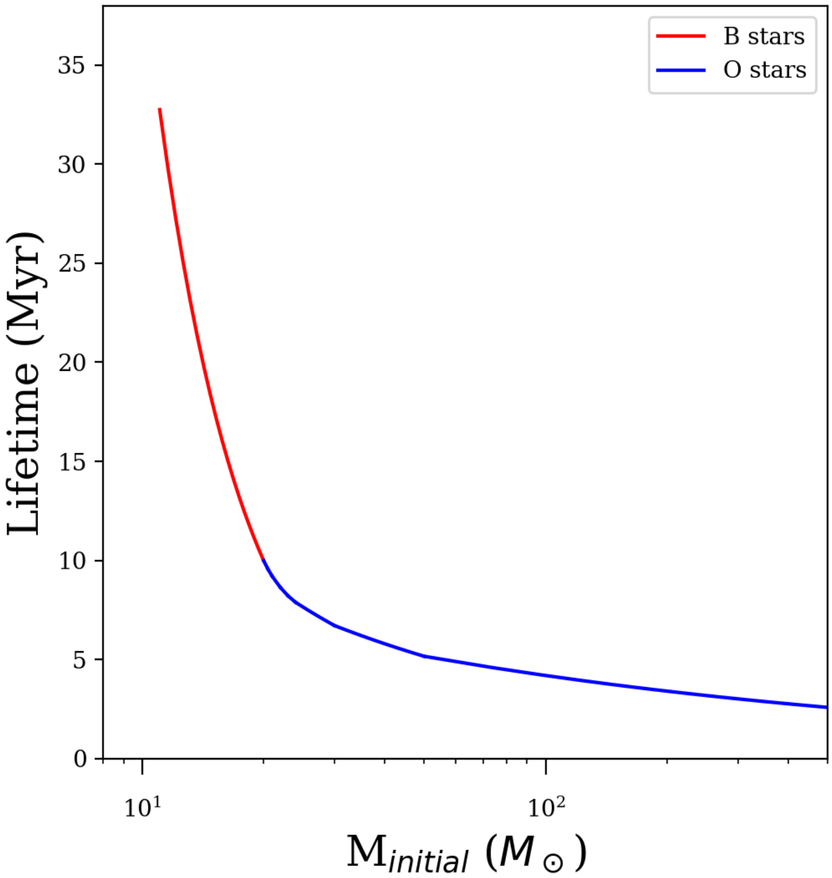

Figure 1.7:]
The lifetime (τ) of isolated massive stars as a function of their initial mass (M) by $\tau \propto M^{1-\alpha}$. For B stars ($\sim 5 < M_\odot < 20$) $\alpha \sim 3$, while O stars ($M > 20\,M_\odot$) have $\alpha \sim 1.3$. This figure is adapted from Yusof et al. (2013).

and eastern wing of the SMC, covering a 5.6 deg^2 area to a limiting point source luminosity of $\sim 10^{33}$ erg s^{-1}. This survey alone yielded 49 new SMC HMXBs (Sturm et al. 2013). In the SMC all HMXBs belong to the BeXB class, except for SMC X–1 belonging to SGXBs. Multiple SMC HMXB catalogues have been published, of which the most recent include the Liu et al. (2005), Coe & Kirk (2015), Haberl & Sturm (2016) and Antoniou et al. (2019) catalogues. The census by Antoniou et al. (2019) identified 137 HMXBs (candidate and confirmed) of which ~60 are confirmed X-ray pulsars. This population is similar to the population in the Milky Way, even though the SMC is only one-fiftieth the mass.

The SFH of the SMC may play the most significant role when considering the number of observed BeXBs. During the initial mass transfer phase of massive binaries (Figure 1.1, RLO), the progenitor Oe/Be companion will be spun up to near-critical rotation velocity, leading to the formation of an equatorial disc within 25 – 80 Myr (McSwain & Gies 2005). Thus, the recent SF episode in the SMC that peaked 60 Myr ago results in the optimal time frame for the detection of Oe/Be stars, and consequently BeXBs. The number of observed HMXBs also scales linearly with a galaxy's SFR (Mineo et al. 2012; 2014, Lehmer et al. 2019), implying that the SMC's SFH can be inferred from its large HMXB population. Another possible explanation for the high number of observed neutron stars in the SMC is its low metallicity when compared to the Milky Way (Dray 2006). Poelarends (2007), Linden et al. (2009) and Linden et al. (2010) showed that electron-capture SNe is a likely outcome for lower mass stars ($<8\ M_\odot$) with lower metallicities, increasing the range of the initial stellar masses required for the formation of neutron stars.

Despite this large population of neutron stars in the SMC only five rotation powered pulsars have been discovered (Table 1.1). To date, three SMC radio pulsar surveys have been carried out. The first was a Parkes survey by McConnell et al. (1991) that resulted in the discovery of one pulsar, PSR J0045−7319. It was found to be in a 51 day orbit around a 16th magnitude B star (Kaspi et al. 1994). In a subsequent SMC survey with the 20 cm Multi-Beam receiver at Parkes, Crawford et al. (2001) discovered PSR J0113−7220, while Manchester et al. (2006) observed a larger region of the SMC and was sensitive to an increased dispersion measure (DM) range, resulting in the discovery of three pulsars (J0045−7042, J0111−7131, J0131−7310). The Manchester et al. (2006) survey is the most complete survey of the SMC, however the large distance to the SMC (~60 kpc) implies that only the brightest pulsars ($L_{1400} > 240\,\mathrm{mJy\,kpc^2}$) were detected, assuming that they have a similar luminosity distribution to the Galactic pulsars (Figure 1.8).

Table 1.1: SMC pulsar parameters with discovery articles.

Pulsar JName	P (ms)	DM (pc cm^{-3})	S_{1400} (mJy)	Discovery Ref.
J0045−7042	632	70	0.11	Manchester et al. (2006)
J0045−7319	926	105	0.30	McConnell et al. (1991)
J0111−7131	688	76	0.06	Manchester et al. (2006)
J0113−7220	325	125	0.40	Crawford et al. (2001)
J0131−7310	348	205	0.15	Manchester et al. (2006)

1.2.3 Large Magellanic Cloud

The first X-ray surveys of the LMC were carried out with the Einstein (Wang & Helfand 1991), and ROSAT (Haberl & Pietsch 1999) X-ray telescopes and they revealed a dozen point sources associated with the LMC. Later on Kahabka (2002) identified 20 – 30 ROSAT point sources

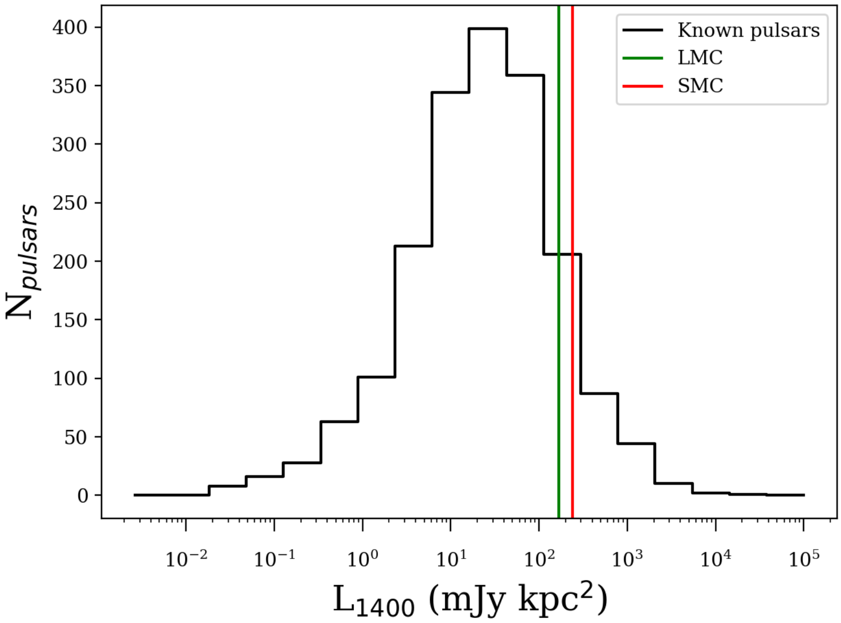

Figure 1.8: The radio luminosity distribution at 1400 MHz of all known Galactic pulsars. The green (LMC) and red (SMC) lines show the limiting luminosities of the Manchester et al. (2006) survey. Data from the ATNF catalogue (Manchester et al. 2005; https://www.atnf.csiro.au/research/pulsar/psrcat).

that have X-ray hardness ratios consistent with X-ray binaries. These X-ray sources had luminosities exceeding 10^{35} erg s^{-1}. Initial XMM-Newton observations uncovered one new HMXB (Haberl et al. 2003), as well as four candidates (Shtykovskiy & Gilfanov 2005). The various surveys have so far uncovered ~40 HMXBs (candidate and confirmed, Antoniou & Zezas 2016) HMXBs.

The relatively small number of detected HMXBs in the LMC is not unexpected since Antoniou & Zezas (2016) showed that the HMXB production rate in the LMC is considerably less efficient than that of the SMC. As mentioned above, the metallicity of the host galaxy influences stellar evolution. Thus, the higher metallicity of the LMC (Z_{LMC} ~0.5 $Z_{\odot}$, Cole 2005) can cause fewer BeXBs to form when compared to a galaxy with a lower metallicity. The SFH of the LMC also plays a role when considering the number of observable HMXBs. The most recent SF episode occurred 12 Myr ago, too recent for the associated O and B stars to form an equatorial disc, and consequently too early for massive binaries to evolve into BeXBs. However, during this SF episode a population of SGXBs and BH-HMXBs could have been formed (Antoniou & Zezas 2016). The second most recent SF episode occurred 100 Myr ago. By this time, the vast majority of the massive binaries would have evolved past the HMXB phase.

The LMC harbours 21 rotation powered radio pulsars (Table 1.2), that were discovered by various Parkes radio telescope observations of the LMC. The McCulloch et al. (1983) survey of the LMC lead to the discovery of its first radio pulsar, while a subsequent survey (McConnell et al. 1991) uncovered two new pulsars (McCulloch et al. 1983, McConnell et al. 1991, Crawford et al. 2001, Manchester et al. 2006, Ridley et al. 2013). The most complete and sensitive radio pulsar survey was carried out by Manchester et al. (2006), and discovered nine new pulsars. Ridley et al. (2013) discovered three new pulsars in a partially completed LMC survey (49 out 209 pointings), while also uncovering five new pulsars by reprocessing archival data. Young, energetic radio pulsars are strong non-thermal X-ray emitters, and can result in the detection of radio pulsars. Two young LMC pulsars associated with SNRs were first detected in the X-rays by the Einstein X-ray observatory (Seward et al. 1984), and the Rossi X-ray Timing Explorer (Marshall et al. 1998). The observed radio pulsar population of the LMC may be related to its SFH. In particular, the SF episodes that occurred 12 and 100 Myr ago produced massive stars, and consequently resulted in the formation of young and old radio pulsars respectively. Although a moderate LMC radio pulsar population has been uncovered, only bright pulsars were detected ($L_{1400} > 160\,\mathrm{mJy\,kpc^2}$). Future, more sensitive surveys are required to uncover more pulsars to understand the underlying properties of the LMC pulsar population.

1.2.4 Thesis overview

The MCs present us with a paradox of sorts. The SMC harbours many HMXBs (~120 candidate and confirmed), and relatively few radio pulsars (5), while the LMC contains few HMXBs (~40 candidate and confirmed) and a relatively large population of radio pulsars (21). The various NS populations of the MCs are likely a result of their unique environment and SFHs. In order to quantify these effects and understand their relevance for massive binary evolution, it is necessary to characterise the observational selection effects of the surveys, including flux limits, coverage and sensitivity to both pulsed and unpulsed emission at different wavelengths.

The SMC has been surveyed in the X-rays to a limiting point source luminosity of $\sim 10^{33}$ erg s^{-1} in the (0.2−4.5) keV band (Sturm et al. 2013). Conversely, the LMC has been surveyed to a limiting point source luminosity of $\sim 10^{35}$ erg s^{-1}[*]. Thus, to make meaningful comparisons between the HMXB populations of the MCs I outline the optical follow-up of an equivalent X-ray survey of the LMC (Sturm et al. 2013) with a limiting point source luminosity of $\sim 10^{33}$ erg s^{-1} in Chapter 2. Chapter 2 describes the detailed optical spectroscopy and timing study that aimed to identify new HMXBs in the LMC.

Although the Manchester et al. (2006) observations of the MCs surveyed both Clouds down to

---

[*] Before Sturm et al. (2013).

Table 1.2: LMC pulsar parameters with discovery articles. Adapted from Ridley et al. (2013).

Pulsar JName	P (ms)	DM (pc cm^{-3})	S_{1400} (mJy)	Discovery Ref.
J0449−7031	479	65	0.14	Manchester et al. (2006)
J0451−67	245	45	0.05	Manchester et al. (2006)
J0455−6951	320	94	0.25	McConnell et al. (1991)
J0456−69	117	103	>0.15	Ridley et al. (2013)
J0456−7031	800	100	0.05	Manchester et al. (2006)
J0457−69	231	91	>0.05	Ridley et al. (2013)
J0458−67	1133	97	>0.07	Ridley et al. (2013)
J0502−6617	691	68	0.25	McConnell et al. (1991)
J0519−6932	263	119	0.32	Manchester et al. (2006)
J0521−68	433	136	>0.12	Ridley et al. (2013)
J0522−6847	674	126	0.19	Manchester et al. (2006)
J0529−6652	975	103	0.30	McCulloch et al. (1983)
J0532−6639	642	69	0.08	Manchester et al. (2006)
J0532−69	574	124	>0.05	Ridley et al. (2013)
J0534−6703	1817	94	0.08	Manchester et al. (2006)
J0535−66	210	75	>0.03	Ridley et al. (2013)
J0535−6935	200	89	0.05	Crawford et al. (2001)
J0537−69	112	273	>0.04	Ridley et al. (2013)
J0537−6910	16	–	–	Marshall et al. (1998)
J0540−6919	50	146	0.02	Seward et al. (1984)
J0542−68	425	97	>0.14	Ridley et al. (2013)
J0543−6851	708	131	0.22	Manchester et al. (2006)
J0555−7056	827	73	0.21	Manchester et al. (2006)

a limiting flux density of 0.12 mJy, the SMC survey sensitivity was reduced by ~30% due to its greater distance. Figure 1.8 shows the limiting luminosities of the Manchester et al. (2006) surveys, illustrating that only ~3% and ~5% of the SMC and LMC pulsar population has been explored respectively, assuming that the Galactic luminosity distribution applies to the MC radio pulsar populations (see Chapter 4). In an attempt to identify more SMC radio pulsars, I conducted a deep, targeted radio pulsar survey of SNRs in the SMC. Chapter 3 defines the survey and the various pulsar searches.

To quantify the selection effects of different radio pulsar surveys I simulate the radio pulsar population of the SMC with a binary population synthesis code. I describe the implementation of the population synthesis code in Chapter 4 and predict the number of observable SMC radio pulsars, as well as the number of pulsars the future MeerKAT survey will detect. In addition to the number of pulsars, I also determine the synthesised primordial HMXB population size.

Chapter 2

Identification of High Mass X-ray Binaries selected from XMM-Newton observations of the LMC

Abstract

The Large Magellanic Cloud (LMC) currently hosts around 23 high mass X-ray binaries (HMXBs) of which most are Be/X-ray binaries. The LMC XMM-Newton survey provided follow-up observations of previously known X-ray sources that were likely HMXBs, as well as identifying new HMXB candidates. In total 19 candidate HMXBs were selected based on their X-ray hardness ratios. In this paper we present red and blue optical spectroscopy, obtained with SALT and the SAAO 1.9-m telescope, plus a timing analysis of the long term optical light curves from OGLE to confirm the nature of these candidates. We find that 9 of the candidates are new Be/X-ray Binaries, substantially increasing the LMC Be/X-ray binary population. Furthermore, we present the optical properties of these new systems, both individually and as a group of all the BeXBs identified by the XMM-Newton survey of the LMC.

2.1 Introduction

High Mass X-ray Binaries (HMXBs) include supergiant X-ray binaries (SGXBs) and Be/X-ray binaries (BeXBs). SGXBs are luminosity class I-II stars, with their mass transfer mechanisms being either Roche lobe overflow or wind accretion. BeXBs making up the largest fraction of HMXBs, having a Oe or Be companion with luminosity class III-V. These stars are either late type O or early B, emission line stars, with the majority having spectral types of B0-B1 (Negueruela & Coe 2002, Coe et al. 2005, McBride et al. 2008). The emission originates from a decretion disc around the star, which formed due to the rapid rotation (rotating at $\gtrsim$75%

(Rivinius et al. 2013) of their critical velocity) of the stars, although the mechanism responsible for the decretion disc formation is poorly understood (Porter & Rivinius 2003).

The Magellanic Clouds (MCs) are our closest neighbouring galaxies. As such they provide an independent astrophysical laboratory outside of the Milky Way, with minimal extinction and known distances. As such they can be used for extensive studies of their stellar populations and, potentially, the environmental impact on star formation (SF, Dray 2006, Walter et al. 2015). We can measure the recent SF rate of the MCs directly by means of their HMXB population, since these massive stars must have formed recently (Grimm et al. 2003). The Small Magellanic Cloud (SMC) contains a large population of HMXBs. A recent census by Antoniou et al. (2019) shows that 137 HMXBs have been identified in the SMC, of which more than 60 show X-ray pulsations indicating the spin period of a neutron star. It provides a comprehensive sample to conduct population synthesis studies to help understand the recent SF, and how the SMC's environment affected it. Conversely, only 40 HMXBs have been identified in the Large Magellanic Cloud (LMC), of which only 23 have been confirmed (Antoniou & Zezas 2016, Vasilopoulos et al. 2016; 2018). With so few confirmed HMXBs in the LMC it is difficult to make comparisons with population synthesis and SF studies. More complete samples of LMC HMXBs will allow one to investigate the effects of metallicity on SF at better spatial resolution scales, by comparing the SF history of the SMC (Z_{SMC} ~0.2 $Z_{\odot}$, Luck et al. 1998) with the LMC (Z_{LMC} ~0.5 $Z_{\odot}$, Cole 2005) and the Milky Way.

Thus in an effort to increase the sample of confirmed LMC HMXBs, we investigate the nature of the optical counterparts of 19 HMXB candidates, some of which were identified by previous surveys (Liu et al. 2005), but with improved positions and hardness ratios from the XMM-Newton survey, as well as new candidates identified by the XMM-Newton survey. We use spectra from the Southern African Large Telescope (SALT) to search for Hα emission from the decretion disc, blue spectra from the SAAO 1.9 m telescope to determine the spectral class of the central star, and finally we conduct a timing analysis using I-band OGLE IV light curves. Based on the X-ray and optical properties we confirm 9 of the candidates as BeXBs. In Section 2.2 we give an overview of the observations, in Section 2.3 we describe the analysis procedures, followed by a discussion of the results in Section 2.4, and a outline of our conclusions in Section 2.5.

2.2 Overview of Observations

2.2.1 XMM data

We selected our targets for optical follow-up spectroscopy from preliminary source detection lists, which we obtained from *XMM-Newton* (Jansen et al. 2001) observations. For our analysis we used the observations from the LMC survey, a very large *XMM-Newton* programme to cover the central part of the LMC (PI: F. Haberl), which included archival, as well as ToO observations up to October 2013 within 4° centred at R.A. = 05h 22m 00s, Dec. = -68° 30′ 00″ (see Figure 2.1 in Maggi et al. 2016). *XMM-Newton* carries three X-ray telescopes with a CCD detetcor − the European Photon Imaging Camera (EPIC-pn, EPIC-MOS; Strüder et al. 2001; Turner et al. 2001, respectively) − in each focal plane. To derive X-ray source detection lists for each observation, we followed the analysis steps of Sturm et al. (2013), applying a maximum likelihood algorithm (EDETECT_CHAIN) from the *XMM-Newton* Science Analysis Software* to images from the three cameras, simultaneously.

Candidates for HMXBs are characterised by hard X-ray spectra, which allows them to be selected using hardness ratios (X-ray colours; Sturm et al. 2013). In addition their optical counterparts are bright (typically V magnitudes between 13 and 17 for stars in the Magellanic Clouds). From our source lists we selected 19 candidates which fulfilled hardness ratio criteria (see below) and had a possible optical counterpart within 5″ with appropriate optical brightness and colours. Finally we added Swift J0513.4−6547, a discovered Be/X-ray binary pulsar (Krimm et al. 2009) to our sample. The target list is presented in Table 2.1 with X-ray properties obtained from re-processing the data with the latest version of SAS (16.1) and including new data, which became available since our first detection run. To improve the X-ray coordinates, we applied astrometric corrections, using a catalogue of background AGN as the reference frame. In contrast to Sturm et al. (2013), we applied background filtering individually for each instrument, which gains exposure time for EPIC-MOS. Candidate 5, originally detected with very low existence likelihood could not be confirmed as an X-ray source and was excluded from the list.

We performed source detection simultaneously on images from the three instruments and the five standard energy bands 0.2−0.5 keV, 0.5−1 keV, 1−2 keV, 2−4.5 keV, and 4.5−12 keV and computed four hardness ratios $HR_i = (R_{i+1} - R_i)/(R_{i+1} + R_i)$, with R_i the inferred source counts in band i. Several of our candidates are detected multiple times. In some cases more than 20 detections are available due to frequent calibration observations undertaken of the supernova remnant N132D or from a monitoring program of Cal 83, a supersoft X-ray source in the LMC.

HR2 and HR3 are listed in Table 2.1 and plotted in Fig. 2.1 and were derived using the sum of counts from all observations covering the source, i.e. represent average hardness ratios. Similarly, average X-ray fluxes are given, which are converted from count rates using conversion factors taken from Sturm et al. (2013). Also X-ray coordinates were computed as

---

*SAS, http://xmm.esa.int/sas/

error-weighted mean and errors (1σ confidence, with a $0.5''$ systematic uncertainty added in quadrature) propagated, when multiple detections are available.

A comparison of the X-ray positions with the positions of the selected counterparts from the Two Micron All Sky Survey (2MASS; Skrutskie et al. 2006), shows agreement better than 2σ for most of the candidates (Table 2.1). The largest discrepancy in X-ray to optical separation is seen for BeCand-18. This is detected as weak source in 24 observations of N132D, in most cases at the rim of the field of view (FoV) with off-axis angles $> 13'$, which results in relatively large positional uncertainties. The large number of observations covering BeCand-18 allowed us to reduce the error considerably (Table 2.1). Also, in two observations the source was located at off-axis angles of $6.3'$ and $8.7'$, which also yield separations of $3.9''$ and $3.1''$, respectively. BeCand-8 and BeCand-9 are also located in the FoV of the N132D observations. BeCand-8 is brighter than the other two candidates and its X-ray and 2MASS position match perfectly, confirming the correct astrometry of these observations. We conclude, that the large discrepancy in X-ray/optical separation for BeCand-18 makes a chance coincidence highly likely.

We took the U, B and V magnitudes of the selected optical counterparts from the Magellanic Clouds Photometric Survey (MCPS; Zaritsky et al. 2004), computed U−B, B−V colours and the reddening-free parameter $Q = U{-}B - 0.72\times(B{-}V)$ which shows typical values of -1.1 to -0.7 for the known Be/X-ray binaries in the Small Magellanic Cloud (SMC; Haberl & Sturm 2016). The distribution of Q values from our candidate sample (Table 2.1) is fully consistent with that of the SMC systems.

2.2.2 SALT Hα spectra

Hα spectra were taken with SALT (Buckley et al. 2006) between January 13 2014 and February 8 2014 , and on October 30 2017 with RSS (Burgh et al. 2003) in longslit mode, using the PG2300 grating with a slit width of $0.6''$, and 2×2 binning, yielding a resolution of ~0.9 Å around Hα. The 2-D product spectra received from the SALT pipeline were reduced with PySALT (Crawford et al. 2010), and wavelength calibrated with a Thorium-Argon lamp. The exposure dates and times for each observation are shown in Table 2.2.

2.2.3 SAAO 1.9 m blue spectra

Blue spectra were taken with the SAAO 1.9 m telescope between November 24 and 29 2016. The observations were carried out with the SpUpNIC spectrograph (Crause et al. 2016), using grating 4 to cover a wavelength range of $\lambda\lambda$3800–5000 Å, with 1×2 binning, yielding a resolution of ~4 Å. Depending on the source brightness and the weather conditions, exposure times ranged from 1200 to 1800 seconds, and were observed multiple times if necessary to produce averaged

Table 2.1: HMXB candidates selected from *XMM-Newton* observations.

Be[a]	*XMM-Newton*							2MASS		X-2M	MCPS
Cand	RA [h m s]	Dec [° ″ ′]	Err [″]	N det	HR2	HR3	Flux [cgs][b]	RA [h m s]	Dec [° ″ ′]	Sep [″]	Q [mag]
1	04 55 46.68	-69 57 21.0	1.47	1	0.66 ± 0.33	0.11 ± 0.23	1.07×10^{-13}	04 55 46.34	-69 57 18.8	2.85	-1.159
2	05 00 46.24	-70 44 35.4	0.50	1	0.41 ± 0.01	0.15 ± 0.01	1.13×10^{-11}	05 00 46.05	-70 44 36.0	1.14	-0.852
3	05 07 22.33	-68 47 58.2	1.21	2	0.43 ± 0.14	-0.05 ± 0.12	1.01×10^{-13}	05 07 22.15	-68 47 59.2	1.43	-0.515
4	05 07 55.35	-68 25 05.1	0.27	4	0.38 ± 0.02	-0.08 ± 0.02	1.59×10^{-12}	05 07 55.47	-68 25 05.3	0.66	-1.049
6	05 13 28.28	-65 47 18.4	0.37	–	–	–	–	05 13 28.26	-65 47 18.7	0.35	-0.923
7	05 20 49.11	-69 19 30.1	0.71	3	0.07 ± 1.98	0.94 ± 0.11	1.50×10^{-13}	05 20 48.84	-69 19 30.3	1.40	-0.576
8	05 24 17.14	-69 25 33.7	0.24	30	0.40 ± 0.13	-0.24 ± 0.11	8.05×10^{-14}	05 24 17.15	-69 25 33.8	0.08	-0.631
9	05 25 46.46	-69 44 50.9	0.33	22	0.48 ± 0.12	-0.20 ± 0.08	2.35×10^{-14}	05 25 46.32	-69 44 51.7	1.11	-0.401
10	05 28 58.38	-67 09 46.4	0.75	1	0.16 ± 0.18	-0.12 ± 0.17	1.18×10^{-13}	05 28 58.46	-67 09 45.9	0.69	-0.871
11	05 30 10.89	-69 47 55.8	0.91	1	0.07 ± 0.42	0.23 ± 0.30	2.66×10^{-14}	05 30 10.79	-69 47 55.4	0.71	-0.623
12	05 30 11.32	-65 51 23.9	0.37	2	0.34 ± 0.03	0.03 ± 0.02	1.21×10^{-12}	05 30 11.37	-65 51 24.1	0.34	-0.973
13	05 30 45.42	-70 40 35.7	1.10	2	0.52 ± 0.30	-0.06 ± 0.19	2.35×10^{-14}	05 30 45.16	-70 40 34.8	1.55	-0.573
14	05 30 59.27	-68 32 53.4	1.68	1	0.16 ± 0.44	0.15 ± 0.33	1.08×10^{-14}	05 30 59.41	-68 32 53.8	0.83	-0.962
15	05 31 08.33	-69 09 23.5	0.51	1	0.89 ± 0.02	0.46 ± 0.02	2.16×10^{-12}	05 31 08.45	-69 09 23.5	0.64	-0.524
16	05 33 20.87	-68 41 22.6	0.65	2	0.65 ± 0.04	0.03 ± 0.04	6.47×10^{-13}	05 33 20.69	-68 41 23.5	1.28	-0.945
17	05 33 28.23	-67 48 45.9	0.82	1	0.69 ± 0.23	-0.11 ± 0.17	1.59×10^{-13}	05 33 28.19	-67 48 46.5	0.68	-0.765
18	05 25 50.70	-69 27 29.9	0.30	24	0.90 ± 0.15	-0.10 ± 0.09	6.12×10^{-14}	05 25 50.59	-69 27 32.9	3.02	-0.804
19	05 40 45.48	-69 14 52.7	1.19	2	0.49 ± 0.60	0.38 ± 0.30	2.07×10^{-14}	05 40 45.58	-69 14 51.7	1.19	-0.772
20	05 41 34.18	-68 25 48.5	0.12	25	0.44 ± 0.03	-0.03 ± 0.03	2.81×10^{-11}	05 41 34.32	-68 25 48.4	0.77	-0.955

---

[a] BeCand-5: preliminary X-ray detection not confirmed. BeCand-6: no XMM-Newton data, Swift discovery (Krimm et al. 2009). BeCand-8/11: coordinates of optical counterpart from 2MASS 6X. BeCand-9: No 2MASS catalog entry, coordinates of optical counterpart from OGLE (with Imag). BeCand-2: The value for B (16.676 ± 0.091 mag) is obviously wrong in the MCPS catalogue, therefore we used B = 13.78 mag from Massey (2002) to compute the Q value. BeCand-18: likely a chance coincidence between optical and X-ray source.

[b] Average (error weighted) 0.2−12 keV flux in erg s^{-1} cm^{-2}

Table 2.2: Technical summary of various optical observing campaigns.

BeCand	SALT^a		1.9 m^b		OGLE IV ID
	Date	Exp. Time (s)	Date	Exp. Time (s)^c	
1	13-01-2014	200	24-11-2016	3600	LMC530.26.30737
2	13-01-2014	200	24-11-2016	3600	LMC508.31.62
3	15-01-2014	400	26-11-2016	5400	LMC510.11.55526
4	14-01-2014	200	-	-	LMC510.20.50751
6	14-01-2014	250	26-11-2016	3600	LMC506.16.16
7	14-01-2014	250	-	-	LMC503.11.56624
8	07-02-2014	400	-	-	LMC503.09.85386
9	16-01-2014	500	-	-	LMC516.25.32805
10	14-01-2014	250	26-11-2016	3600	LMC518.23.4542D
11	07-02-2014	500	29-11-2016	5400	-
12	15-01-2014	200	24-11-2016	3600	LMC519.29.9750
13	08-02-2014	300	27-11-2016	5400	LMC515.31.15984
14	30-10-2017	1300	-	-	LMC517.22.4360
15	19-01-2014	150	27-11-2016	1800	LMC517.05.18792
16	18-01-2014	160	-	-	LMC517.20.21029
17	15-01-2014	200	25-11-2016	5400	LMC518.03.9420
18	15-01-2014	250	27-11-2016	3600	LMC503.08.66672
19	16-01-2014	400	29-11-2016	3600	LMC553.24.87
20	16-01-2014	150	27-11-2016	1800	LMC554.06.18693

The ″-″ signifies the absence of a particular dataset. [a]SALT: The SALT dataset comprises of all the Hα spectra. [b]The 1.9 m dataset comprises of all the blue spectra for spectral classification, [c]while the listed exposure times are those of the averaged combined spectra.

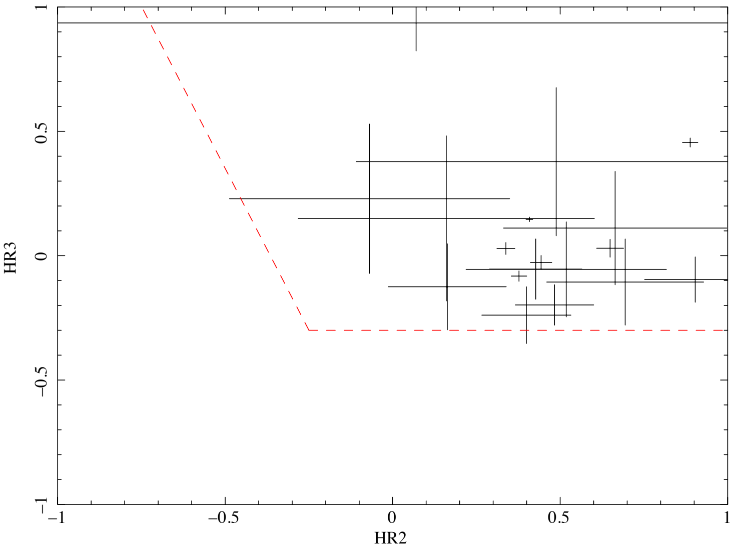

Figure 2.1: Hardness ratio diagram for the selected HMXB candidates. The dashed lines define the selection criteria in the HR3 vs. HR2 parameter space applied by Sturm et al. (2013) for Be/X-ray binaries in the Small Magellanic Cloud.

spectra with SNR of ~40. Table 2.2 shows the observation dates and the total exposure times for the average combined spectra. The spectra were reduced and extracted using IRAF*, cosmic ray cleaned using a Python based `lacosmic` routine (van Dokkum 2001), and wavelength calibrated using Copper-Argon arc lamps. The final, averaged combined spectra were rectified and smoothed with a 3 point boxcar smoothing routine, using IRAF's `splot` routine.

2.2.4 OGLE IV light curves

The Optical Gravitational Lensing Experiment (Udalski et al. 2015) provided long term I band light curves with roughly daily sampling for 18 of the candidates in the OGLE IV field. BeCand-11 was the only candidate for which no photometry was available, but the respective OGLE ID's for which photometry was available are listed in Table 2.2. The OGLE light curves were used to study the variability of the candidate optical counterparts. The identified periodicities and comments on the variability are listed in Table 2.3.

---

*http://iraf.noao.edu

2.3 Analysis Methods

2.3.1 SALT Hα spectra

Two categories of Hα emission were observed namely, narrow emission characteristic of diffuse, interstellar HII regions in the LMC, which is not intrinsic to the candidates, and broad emission resulting from Doppler shifts due to the motion of the decretion disc. BeCand-8 only showed narrow Hα emission, while BeCand-18 had extended narrow Hα emission superimposed on broad Hα emission (Figure 2.2). Out of the 19 optical candidates 13 candidates exhibited intrinsic Hα emission. IRAF's `splot` was used to measure the equivalent widths (EWs), as well as the V/R ratios for the double peaked profiles. The Hα profile measurements for each candidate was repeated 5 times to determine a average EW and V/R ratio, with the uncertainty estimated from the standard deviation of the mean. Figure 2.2 shows the emission Hα spectra and Table 2.3 lists the various Hα profile measurements for the 15 HMXB candidates that exhibit Hα emission.

2.3.2 SAAO 1.9 m blue spectra

The LMC has a lower metallicity than that of the Milky Way (MW), but higher than that of the SMC, hence the spectral behaviour will not necessarily be the same as either the SMC or MW. However Negueruela & Coe (2002) and McBride et al. (2008) have shown independently that the spectral type distributions of the LMC and SMC BeXBs are consistent with that of the Milky Way BeXBs. To determine the spectral class of the candidates we considered spectral classification of massive O and B stars in the SMC, LMC and the MW. We compared the spectra by eye, using the digital MW spectral atlas provided by Walborn & Fitzpatrick (1990), the criteria identified by Evans et al. (2004) for the SMC, as well as the spectral atlas of the 30 Doradus region in the LMC by Walborn et al. (2014), and the criteria provided by Evans et al. (2015) for the north-eastern region of the LMC. We found that the results were relatively consistent with one another. The distance modulus resulting from the spectral and luminosity classifications was compared to the distance modulus of the LMC (~18.48; Walker 2012) using the absolute magnitudes from Zombeck (1990), and direction dependent extinction values from Haschke et al. (2011). Table 2.3 lists the identified spectral classes, while Figures 2.3 and 2.4 shows the spectra grouped by spectral class.

2.3.3 Timing Analysis

The timing analysis described here is based on the method applied to SMC BeXBs by Bird et al. (2012). The OGLE IV light curves were detrended with a 51 and 101 day running average routine, acting as a high pass filter to increase the sensitivity of the Lomb-Scargle periodogram

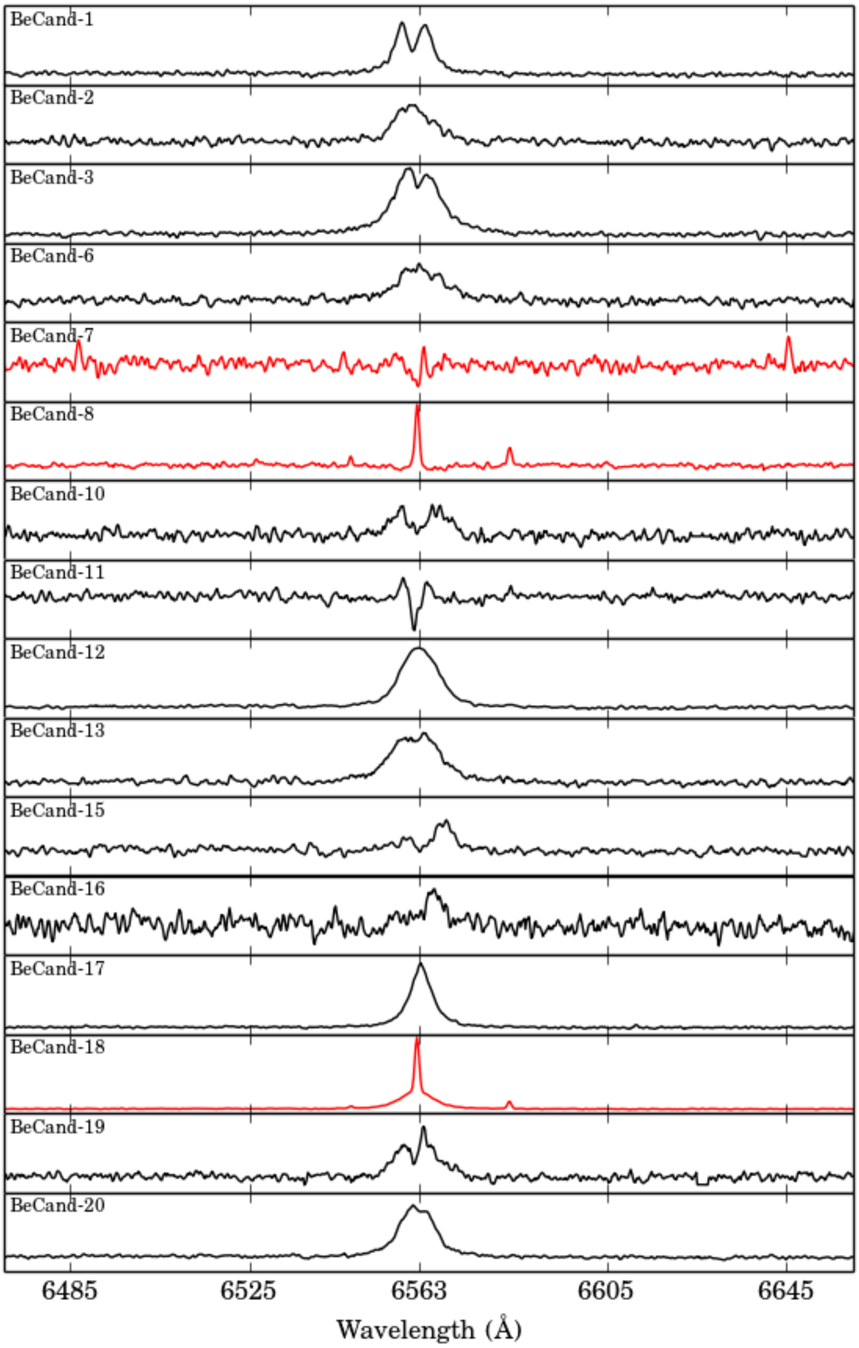

Figure 2.2: Emission Hα profiles. The y-scale for each profile was chosen independently to highlight the various Hα profiles. The spectra highlighted in red are sources containing narrow Hα emission, not necessarily intrinsic to the sources. BeCand-7 shows Hα infilling, however it is not clear if the emission is intrinsic to the source or not. The Hα emission of BeCand-8 is not associated with the optical candidate, but rather with HII region surrounding the optical candidate. BeCand-18 also highlighted in red shows broad emission from the Be star superimposed on extended narrow emission from a small HII region. The remaining candidates (black curves) show intrinsic Hα emission.

Table 2.3: Summary of the results from the optical spectroscopy and OGLE timing study.

BeCand	RA (J2000)	Dec (J2000)	V mag MCPS	EW(Hα) (Å)	V/R	Sp Type	Period (days)	BeXB?
1	04 55 46.34	-69 57 18.8	14.47	-22.3 ± 0.5	0.997	B1 IIIe	76 ± 2	yes
2[a]	05 00 46.05	-70 44 36.0	14.73	-11 ± 1	-	O9 Ve	30.7 ± 0.5, 442 ± 58	yes
3	05 07 22.15	-68 47 59.2	15.79	-94 ± 1	1.230	B3 IIIe	5.27 ± 0.02	yes
4[b]	05 07 55.35	-68 25 05.1	14.96	-	-	OB	262 ± 46	yes
6[c]	05 13 28.28	-65 47 18.4	15.10	-11.0 ± 0.3	-	B0-B1 Ve	27.4 ± 0.4	yes
7	05 20 49.11	-69 19 30.1	15.178	0.7 ± 0.2	-	-	440 ± 43	?
8[d]	05 24 17.14	-69 25 33.7	15.962	-7 ± 1	-	-	32.7 ± 0.4, 547 ± 190	?
9	05 25 46.46	-69 44 50.9	16.39	-	-	-	Variability	?
10	05 28 58.38	-67 09 46.4	15.04	-8.5 ± 0.4	0.952	B0-B0.5 Ve	193 ± 48	yes
11	05 30 10.89	-69 47 55.8	16.07	-1.2 ± 0.2	1.086	B2-B3 IIIe	-	yes
12	05 30 11.32	-65 51 23.9	14.88	-31.2 ± 0.5	-	B1-B3 IIIe-Ve	74 ± 2	yes
13	05 30 45.42	-70 40 35.7	15.58	-22.4 ± 0.4	-	B0.5-B1 Ve	280 ± 44	yes
14[e]	05 30 59.27	-68 32 53.4	15.91	-	-	-	None	no
15[f]	05 31 08.33	-69 09 23.5	13.70	-3.5 ± 0.2	0.365	B0 IIIe	Variability	yes
16[g]	05 33 20.87	-68 41 22.6	12.68	-	-	B0.5 Ib	Variability	yes
17	05 33 28.23	-67 48 45.9	14.82	-29.4 ± 0.2	-	Earlier B0.5 IIIe	560 ± 87	yes
18[h]	05 25 50.70	-69 27 29.9	15.12	-33.5 ± 0.9	-	B2 IVe-Ve	None	no
19	05 40 45.48	-69 14 52.70	15.98	-21.6 ± 0.3	0.740	B1-B3 IIIe-Ve	Variability	yes
20	05 41 34.18	-68 25 48.5	14.04	-15.5 ± 0.3	-	B0-B1 IIIe	31.5 ± 0.4	yes

The coordinates for the optical counterparts are from Table 2.1 listed in the 2MASS column. A ″−″ indicate a measurement that could not be made, either due to the absence or the quality of the data. In the case of the *V/R* column, V/R measurements could only be taken for double peaked Hα emission lines. [a] BeCand-2: Classified as BeXB (Vasilopoulos et al. 2016). [b] BeCand-4: OB spectral class determined from photometry, and classified as BeXB (Maggi et al. 2013). [c] BeCand-6: Classified as BeXB (Coe et al. 2015). [d] BeCand-8: The Hα emission does not originate from a decretion disc around the central star, but is from a surrounding nebula. [e] BeCand-14: The Hα spectrum was taken in a follow-up campaign with SALT on 30 October 2017. [f] BeCand-15: Vasilopoulos et al. (2018) classified the optical companion as a B0 II-Ibe star. [g] BeCand-16: Spectral class determined by Vasilopoulos et al. (2018). Possible infilling of the Hα line, however the spectrum does not have sufficient SNR to measure a accurate EW. [h] BeCand-18: The quoted EW includes only the broad component of the Hα emission profile.

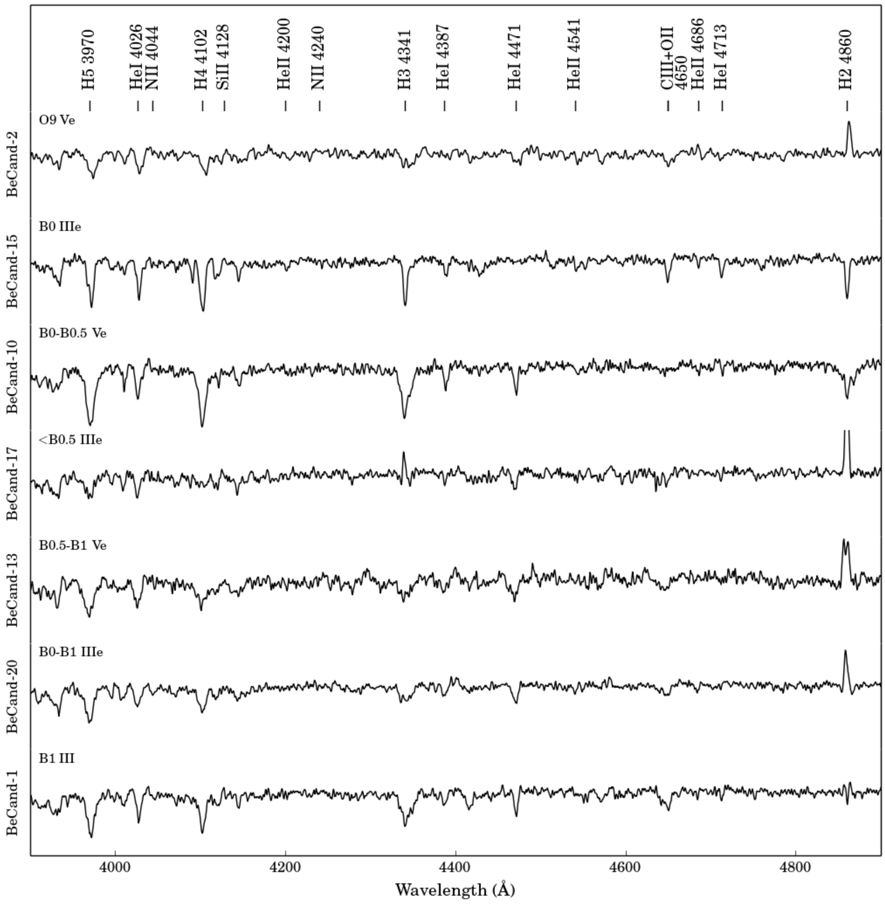

Figure 2.3: Blue-end spectra of candidates with spectral class B1 and earlier. The open ended emission lines are Balmer emission originating from the decretion disc that were cut off for a better y-scale.

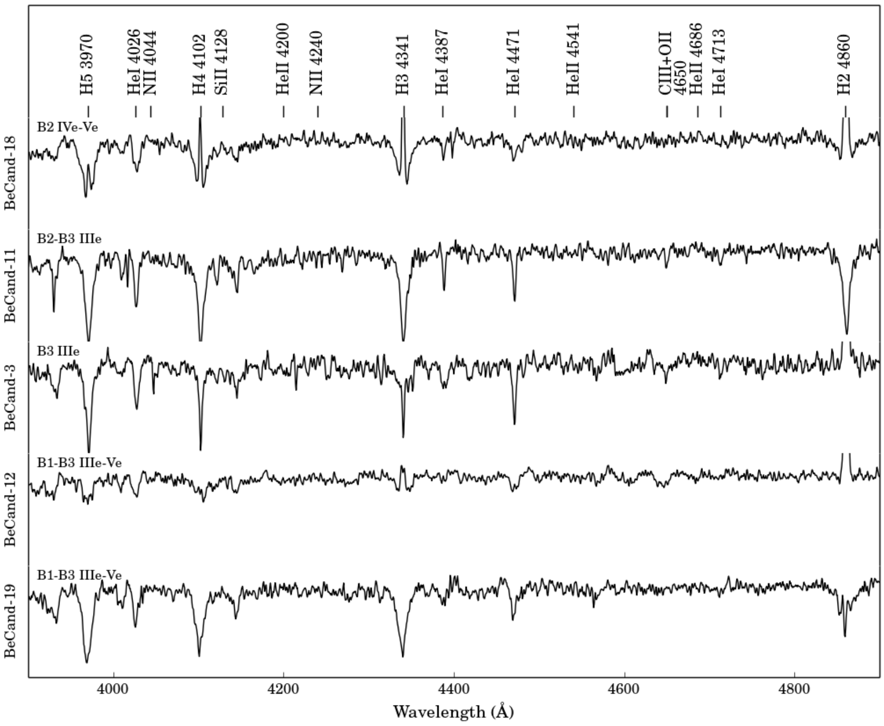

Figure 2.4: Blue spectra of candidates with spectral class later than B2. The open ended emission lines are Balmer emission originating from the decretion disc that were cut off for a better y-scale.

at shorter periods. The Lomb-Scargle periodograms of both the raw and detrended light curves were calculated by *gatspy* (Vanderplas 2015), a `Python` based Lomb-Scargle program. Furthermore, the 3σ significance levels of the power spectra were determined by running a Monte Carlo simulation with 10 000 iterations, using the raw and detrended light curves as inputs. The simulations were setup such that the time structure was preserved, but the intensities were randomised. Finally, significant aliases, harmonics and beat frequencies were calculated based on the sampling frequency and the annual sampling period to determine which significant peaks in the power spectra were due to variability intrinsic to the source. The timing analysis results are summarised in Table 2.3.

Bird et al. (2012) showed that non-radial pulsations (NRPs) of less than a day can beat with the daily sampling period, resulting in significant longer periods (> 10 days) in the power spectra. It is possible to distinguish between aliased NRPs and orbital modulations by considering two metrics from the shape of the phase folded light curves. Since perturbations associated with orbital modulation are caused by the neutron star's interaction with the decretion disc, they result in a fast rise and exponential decay (FRED) phase folded light curve. Aliased NRPs, on the other hand, are associated with a more sinusoidal phase folded light curve. The metrics are the phase FWHM, i.e. the phase span (PS), and the phase asymmetry (PA). The PA was given by the fraction of the phase length calculated from the difference between the peak and 10% of the peak value on the left and right hand side of the phase folded light curve (See Table 2.4). Bird et al. (2012) found that orbital modulation and the aliased NRPs occupy distinct regions in the PA-PS plane (Figure 2.6). From this we conclude that BeCand-2,6,7,8 and 20 exhibit orbital modulation, while the remaining periodicities appear to be associated with aliased NRPs, except BeCand-1's light curve which showed a clear 76 ± 2 d modulation with a sinusoidal phase folded light curve.

2.4 Discussion

From the *XMM-Newton* survey 19 X-ray sources were identified as potential HMXBs based on their hardness ratios and the association with an early type star. In Table 2.3 we present the spectral properties and timing results of 18 of the optical counterparts that are coincident with the X-ray sources, as well as BeCand-18, which was identified as a likely chance coincidence.

2.4.1 New BeXBs

We classify 9 of the optical candidates as Be stars with spectral types B3 and earlier, with variable and periodic OGLE light curves. We confirm these 9 sources as new BeXBs, increasing the

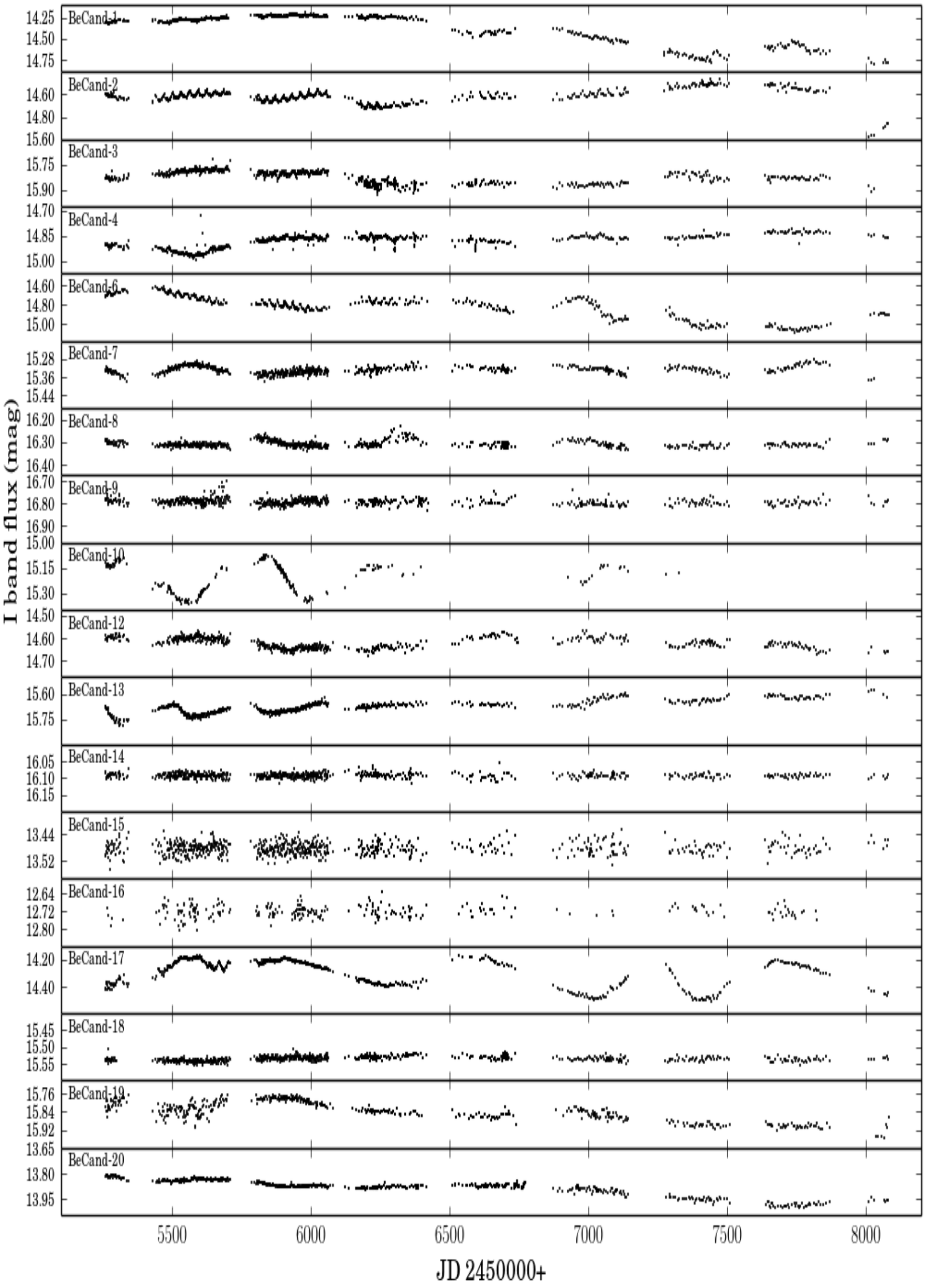

Figure 2.5: OGLE I band light curves.

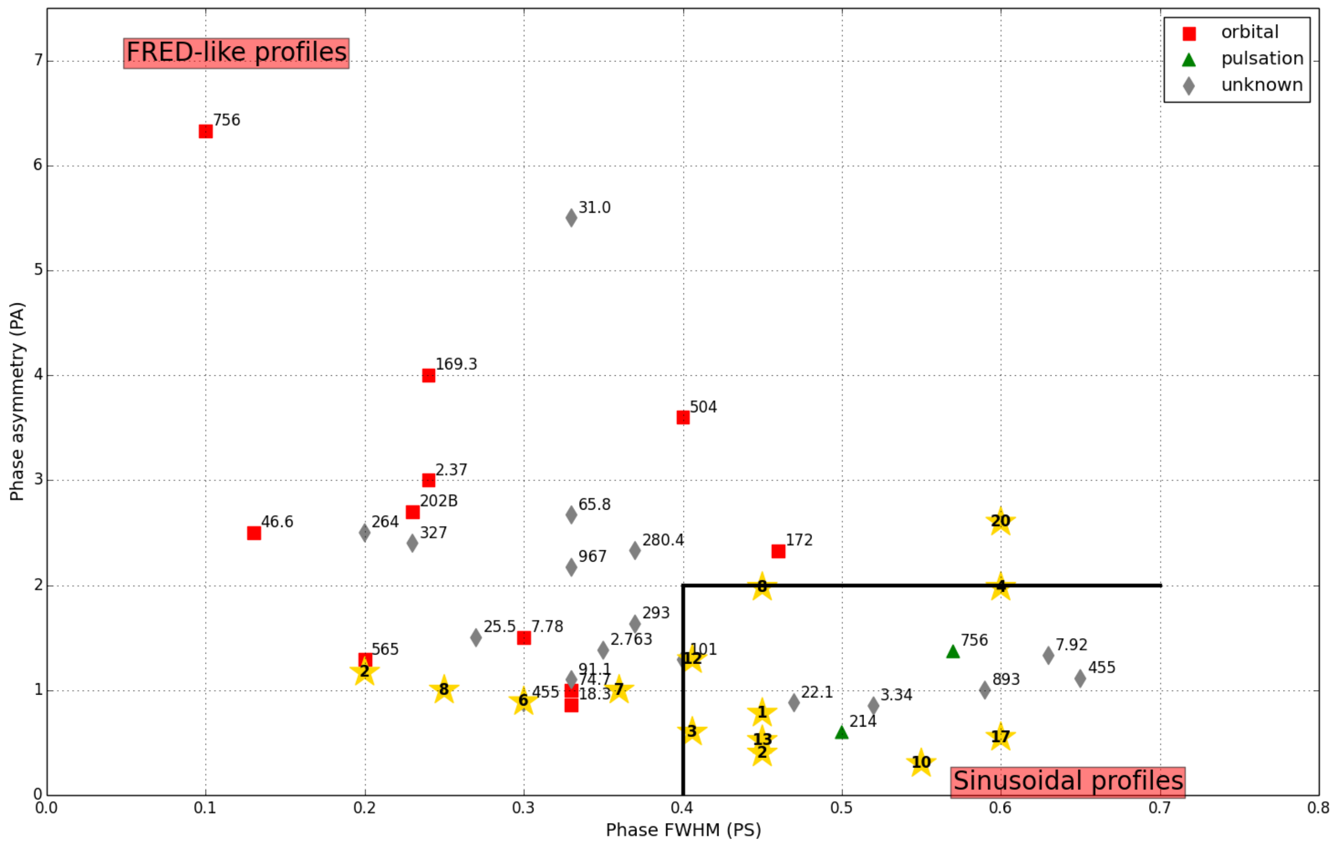

Figure 2.6: Phase metrics to distinguish between orbital pulsations with FRED phased folded light curves, and aliased non-radial pulsations with sinusoidal phased folded light curves. The number next to each point is the X-ray pulse period in seconds, while our candidates are indicated by the yellow stars with the star number corresponding to the candidate number. BeCand-2 and 13 in the Sinusoidal region of the plot were shifted slightly in PA in order to resolve the two candidates. Furthermore, BeCand-3,4,8 and 12 are located on the periphery of the FRED and Sinusoidal division. They were shifted slightly for clarity. The "unknown" sources refer to the sources where it is not clear if the observed period is related to orbital pulsations or aliased non-radial pulsations. The original plot was taken from Bird et al. (2012).

Table 2.4: The phase span (PS) and phase asymmetry (PA) measurements of the phased folded OGLE IV light curves. The results are plotted in Figure 2.6.

BeCand	Period	PS (FWHM)	PA	Type
1	76 ± 2	0.45	0.78	Sinusoidal
2	30.7 ± 0.5	0.20	1.17	FRED
-	442 ± 58	0.45	0.40	Sinusoidal
3	5.27 ± 0.02	0.40	0.60	?
4	262 ± 46	0.60	2.00	?
6	27.4 ± 0.4	0.30	0.89	FRED
7	440 ± 43	0.35	1.00	FRED
8	32.7 ± 0.4	0.45	2.00	?
-	547 ± 190	0.25	1.00	FRED
10	193 ± 48	0.55	0.30	Sinusoidal
12	74 ± 2	0.40	1.29	?
13	280 ± 44	0.45	0.45	Sinusoidal
17	560 ± 87	0.60	0.55	Sinusoidal
20	31.5 ± 0.4	0.60	2.60	FRED

The ″?″ indicates the periods for which the phase folded light curve metrics were located on the periphery of the FRED and Sinusoidal regions of Figure 2.6.

LMC's BeXB population to 26, moreover increasing the HMXB population of the LMC by ~50%.

2.4.2 Known XMM BeXBs

BeCand-2 was detected previously with INTEGRAL (IGR J05007−7047, LXP 38.55) and confirmed as a BeXB with a 38.55 s X-ray pulsar, and a orbital period of 30.776 ± 0.005 d (Vasilopoulos et al. 2016), with a B2 IIIe companion (Masetti et al. 2006). Our OGLE analysis yielded a consistent orbital period of 30.8 ± 0.5 d, although the blue optical spectrum had a HeII absorption line at λ4200 Å, which is consistent with a O9e V star.

Early on in the XXM survey BeCand-4 (LXP 169) was classified as a BeXB based on its X-ray pulse period of 168.8 s, as well as long term X-ray variations, and *I*-band OGLE III-IV light curves. Maggi et al. (2013) interpreted the rapid decrease in brightness, appearing at all epochs separated by period of 24.328 d, as a binary transit observed at a high inclination angle. Our Lomb-Scargle analysis revealed a significant period associated with a likely aliased NRP at 262 ± 46 d (See Figure 2.6).

Swift observed BeCand-6 (Swift J0513.4−6547, LXP 27.2) in April 2009, and was later classified by Coe et al. (2015) as a BeXB with a 27.2 s pulse period, and a *I*-band OGLE IV orbital period of 27.405 ± 0.008 d, with ~B1 Ve companion. We determined a orbital period of 27.4 ± 0.4 d from I-band OGLE IV light curve, which is consistent with the previous study. In addition we classified the companion star as a B0e-B1 Ve star, also consistent with the previous analysis.

Vasilopoulos et al. (2018) confirmed BeCand-15 (XMMU J053108.3−690923) as a HMXB belonging to the SGXB group, with a B0 II-Ibe optical companion and an X-ray spin period of 2013 s. However, in this work we have classified the companion of BeCand-15 as a B0 IIIe star. This discrepancy is likely due to the lower S/N ratio of the blue spectrum which we used for our classification. BeCand-16 (XMMU J053320.8−684122) was also classified as a SGXB with a B0.5 Ibe companion by Vasilopoulos et al. (2018), with fast flaring X-ray behaviour.

2.4.3 Published XMM pulsars

X-ray pulsations with a period of 272 s (Haberl et al. 2003) was detected for BeCand-12 (XMMU J053011.2−655122). From our study we confirm BeCand-12 as a BeXB with a significant period around 74 ± 2 d, with a B1-B3 III-Ve companion.

Shtykovskiy & Gilfanov (2005) identified BeCand-20 (XMMU J054134.7−682550) as a likely HMXB based on its X-ray properties. Subsequently Manousakis et al. (2009) observed BeCand-20 in a flaring state and found a 61.601 ± 0.017 s X-ray pulsation with RXTE. We confirm BeCand-20 as a BeXB with a 31.5 ± 0.4 d orbital period, and a B0-B1 IIIe optical companion.

2.4.4 Unconfirmed candidates

The nature of 3 of the candidates (BeCand-7, 8, 9) remains unresolved, and require additional optical spectroscopic follow up. BeCand-7 showed definite infilling of the Hα line with a EW of 0.7 ± 0.2, and exhibited an orbital period of 440 ± 43 d, however we did not obtain blue-end spectra due to unfavourable weather conditions. As a result BeCand-7 is likely a Be star based on the data in hand, but the definite spectral type is unknown. From Figure 2.2 we observe a narrow Hα line for BeCand-8, consistent with diffuse interstellar emission, not necessarily intrinsic to the source, and with a orbital period of 547 ± 190 d. The Hα spectrum of BeCand-9 was too faint to extract reliably, however the OGLE IV light curve showed some variability. A second epoch of Hα observations will be necessary to determine if these candidates are emission line stars. In addition to the Hα spectra, blue-end spectra are still required to make a reliable spectral classification. Due to insufficient optical spectroscopy the nature of the optical counterparts remain uncertain for BeCand-7, 8 and 9, however these optical counterparts are coincident with X-ray emission, and in the case for BeCand-7, 8 and 9 were detected multiple times in the XMM data.

2.4.5 Non-HMXB systems

With no Hα emission and no variability observed in the OGLE IV light curve, BeCand-14 is likely not at BeXB, while BeCand-18 is peculiar amongst our sample as the Hα profile has both broad and narrow components. The narrow component originates from a resolved nebula around 10″ in diameter. The emission line ratios of log(Hα/[N II])=0.9 and log(Hα/[S II])=0.6 are consistent with extragalactic HII regions (Frew & Parker 2010). Imaging at mid-infrared wavelengths with *Spitzer* is also consistent with the nebula being an HII region (Meixner et al. 2006). The broad Hα component from the B2e IV-V central star suggests a Be star is the ionising source of the HII region. An O-type emission line classification (e.g. Walborn et al. 2014) cannot be associated with the broad Hα emission given the B2e IV-V classification.

2.5 Conclusions

Eighteen of the XMM X-ray sources were coincident with optical counterparts, of which 3 (BeCand-2, 4 ,6) have been classified as BeXBs, and 2 (BeCand-15, 16) as SGXB in previous work, while the nature of 3 candidates (BeCand-7,8,9) are still uncertain. The 9 remaining candidates we classify as new BeXBs (see Table 2.3), raising the population of BeXBs in the LMC to 26, and subsequently the number of confirmed HMXBs in the LMC to 32. Moreover, as expected all the BeXBs have spectral classes of B3 and earlier, as well as variable OGLE light curves.

Acknowledgements

The XMM-Newton project is supported by the Bundesministerium für Wirtschaft und Technologie/Deutsches Zentrum für Luft- und Raumfahrt (BMWI/DLR, FKZ 50 OX 0001) and the Max-Planck Society. GV acknowledges support from the BMWI/DLR grant FKZ 50 OR 1208. DAHB and VM acknowledges support of the National Research Foundation of South Africa (grants IFR2010042800093,98969 and 93405). This paper uses observations made at the South African Astronomical Observatory (SAAO) and with the Southern African Large Telescope. The OGLE project has received funding from the National Science Centre, Poland, grant MAESTRO 2014/14/A/ST9/00121 to AU.

Chapter 3

Targeted search for young radio pulsars in the SMC: Discovery of two new pulsars

Abstract

We report the first rotation powered pulsars discovered in the Small Magellanic Cloud (SMC) in more than a decade. PSR J0043−73 and PSR J0052−72 were discovered during a Parkes Multi-Beam (PMB) survey of MCSNR J0127−7332, and five new, optically selected, supernova remnant (SNR) candidates identified by the XMM Newton survey. In addition to the candidates, we adjusted the PMB rotation to include an additional nine SNRs and pulsar wind nebulae. We searched for young pulsars (1 – 200 ms) employing a Fourier analysis with `PRESTO`, as well as a search for longer period pulsars (200 ms – 360 s) with a fast folding algorithm. Our targeted survey had a limiting flux density of 0.039 mJy for periods greater than 50 ms. Although not the main target of this search it was also sensitive to millisecond pulsars. PSR J0043−73 has a period and dispersion measure of 937.42937 (26) ms and 115.1 (3.4) pc cm^{-3} respectively, and PSR J0052−72 has a period of 191.444328 (46) ms and a DM of 158.6 (1.6) pc cm^{-3}.

3.1 Introduction

The Magellanic Clouds (MCs) are our closest satellite galaxies, and the only galaxies other than the Milky Way in which we have been able to detect radio pulsars. The MCs have gone through a relatively recent episode of star formation (Antoniou et al. 2010, Antoniou & Zezas 2016), producing a large number of O and B stars, many of which are companions in high mass X-ray binary (HMXB) systems. A recent census (Antoniou et al. 2019) identified 137 HMXBs (of which 63 are X-ray pulsars) in the Small Magellanic Cloud (SMC) – similar to the population in the Milky Way, despite the fact that the SMC is only one-fiftieth the mass. This is a clear indication that the SMC harbours many neutron stars (NSs) and many in interesting binaries. However, despite this large population of NSs only five rotation powered pulsars so far have been discovered in the SMC through various MC radio surveys (McConnell et al. 1991, Crawford et al. 2001, Manchester et al. 2006).

Massive stars form NSs during core-collapse supernova events. Most of the newly formed NSs are rotation-powered pulsars (Keane & Kramer 2008), which emit pulsed, non-thermal radio emission. Energetic young radio pulsars can produce an outflow of relativistic particles which will interact with their natal SNR and the surrounding interstellar medium, creating a pulsar wind nebula (PWN). Thus, SNRS and PWNe are excellent candidates for targeted radio pulsar surveys, that being said pulsars have so far only been discovered in ~50% of SNRs and PWNe (Green 2014). The lack of SNRs and PWNe associations with pulsars may be the result of beaming effects, or alternatively due to instrumentation sensitivity limits. Camilo (2003) completed a census of SNR-pulsar associations (Kaspi & Helfand 2002, Gorham et al. 1996, Lorimer et al. 1998, Manchester et al. 2001) and found that in some cases the pulsars associated with SNRs can be faint. Hence, deep surveys may be required to detect these young radio pulsars.

The first of the SMC surveys using the Parkes radio telescope was conducted by McConnell et al. (1991) with a limiting mean flux density at 610 MHz of 0.5 - 0.8 mJy for pulsars with periods greater than 500 ms and dispersion measure (DMs) of 100 pc cm^{-3} or less. The survey discovered 1 pulsar, PSR J0045−7319, later shown to be in a 51 day orbit around a 16th magnitude B star (Kaspi et al. 1994). In a subsequent SMC survey with the 20 cm Multi-Beam receiver at Parkes (PMB), Crawford et al. (2001) discovered PSR J0113−7220. The survey covered a more complete region of the SMC (~6.7 deg^2) with a limiting flux density of 0.08 mJy at 1400 MHz for pulsars with periods greater than 50 ms and DMs less than 200 pc cm^{-3}. The most recent and successful SMC survey was conducted by Manchester et al. (2006), also using the PMB receiver, in which three pulsars were detected (PSR J0045−7042, PSR J0111−7131, PSR J0131−7310). The advantage of the Manchester et al. (2006) survey was the increased DM range of up to 277 pc cm^{-3}, however it was most sensitive to periods greater than 50 ms, but with a similar limiting flux density to the Crawford et al. (2001) survey.

Due to the distance to the SMC (~60 kpc), the blind surveys only detected the brightest pulsars, since integration time is sacrificed to cover a larger area. To improve upon the sensitivity of the previous blind surveys we carried out the deepest, most sensitive pulsar searches of five supernova remnant (SNR) candidates, as well as MCSNR J0127−7332 in the SMC. Finding a young pulsar which is coincident with its natal SNR or within a PWN will enable studies of the initial spin period, velocity, and magnetic field distributions of young NSs, providing insights to the physics governing core-collapse. It also enable searches at other energies, particularly X-ray observations can facilitate NS cooling studies. Finding just one new radio pulsar in the SMC will provide valuable details about the nature of the SMC pulsar population and the progenitor stars that formed it. Particularly, the low metallicity environment of the SMC will affect mass loss of massive stars uniquely when compared to the Galaxy. This may be reflected in the distribution of angular momentum of the radio pulsars.

In this paper we present the results for our targeted pulsar searches in the SMC. In Section 3.2, we describe the observations, followed by the data reduction process in Section 3.3. In Section 3.4 we present the results, and discuss their implications in Section 3.5. Finally, in Section 3.6, we draw our conclusions.

3.2 Source Selection and Observations

3.2.1 Supernova Remnant Candidates

The XMM-Newton satellite has conducted the deepest complete survey of the SMC in the 0.15–12.0 keV X-ray band to date (Haberl et al. 2012, Sturm et al. 2013). The relatively close and known distance to the SMC (60 kpc) together with the moderate Galactic foreground absorption of NH $\approx 6\times10^{20}$ cm^{-2} (Dickey & Lockman 1990) provides an opportunity to study the complete X-ray source population within the SMC. These are dominated by HXMBs, SNRs and super-soft X-ray sources. In total the survey detected 23 SNRs, 20 previously known (Badenes et al. 2010) and 3 new candidates, XMMU J0049-7306, XMMU J0056.6-7208 and XMMU J0057.7-7213.

Following a study of narrow band optical images (Hα and SII) and ATCA radio observations (Filipović et al. 2005, Payne et al. 2007, Roper et al. 2015, Maggi et al. 2019) of the SMC, nine new SNR candidates were selected for further study. One of these (SNR C1) was found to be coincident with one of the newly identified XMM-Newton SNRs (Haberl et al. 2012), namely XMMU J0056.6-7208. Following SALT long slit spectroscopy of 8 of these new candidate SNRs, SII/Hα ratios were determined and indicated that 6 were consistent with being SNR. These, plus the two other XMM-Newton SNR candidates were then selected to be observed by SALT using the Fabry-Perot imaging at Hα, SII and OIII. In the end only 7 SNRs candidates were observed, of which 4 showed strong evidence for SNR shells, namely SNR C1 (=XMMU J0056.6-7208), SNR C3, SNR C4 & SNR C9). The 3 others showed either indistinct or small shells (SNR C2, SNR C6 & XMMU J0057.7-7213). A known SNR, MCSNR J0127−7332, which is associated with a slowly spinning X-ray pulsar SXP 1062 in

Table 3.1: The PMB receiver properties as recorded by Manchester et al. (2001).

Beam	Centre	Inner	Outer
Gain (K Jy^{-1})	0.735	0.690	0.581
Half power beamwidth (arcmin)	14.0	14.1	14.5
Beam ellipticity	0.0	0.03	0.06
Coma lobe (dB)	none	17	14

a Be X-ray binary (Hénault-Brunet et al. 2012), was observed as a control object, which was confirmed as a SNR.

We were awarded 54 hours with the Parkes radio telescope to observe six of the SNR candidates (MCSNR J0127−7332, XMMU J0049.0−7306, SNR C3, SNR C2, XMMU J0056.6−7208, SNR C9), which were coincident with X-ray point sources.

3.2.2 Parkes Observations

The PMB receiver (Staveley-Smith et al. 1996a) has the ability to observe 13 distinct regions on the sky simultaneously, covering a 0.5 deg^2 region, making it ideal for surveys. The PMB consists of the most sensitive central beam, six inner ring beams, and the six least sensitive outer ring beams. The beam properties are listed in Table 3.1.

We used the PMB with the Berkeley-Parkes-Swinburne data recorder (BPSR, McMahon 2008; Keith et al. 2010) to perform deep pulsar searches in the SMC. The focus of the survey was 5 optically selected SNR candidates, as well as a known SNR, MCSNR J0127−7332, which are coincident with X-ray point sources. The extent of the SNRs was less than the ~14 arcmin half power beam width (HPBW) of the PMB. The central beam of the PMB was positioned on the SNRs, and then rotated to include an additional 9 known SNRs and PWNe (Filipović et al. 2008). The targets are listed in Table 3.2. One beam of one pointing was adjusted as much as possible to the position of PSR J0131−7310, a known radio pulsar in the SMC, with a period and DM of 348.124045581 (7) ms and 205.2 pc cm^{-3} respectively (Manchester et al. 2006). The PMB beam pattern and configuration is highlighted in Figure 3.1.

Our observations were carried out between 25 August 2017 and 13 December 2017, using a central frequency of 1382 MHz with a bandwidth of 400 MHz, split into 1024 channels, and a temporal resolution of 64 μs. Each field was observed twice (except for the MCSNR J0127−7332 pointing which was observed 3 times), separated on average by 20 days, with an integration time of ~15 000 s per pointing. This would allow us to cross match candidates identified in a

Table 3.2: Survey field observed in the SMC with the PMB.

Date	Target	Beam	Epoch[a] (MJD)	RA$_{beam}$[b] (J2000)	Dec$_{beam}$[b] (J2000)	t_{int}[c] (s)	Type (SNR/PWN)	Confirmed (yes/no)	Figure 3.1: PMB pattern
2017–08–25	MCSNR J0127−7332	1	57990.50	01 27 37.66	-73 35 20.50	16 223	SNR	yes	Red
	XMMU J0049.0−7306	1	57990.69	00 49 54.48	-73 04 09.70	12 989	SNR	no	Green
	DEM S5	13	57990.69	00 41 24.24	-73 39 24.80	12 989	PWN	yes	Green
	B0050−72.8	3	57990.69	00 51 35.18	-72 36 02.30	12 989	SNR	yes	Green
2017–08–28	SNR C3	1	57993.47	01 03 27.99	-72 03 41.30	16 217	SNR	no	Blue
	IKT 16	2[d]	57993.47	00 58 06.93	-72 19 17.60	16 217	PWN	yes	Blue
	IKT 21	1	57993.47	01 03 27.99	-72 03 41.30	16 217	SNR	yes	Blue
	1E0102−723	1	57993.47	01 03 27.99	-72 03 41.30	16 217	SNR	yes	Blue
	SNR C2	1	57993.66	00 56 31.02	-72 15 48.40	14 000	SNR	no	Cyan
	B0058−71.8	9	57993.66	01 00 19.47	-71 28 15.00	14 000	SNR	yes	Cyan
	IKT 25	10	57993.66	01 07 23.94	-72 06 41.50	14 000	SNR	yes	Cyan
2017–08–29	XMMU J0056.6−7208	1	57994.55	00 56 37.69	-72 09 01.40	16 223	SNR	no	Magenta
	N S66D	1	57994.55	00 56 37.69	-72 09 01.40	16 223	SNR	no	Magenta
	HFPK 334	12	57994.55	01 04 25.17	-72 45 33.80	16 223	SNR	yes	Magenta
	SNR C9	1	57994.74	01 12 39.07	-73 28 15.40	15 487	SNR	no	Yellow
2017–09–11[e]	MCSNR J0127−7332	1	58007.44	01 27 37.66	-73 35 20.50	16 224	SNR	yes	Red
	XMMU J0049.0−7306	1	58007.63	00 49 54.48	-73 04 09.70	12 319	SNR	no	Green
	DEM S5	13	58007.63	00 41 24.39	-73 39 25.40	12 319	PWN	yes	Green
	B0050−72.8	3	58007.63	00 51 35.18	-72 36 02.30	12 319	SNR	yes	Green
2017–09–12	SNR C3	1	58008.54	01 03 27.99	-72 03 41.30	16 221	SNR	no	Blue
	IKT 16	7[d]	58008.54	00 58 06.93	-72 19 17.60	16 221	PWN	yes	Blue
	IKT 21	1	58008.54	01 03 27.99	-72 03 41.30	16 221	SNR	yes	Blue
	1E0102−723	1	58008.54	01 03 27.99	-72 03 41.30	16 221	SNR	yes	Blue
	SNR C2[f]	1	58008.73	00 56 31.02	-72 15 48.40	5 436	SNR	no	Cyan
	B0058−71.8	9	58008.73	01 00 19.47	-71 28 15.00	5 436	SNR	yes	Cyan
	IKT 25	10	58008.73	01 07 23.94	-72 06 41.50	5 436	SNR	yes	Cyan
2017–09–28	XMMU J0056.6−7208	1	58024.52	00 56 37.69	-72 09 01.40	16 218	SNR	no	Magenta
	N S66D	1	58024.52	00 56 37.69	-72 09 01.40	16 218	SNR	no	Magenta
	HFPK 334	12	58024.52	01 04 25.26	-72 45 33.30	16 218	SNR	yes	Magenta
	SNR C9	1	58024.71	01 12 39.07	-73 28 15.40	13 469	SNR	no	Yellow
2017–12–13	MCSNR J0127−7332[g]	1	58100.47	01 27 37.66	-73 35 20.50	17 852	SNR	yes	Red

[a] The observation Epoch refers to the start of an observation. [b] The PMB coordinates within which the SNR was located. [c] t_{int} is the observation integration time. [d] IKT 16: The PMB was rotated by 60°, resulting in a different beam number corresponding to the same beam coordinates. Thus on 2017–08–28 IKT 16 was located in beam 2, but in beam 7 on 2017–09–12. [e] During the observations on 2017–09–11 strong RFI was detected. [f] SNR C2: The observation was terminated due to strong winds. [g] MCSNR J0127−7332: Additional Director's Time was allocated due to severe RFI during the 2017–09–11 pointing.

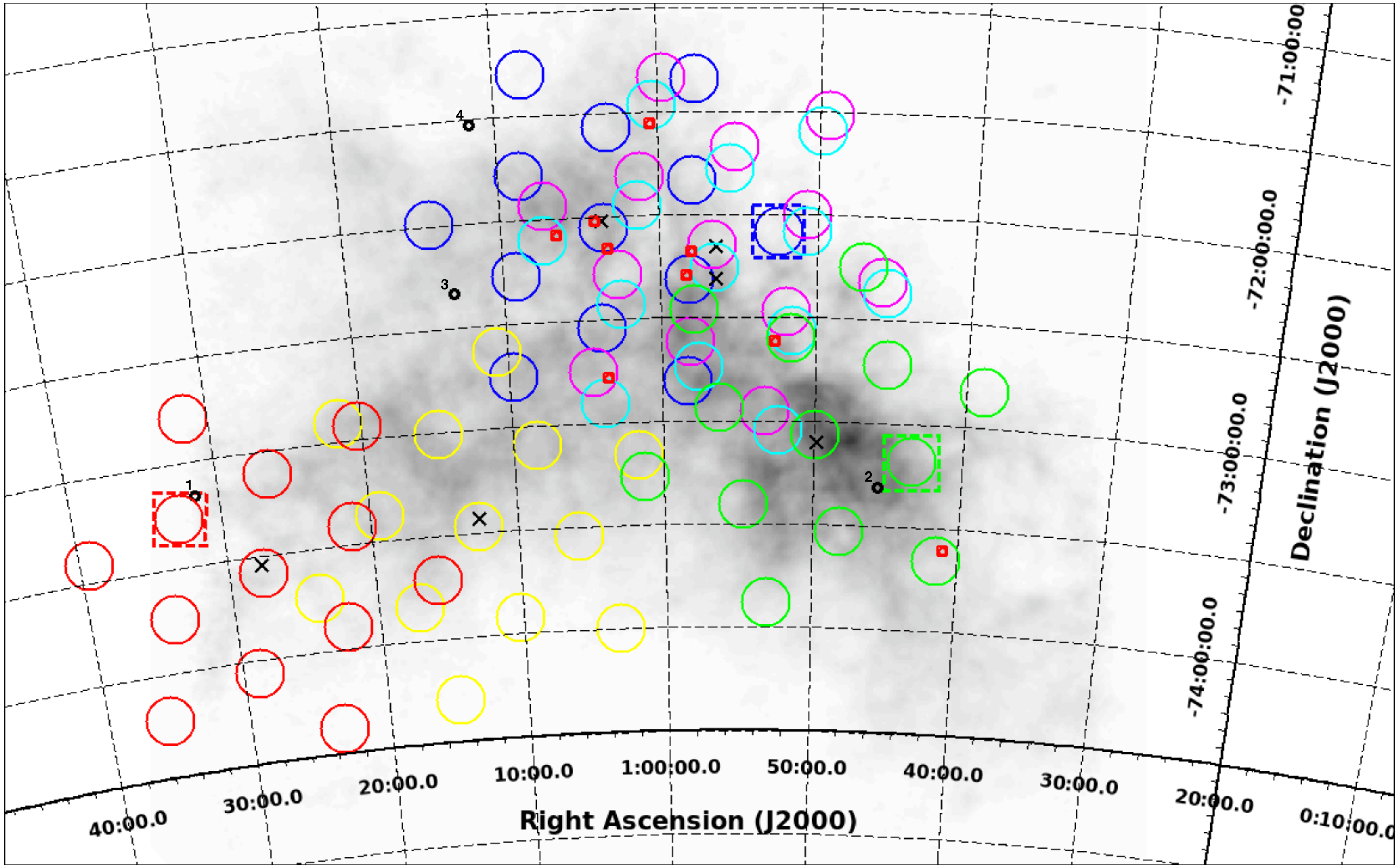

Figure 3.1: The coloured circles show the PMB orientation, where their 14 arcmin width is consistent with the half power beam width (HPBW) of the PMB beams (Table 3.1), and is superimposed on a HI map of the SMC (Stanimirovic et al. 1999). Furthermore, the locations of the five SNR candidates and MCSNR J0127−7332 are indicated by black crosses, and four of the known SMC radio pulsars are shown by black circles (1: PSR J0131−7310; 2: PSR J0045−7319; 3: PSR J0113−7220; 4: PSR J0111−7131; the fifth known pulsar is off the plot on the right hand corner). The nine additional SNRs and PWNe are highlighted with small red squares. The dashed squares indicate the beams within which pulsars were detected: PSR J0131−7310 (red square), the new pulsars, PSR J0043−73 (green square), and PSR J0052−72 (blue square).

Table 3.3: Observational setup of SMC radio pulsar surveys, as well as the limiting flux densities at 1400 MHz for $P \geq 50$ ms. The flux densities were calculated as outlined in Section 3.2.3

Survey	Pointings	T_{int} (s)	t_{samp} (μs)	$\Delta\nu$ (MHz)	S_{1400} (mJy)
Crawford et al. (2001)	NA	8 400	250	288	0.066
Manchester et al. (2006)	73	8 400	1 000	288	0.067
This work	12	15 000	64	400	0.039

pointing, as well as detect binary pulsars at a different orbital phase.

3.2.3 Survey Sensitivity

To compare our targeted survey with the previous blind surveys (Crawford et al. 2001, Manchester et al. 2006) we calculate the average, limiting flux density at 1400 MHz (S_{1400}) for each survey with the survey parameters recorded in Table 3.3. The average, fundamental limiting flux density for a survey is given by the radiometer equation

$$S_{\mathrm{lim}} = \frac{\sigma\beta T_{\mathrm{sys}}}{G\sqrt{n_{\mathrm{p}} t_{\mathrm{int}} \Delta\nu}}, \tag{3.1}$$

where the detection threshold, σ was chosen to be 8, and $\beta = 1.5$ for BPSR's 2-bit digitisation, which takes into account instrumental imperfections. For the PMB the mean system temperature is $T_{\mathrm{sys}} = 23$ K (McMahon 2008, Keith et al. 2010), while the central PMB's gain is $G = 0.735\ \mathrm{K\,Jy^{-1}}$, with the number of polarisations, $n_{\mathrm{p}} = 2$. The integration time (t_{int}) in seconds, and bandwidth ($\Delta\nu$) in MHz for the various surveys are recorded in Table 3.3. We used the same parameter values as outlined in Ridley et al. (2013) to calculate our sensitivity limits. The fundamental limiting flux density given by equation (3.1) for the Crawford et al. (2001) and Manchester et al. (2006) survey was 0.17 mJy, while our survey was more sensitive with a limiting flux density of 0.11 mJy.

These limits do not take into account the pulse width or broadening effects that must be accounted for, considering that a survey is not equally sensitive to all periods, pulse shapes, and DMs. We followed the methodology of Manchester et al. (2001) to model the frequency response of a pulsar. A series of pulses with frequency $f_{\mathrm{p}} = 1/P$, where P is the pulse period, is portrayed in the Fourier domain by the fundamental and 8 harmonics. The respective harmonics have an amplitude of $1/S_{\mathrm{lim}}$, which are multiplied by a sequence of functions representing the transformation the data will be subjected to. The first function accounts for the intrinsic pulse shape, which is modelled by a Gaussian with a width of $W_{50} = 0.05P$:

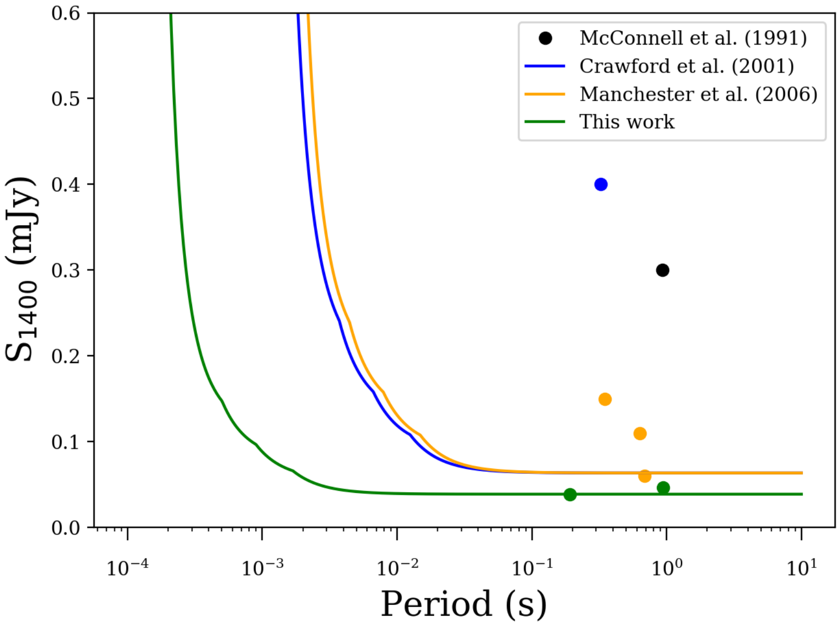

Figure 3.2: The 1400 MHz limiting flux densities for all SMC radio pulsar surveys. The filled circles represent the pulsars detected in the various surveys, in particular the green filled circles indicate the pulsars discovered in this survey (PSR J0043−73, PSR J0052−72).

$$g_1(f_\mathrm{p}) = \exp\left(-\frac{\pi^2 f_\mathrm{p}^2 {W_{50}}^2}{4\ln 2}\right). \tag{3.2}$$

The interstellar medium will then disperse the pulses, and cause a dispersion delay across a bandwidth of $\Delta\nu$, centred at a frequency of ν given by

$$\tau_\mathrm{DM} = 8.3 \times 10^3 \mathrm{DM}\Delta\nu\nu^{-3} s. \tag{3.3}$$

Thus, $g_2(f_\mathrm{p})$ is modelled by a similar Gaussian as in equation (3.2), but with W_{50} replaced with τ_DM. The final transformation has to account for the effect the finite sampling time (t_samp) has on the pulses, which is characterised by

$$g_3(f_\mathrm{p}) = \left|\frac{\sin(\pi f_\mathrm{p} t_\mathrm{samp})}{\pi f_\mathrm{p} t_\mathrm{samp}}\right|. \tag{3.4}$$

The final limiting sensitivity is given by summing over n harmonics, where $n \in \{1, 2, 4, 8\}$. Figure 3.2 shows the final limiting flux density for the various surveys at 1400 MHz for the average SMC DM of 116.4 pc cm^{-3}. It clearly shows our survey is the first to be sensitive to MSPs, and that for $P \geq 50$ ms our survey is twice as sensitive as the previous surveys. The respective flux densities for $P \geq 50$ ms are recorded in Table 3.3.

Table 3.4: Dedispersion parameters for young pulsar search.

Low DM ($\mathrm{pc\,cm^{-3}}$)	High DM ($\mathrm{pc\,cm^{-3}}$)	DM step ($\mathrm{pc\,cm^{-3}}$)	Down Sampling	Number DMs
0.00	196.80	0.10	1	1968
196.80	350.40	0.20	2	768
350.40	580.80	0.30	4	768
580.80	664.80	0.50	8	168

3.3 Data Reduction

3.3.1 Young Pulsar Search

The PMB data were searched for young pulsars (i.e. those with periods of a few tens of milliseconds) using routines from `PRESTO`* (Ransom et al. 2002). Radio frequency interference (RFI) masks were created for each beam using `rfifind` with the `blocks` parameter set to 30. We searched 3 672 DMs within a range of 0 − 660 $\mathrm{pc\,cm^{-3}}$ (Table 3.4), with no restrictions on the period parameter space. The dedispersed time series was barycentred to correct for the Earth's motion and then Fourier transformed with `realfft`. The resulting power spectra were searched for significant pulses, which were summed up to the 8th harmonic using `accelsearch` with `z = 0`, i.e. no acceleration searches were conducted. Finally, candidates above a S/N threshold of 4.0 were selected and folded with `prepfold`. The low threshold was chosen, since we can cross-match candidates between pointings of the same field. We also observed PSR J0024−7204C at the start of every observing day, apart from the 2017–08–29 observations. The test pulsar was recovered with blind `PRESTO` searches at an expected S/N of 22, for every observation except on the 2017–09–11, when the observation was subjected to severe RFI.

The search identified ~150 000 candidates, which were inspected by eye. Promising candidates were cross-checked with the alternate pointing of the same source on another day. If the candidate was not detected in the alternate pointing, the raw data were also folded with the identified period and DM.

3.3.2 Longer Period Pulsars

The Fast Fourier Transform (FFT) method employed by `PRESTO` for the young pulsar search is susceptible to red noise, since the power spectral density of red noise is inversely proportional to f^2, which implies it has more energy at lower frequencies. Furthermore van Heerden et al. (2017) showed that the sensitivity off FFT searches are significantly reduced for pulsars with

---

*https://www.cv.nrao.edu/~sransom/presto periods greater than 200 ms. To combat the effects of red noise we utilised a fast folding algorithm (FFA, Staelin 1969; Morello et al. 2019, in prep) to search for pulsars with periods from 200 ms – 360 s, and DMs from 0 – 400 pc cm^{-3} with DM steps of 2 pc cm^{-3}. The lower period limit was selected since the known pulsar distribution peaks at 200 ms, while the upper limit was the largest period we expect to have sufficient pulses to detect a pulsar. The data were dedispersed using `PRESTO`, while applying the same RFI masks created for the young pulsar search.

The FFA identified ~40 000 candidates, which were also inspected by eye. Acceptable candidates were cross matched with the alternate pointing in question, and folded with `PRESTO` using the period and DM identified by the FFA.

3.4 Results

We discovered two new pulsars, and identified 2 additional low signal to noise (S/N) candidates in our targeted survey of the SMC. We also detected the known PSR J0131−7310 (Manchester et al. 2006). We folded the raw data with `dspsr`, and then refined the periods, DMs and S/Ns with `pdmp`. The quoted values were obtained from `pdmp`, unless specified otherwise. Table 3.5 lists the pulsar properties and the PMB beam coordinates within which the pulsars were detected.

3.4.1 PSR J0131−7310

PSR J0131−7310 was detected in the 2017–08–25 pointing, focused on MCSNR J0127−7332. The pulsar was on the edge of one of the inner ring beams of the PMB (Figure 3.1, red square), with beam coordinates of RA = 01:32:46.87 and Dec = –73:16:21.80 (beam 5). We detected PSR J0131−7310 with a barycentric period of 348.12341 (18) ms, and a DM of 206.7 (1.5) pc cm^{-3}, matching well the Manchester et al. (2006) values for the period of 348.124045581 (7) ms and a DM of 205.2 pc cm^{-3}. PSR J0131−7310 was not detected in the second observation on 2017–09–11, but was detected again in the follow-up observation on 2017–12–13 with the `FFA`. Figure 3.3 shows the pulse profile of PSR J0131−7310 for the 2017–08–25 pointing.

3.4.2 PSR J0043−73

The first new SMC radio pulsar has a barycentric period of 937.42937 (26) ms and DM of 115.1 (3.4) pc cm^{-3}, which is consistent with the known SMC pulsar DM range (76 – 205 pc cm^{-3}). Hereafter the new pulsar will be referred to as PSR J0043−73 (Figure 3.1, green square). The

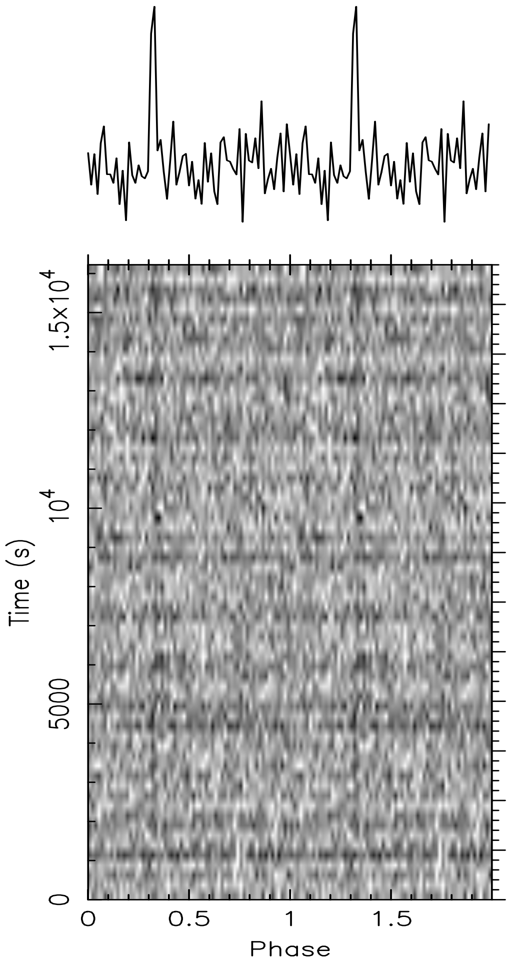

Figure 3.3: The integrated pulse profile (top panel) of PSR J0131−7310, as well as the pulse intensity as a function of pulse phase and integration time (grey scale). The pulses are plotted over two pulse phases.

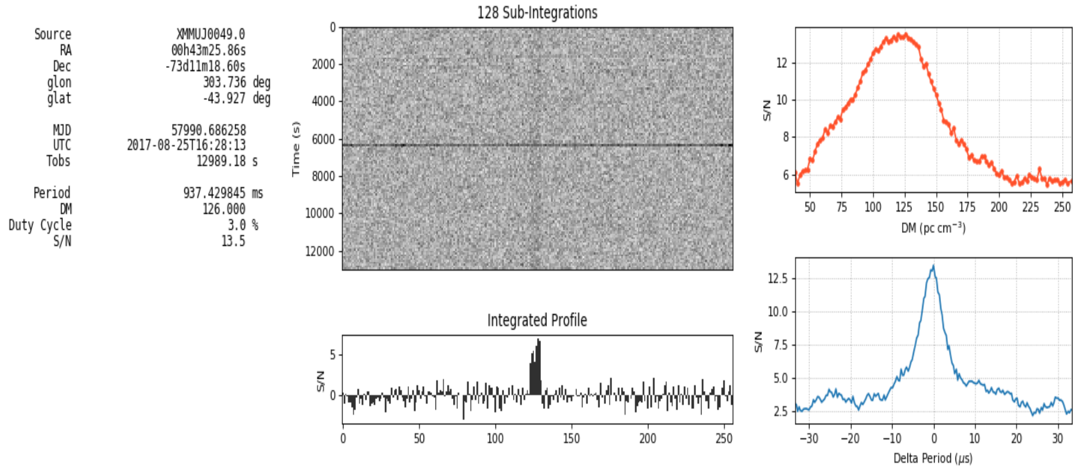

Figure 3.4: The FFA discovery plot of PSR J0043−73, which was located in beam seven of the XMMU J0049.0-7306 pointing on 2017–08–25. The bottom central panel show the integrated pulse profile. Following the discovery, we folded the raw data with `pdmp`, constraining the barycentric period to 937.42937 (26) ms and the DM to 115.1 (3.4) pc cm^{-3}. The pulsar was not detected in the initial young pulsar search with `PRESTO`.

pulsar was found in the 2017–08–25 pointing of which the XMMU J0049.0−7306 source was the focus, with beam coordinates of RA = 00:43:25.86 and Dec = –73:11:18.60 (beam 7), but not in the following observation on 2017-09-11. The pulsar was discovered using the FFA, but could clearly be seen in the `PRESTO` `prepfold` plot when folding the raw data with the identified period and DM. When we increased the number of summed harmonics to 16, `PRESTO` also identified PSR J0043−73 as a candidate pulsar. Figure 3.4 shows the FFA discovery plot. We used the archival Parkes data of the Manchester et al. (2006) survey, and used `prepfold` to fold the data at PSR J0043−73's period and DM, but did not recover the pulsar.

The known SMC pulsar, PSR J0045−7319 (Figure 3.1, black circle on left-hand corner edge of green square) has a similar period, but is located 33.24 arcmin from the centre of the beam within which PSR J0043−73 was found. This is nearly 5 times the HPBW radius, moreover PSR J0045−7319 has a period of 926.2 ms and a DM of 105.4 pc cm^{-3} (Crawford et al. 2001;Manchester et al. 2005*). Thus, we are confident that PSR J0043−73 is a new SMC radio pulsar.

3.4.3 PSR J0052−72

PSR J0052−72 (Figure 3.1, blue square) is the second new SMC pulsar (Figure 3.5) with a barycentric period of 191.444328 (46) ms and a DM of 158.6 (1.6) pc cm^{-3}. The pulsar was

---

*http://www.atnf.csiro.au/research/pulsar/psrcat

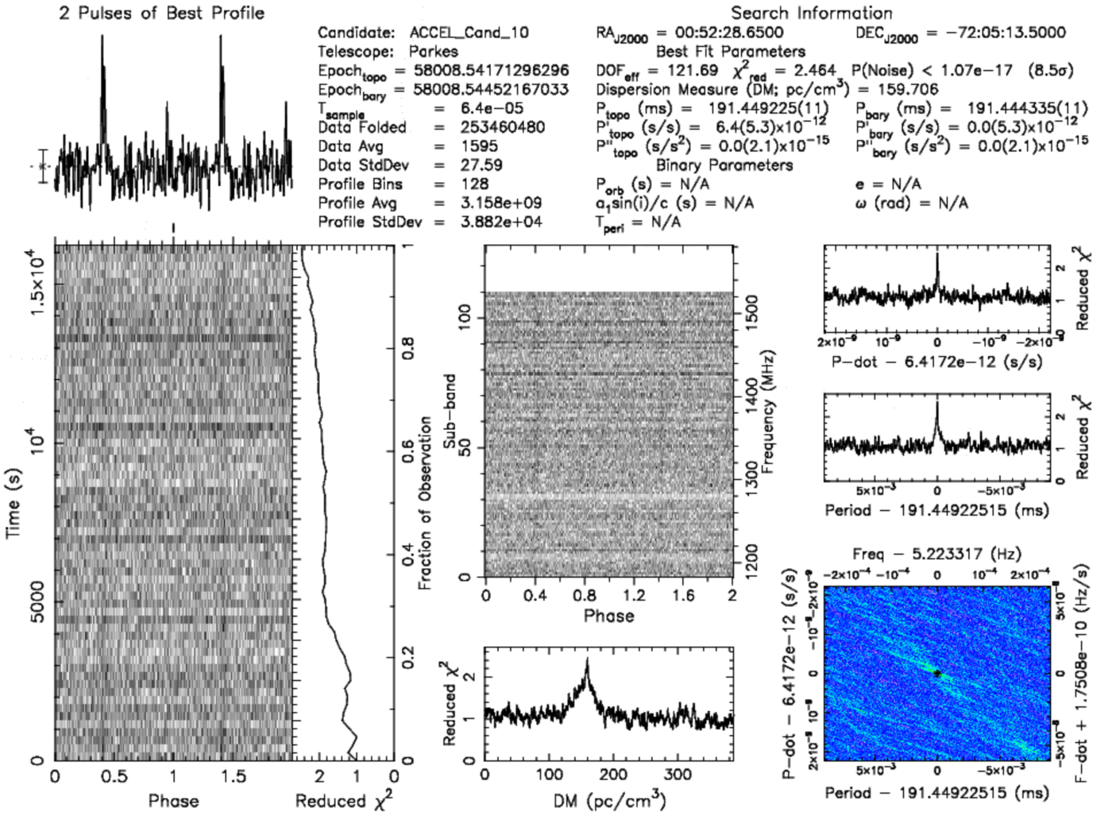

Search Information

Candidate: ACCEL_Cand_10
Telescope: Parkes
$\mathrm{Epoch_{topo}}$ = 58008.54171296296
$\mathrm{Epoch_{bary}}$ = 58008.54452167033
T_{sample} = 6.4e–05
Data Folded = 253460480
Data Avg = 1595
Data StdDev = 27.59
Profile Bins = 128
Profile Avg = 3.158e+09
Profile StdDev = 3.882e+04

$\mathrm{RA_{J2000}}$ = 00:52:28.6500 $\mathrm{DEC_{J2000}}$ = –72:05:13.5000

Best Fit Parameters

$\mathrm{DOF_{eff}}$ = 121.69 χ^2_{red} = 2.464 P(Noise) < 1.07e–17 (8.5σ)
Dispersion Measure (DM; pc/cm^3) = 159.706
P_{topo} (ms) = 191.449225(11) P_{bary} (ms) = 191.444335(11)
P'_{topo} (s/s) = 6.4(5.3)x10^{-12} P'_{bary} (s/s) = 0.0(5.3)x10^{-12}
P''_{topo} (s/s^2) = 0.0(2.1)x10^{-15} P''_{bary} (s/s^2) = 0.0(2.1)x10^{-15}

Binary Parameters

P_{orb} (s) = N/A e = N/A
$a_1\sin(i)/c$ (s) = N/A ω (rad) = N/A
T_{peri} = N/A

Figure 3.5: The `PRESTO` discovery plot of PSR J0052−72, which was located in beam eight of the SNR C3 pointing on 2017–09–12. PSR J0052−72 has a barycentric period to 191.444328 (46) ms and a DM of 158.6 (1.6) pc cm^{-3}.

detected in one of the outer ring beams (beam 8) of the 2017–09–12 data set, which was focused on SNR C3. The beam (RA = 00:52:28.65, Dec = -72:05:13.5) was intersected by two inner ring beams from XMMU J0056.6-7208 and SNR C2, but PSR J0052−72 was not detected in either of the beams. The FFA was adapted to search for the pulsar's period, and subsequently detected the pulsar as well. PSR J0052−72 was re-detected in the 2017–08–28 dataset (beam 9) with the FFA. We also used the archival Parkes data of the Manchester et al. (2006) survey that was coincident with this pointing, and folded the data at the period and DM of PSR J0052−72, but the pulsar was not detected in the dataset.

3.4.4 Candidate Pulsars

We detected two lower S/N candidates, but could not confirm them. One of the candidates was detected in the 2017–09–12 dataset foucsed on SNR C3, and the other in the 2017–09–28 dataset focused on SNR C9. The SNR C3 candidate had a period and DM of 21.03561023 (40) ms and 208.42 pc cm^{-3} respectively, while the SNR C9 candidate had period of 11.001403386 (76) ms

Table 3.5: Properties of detected and candidate pulsars discovered in this survey.

JName	Date	Beam	Epoch^a (J2000)	RA$_{beam}$^{b} (J2000)	Dec$_{beam}$^{b} (MJD)	P^c (ms)	DM (pc cm^{-3})	S$_{1400}$ (mJy)	Method (`PRESTO`/`FFA`)
PSR J0131−7310	2017–08–25	5	57990.50	01 32 46.87	-73 16 21.80	348.12341 (18)	206.7 (1.5)	0.157	FFA
PSR J0043−73	2017–08–25	7	57990.69	00 43 25.86	-73 11 18.60	937.42937 (26)	115.1 (3.4)	0.047	FFA
PSR J0052−72	2017–09–12	8	58008.54	00 52 28.65	-72 05 13.50	191.444328 (46)	158.6 (1.6)	0.039	`PRESTO`
SNR C3 candidate	2017–09–12	5	58008.54	01 09 08.68	-72 16 34.10	21.0356101 (55)	208.17 (66)	0.038	`PRESTO`
SNR C9 candidate	2017–09–28	5	58024.71	01 10 15.74	-73 55 33.00	11.0014027 (11)	342.08 (32)	0.043	`PRESTO`

[a] Observation Epoch is taken to be at the start of a particular observation.
[b] The PMB coordinates within which a pulsar was detected.
[c] This period refers to the barycentric period.

and a DM of 341.58 pc cm^{-3}. Both candidates were located in beam 5. We list the candidate pulsars in Table 3.5, and show the `prepfold` plots in Figure 3.6 and Figure 3.7.

3.5 Discussion

Two new SMC radio pulsars were discovered in our SMC SNR survey, increasing the SMC pulsar population to seven confirmed pulsars. Furthermore, two candidates have been identified, but could not be confirmed. The detected and candidate pulsar properties are shown in Table 3.5.

3.5.1 Detected pulsars

Our survey schedule enabled us to observe each target twice. In theory this would allow us to cross-match likely candidates, and so doing confirm candidates as pulsars when they are detected in both observations. We detected PSR J0052−72 in both pointings (2017–08–28 and 2017–09–12), however PSR J0043−73 was only detected in the first pointing on 2017–08–25. This was a result of more severe RFI, as well as red noise during the second pointing on 2017–09–11. In particular, mitigating the red noise effects for pulsars with periods greater than 200 ms is not a trivial task when a Fourier based pulsar search is implemented as shown by van Heerden et al. (2017). Thus, it is not suprising that we detected both pulsars, PSR J0131−7310 and PSR J0043−73, with the FFA and not initially in the Fourier based `PRESTO` search. Table 3.6 lists the properties of the now, seven SMC pulsars.

PSR J0131−7310

PSR J0131−7310 was detected at 20.55 arcmin from the centre of an inner ring beam, which was coincident with the first side lobe of beam five. Using the inner ring beam model of Ravi et al. (2016) we scaled the gain appropriately and calculated a flux density of 0.16 mJy for S/N = 11.90 and a pulse width of 4.20 ms. This is comparable to the 0.15 mJy flux density recorded for PSR J0131−7310 at 1400 MHz by Manchester et al. (2006).

Table 3.6: SMC pulsar parameters.

JName	P (ms)	DM (pc cm^{-3})	S_{1400} (mJy)	Discovery Ref.
J0043−73	937.42937 (26)	115.1 (3.4)	0.047	1
J0045−7042	632.33580002 (6)	70 (3)	0.11	2
J0045−7319	926.27590497 (3)	105.4 (7)	0.3	4
J0052−72	191.444328 (46)	158.6 (1.6)	0.039	1
J0111−7131	688.54151164 (5)	76 (3)	0.06	2
J0113−7220	325.88301613 (1)	125.49 (3)	0.4	3
J0131−7310	348.124045581 (7)	205.2 (7)	0.15	2

Discovery references: (1) This work, (2) Manchester et al. (2006), (3) Crawford et al. (2001), (4) McConnell et al. (1991).

PSR J0043−73

To calculate the flux density of PSR J0043−73 we used the radiometer equation with a S/N ratio of 18 and a pulse width of 25 ms, we determine $S_{1400} = 0.047$ mJy for an inner ring beam (Figure 3.2). We propose it as a new pulsar, in spite of a non-detection in the subsequent observation on 2017–09–11 when the data were compromised with severe RFI. This is also consistent with the non-detection of PSR J0131−7310 which was also observed on 2017–09–11.

PSR J0052−72

To calculate the flux density of PSR J0052−72 we used the radiometer equation with a S/N ratio of 11 and a pulse width of 8 ms, we determine $S_{1400} = 0.039$ mJy for an outer ring beam (Figure 3.2). This is the fastest spinning radio pulsar discovered in the SMC to date.

3.5.2 Non-detections

During this survey we observed 15 SNRs (candidates and confirmed), some of which are identified as PWNe. No pulsars were detected within any of these regions, but we can quantify flux density limits at a $8\,\sigma$ detection threshold for each of the sources, scaled by their distance from the centre of the beam in question (Table 3.7). We used the PMB beam model by Ravi et al. (2016) in combination with equation (3.1), and our survey parameters listed in Section 3.2.3, which we then multiplied by $\sqrt{\frac{W_{50}}{P-W_{50}}}$, and we set $W_{50} = 0.05P$.

SNR Candidates

Our deep, sensitive observations of MCSNR J0127−7332 and five SMC SNR candidates , identified by the XMM-Newton survey (Haberl et al. 2012), and optically selected by MCELS

Table 3.7: Properties of all SNRs/PWNe observed during our survey. The first six entries was the focus of our survey, which included the known SNR, MCSNR J0127−7332, and the five SNR candidates. The remaining SNRs/PWNe are listed in Filipović et al. (2008).

SNR	Pointing	RA_{SNR}[a] (J2000)	Dec_{SNR}[a] (J2000)	RA_{beam}[b] (J2000)	Dec_{beam}[b] (J2000)	D_{extent}[c] (arcmin)	d_{centre}[d] (arcmin)	S_{1400}[e] (mJy)	Type (SNR/PWN)
MCSNR J0127-7332	MCSNR J0127-7332	01 27 45.95	-73 32 56.30	01 27 37.66	-73 35 20.50	-	3.17	0.024	SNR
XMMU J0049.0-7306	XMMU J0049.0-7306	00 49 46.00	-73 06 17.00	00 49 54.48	-73 04 09.70	0.75	2.21	0.027	SNR
SNR C3	SNR C3	01 03 35.56	-72 01 35.10	01 03 27.99	-72 03 41.30	1.38	2.18	0.024	SNR
SNR C2	SNR C2	00 56 25.00	-72 19 05.00	00 56 31.02	-72 15 48.40	3.72	3.31	0.026	SNR
XMMU J0056.6-7208	XMMU J0056.6-7208	00 56 26.00	-72 09 42.00	00 56 37.69	-72 09 01.40	4.02	1.12	0.024	SNR
SNR C9	SNR C9	01 12 37.00	-73 26 05.00	01 12 39.07	-73 28 15.40	5.85	2.18	0.025	SNR
DEM S5	XMMU J0049.0-7306	00 41 00.10	-73 36 30.00	00 41 24.24	-73 39 24.80	2.66	3.39	0.035	PWN
B0050-72.8	XMMU J0049.0-7306	00 52 36.90	-72 37 18.50	00 51 35.18	-72 36 02.30	2.41	4.79	0.042	SNR
IKT 16	SNR C3	00 58 17.80	-72 18 07.40	00 58 06.93	-72 19 17.60	3.32	1.43	0.036	PWN
IKT 21	SNR C3	01 03 17.00	-72 09 45.00	01 03 27.99	-72 03 41.30	1.20	6.12	0.026	SNR
1E0102-723	SNR C3	01 04 01.20	-72 01 52.30	01 03 27.99	-72 03 41.30	0.34	3.14	0.024	SNR
B0058-71.8	SNR C2	01 00 23.90	-71 33 41.10	01 00 19.47	-71 28 15.00	3.50	5.45	0.036	SNR
IKT 25	SNR C2	01 06 27.50	-72 05 34.50	01 07 23.94	-72 06 41.50	1.13	4.45	0.035	SNR
N S66D	XMMU J0056.6-7208	00 58 00.00	-72 11 01.40	00 56 37.69	-72 09 01.40	3.34	6.61	0.027	SNR
HFPK 334	XMMU J0056.6-7208	01 03 29.50	-72 47 23.20	01 04 25.17	-72 45 33.80	1.00	4.51	0.032	SNR

[a] The SNR coordinates.

[b] The PMB coordinates within which the SNR was located.

[c] D_{extent}: the angular extent of the SNR.

[d] d_{centre}: The distance from the centre of the SNR to the centre of the particular PMB beam.

[e] S_{1400}: The flux density values are calculated based on d_{centre} for $\sigma = 8$.

(Smith & MCELS Team 1999) and SALT Fabry-Perot observations, did not reveal any coincident radio pulsars. The size of each SNR candidate was less than the HPBW of the central PMB, thus the SNR candidates were each observed in their entirety in a single pointing. The sensitivity limit for each SNR candidate and MCSNR J0127−7332 is listed in the first six lines of Table 3.7.

MCSNR J0127−7332 and SNR C3 Pointings

The MCSNR J0127−7332 and SNR C3 pointings were coincident with SXP 1062 and SXP 1323 respectively. Both these X-ray pulsars have extraordinarily long spin periods and are potentially associated with SNRs. In particular, NSs are typically born with spin periods of tens of milliseconds of (e.g. Crab and Vela pulsars), however Ikhsanov (2012) found that a young NS can possibly be spun down within 10^4 years by accreting matter from a magnetic wind, if the NS has a magnetic field of $\sim 10^{13}$ G. Alternatively, Fu & Li (2012) as well as Ho & Andersson (2017) showed that both accreting and isolated NSs with a $B > 10^{14}$ G (i.e. a magnetar) can spin down to $P > 1000$ s within the lifetime of a SNR.

I) MCSNR J0127-7332 Pointing

SXP 1062 is a transient Be\X-ray binary (BeXB) with an orbital period of 668 days, a lower limit eccentricity of 0.4, and a X-ray spin period of 1086 s (González-Galán et al. 2018). SXP 1062 has been spinning down from a period of 1062 s in 2010 to 1086 s in 2014. This is the second longest spin period known for a BeXB. If MCSNR J0127-7332 is the natal SNR of SXP 1062 it implies a kinematic age of $\sim$2-4$\times 10^4$ years for the NS (Hénault-Brunet et al. 2012). This contradicts standard models, which suggests that NSs at this age are too young to enter an accretion phase, and as a result cannot be X-ray pulsars (Lipunov 1992). SXP 1062 is in some aspects similar to the highly eccentric gamma-ray binary system PSR B1259−63, which has a young radio pulsar of $P \sim 47$ ms (Johnston et al. 1992) with a characteristic age of 3.32×10^5 years in orbit around a Be star. The system has a similarly long orbital period of 1236.7 days, and an eccentricity of 0.87 (Wang et al. 2004). We searched MCSNR J0127−7332 for radio pulsations at the X-ray spin period of SXP 1062, but did not detect any pulsations. The limiting flux density of this pointing was 0.024 mJy (Table 3.7).

II) SNR C3 Pointing

SXP 1323 is another peculiar BeXB with a 26.2 day orbital period, and a X-ray spin period of 1100 s (Carpano et al. 2017). SXP 1323 has the longest spin period known for any accreting X-ray pulsar, but has been rapidly spun up in a period between 2006 and 2016 from 1340 s to 1100 s. Recently, Gvaramadze et al. (2019) found evidence for a putative SNR centred on

SXP 1323. They identified the SNR with optical studies, however it is the same SNR discovered by XMM-Newton and referred to as SNR C3 in this paper. If the SNR is associated with SXP 1323 then the NS's age is estimated to be 4×10^4 years, similar to SXP 1062's age. This would be the second, long period X-ray pulsar located in its natal SNR, and interestingly both are hosted in the low metallicity environment of the SMC. However, SXP 1323 has a much shorter orbital period than SXP 1062, and subsequently could accrete matter more often. Accretion typically inhibits radio pulsations, and indeed we did not detect any radio pulsations at the X-ray spin period.

Furthermore, the SNR C3 pointing included 2 confirmed SNRs (1E0102-723, IKT 21) in the central beam, as well as IKT 16 in the second beam. 1E0102-723 was first detected in the X-rays by Seward & Mitchell (1981), and then identified by Dopita et al. (1981) as an oxygen rich SNR with narrow band optical imaging. In a subsequent study, Vogt et al. (2018) identified an isolated neutron star with characteristics consistent with a central compact object (CCO). From their study the CCO is likely associated with 1E0102-723, thus one would not expect to dectect radio pulsations from 1E0102-723, since CCOs are radio quiet. Conversely, IKT 16 has been confirmed as a PWN with a hard X-ray point source (Maitra et al. 2015). In particular, the X-ray spectral index of 1.1 implies that the emission is dominated by non-thermal emission originating from a pulsar. The expected spin down power of 10^{37} erg s^{-1} suggests the existence of a ~100 ms pulsar. Down to the 1400 MHz flux limit of 0.024 mJy we did not detect any pulsations, thus the pulsar must be either too faint or not beaming towards us.

A pulsar BeXB system, SAX J0103−722 with a X-ray spin period of 345 s (Hughes & Smith 1994, Israel et al. 2000, van der Heyden et al. 2004), is coincident with IKT 21. However, it is not clear whether SAX J0103-722 is associated with IKT 21 or merely a chance coincidence. Hughes & Smith (1994) argued that a spatial chance coincidence in the SMC is highly unlikely, and would require a transverse spatial velocity exceeding 100 km s^{-1} if the NS of SAX J0103−722 was born by the same supernova explosion that resulted in the formation of IKT 21. Such a large spatial velocity for a BeXB is improbable*. Instead, the study suggests the SN explosion occurred in an OB association which also harbours SAX J0103−722. Nonetheless, we did not detect any radio pulsars down to a flux limit of 0.026 mJy.

XMMU J0049.0-7306 Pointing

The XMMU J0049.0−7306 pointing included DEM S5 and B0050−72.8 (Table 3.7). The nature of the compact object originating from the precursor SN explosion is not known for B0050−72.8, nor has any candidates been identified. We did not detect any radio pulsations

---

*BeXBs typically have spatial velocities of ~10 km s^{-1} (see Kaper 2001 and references therein) down to a sensitivity of of 0.042 mJy. Alsaberi et al. (2019) has confirmed DEM S5 as a PWN, with a morphological structure analogous to PSR B1951+32 in SNR CTB 80 (Safi-Harb et al. 1995) and 'the mouse' (Camilo et al. 2002). Although this discovery confirms the likely existence of a radio pulsar, we did not detect any radio pulsations down to a flux density of 0.035 mJy.

SNR C2 Pointing

The SNR C2 pointing included B0058−71.8 and IKT 25 in the outer ring beams of the PMB (Table 3.7). B0058−71.8 has not been studied in detail, and we did not detect any radio pulsations at a flux limit of 0.036 mJy. Conversely, IKT 25 was likely produced by a thermonuclear (Type Ia) supernova (Roper et al. 2015, Lee et al. 2011), thus one would not expect a NS to form, and thus one would not expect a radio pulsar residing in the SNR, and indeed we did not detect radio pulsations down to a sensitivity of 0.035 mJy.

XMMU J0056.6-7208 Pointing

N S66D was located on the edge of the central beam during the XMMU J0056.6-7208 pointing, while HFPK 334 was positioned in one of the outer ring beams of the PMB. N S66D is poorly studied, consequently no additional information is available in the literature. On the contrary HFPK 334 is a young (≤ 1800 years) (Crawford et al. 2014), intriguing SNR emitting X-ray and radio emission, but not detectable in the optical (Payne et al. 2007). Filipović et al. (2008) noted a central point source within HFPK 334, and suggested that it may be indicative of a PWN. In light of their study Crawford et al. (2014) conducted a X-ray study of the central object, but could not identify it as either a CCO or a pulsar, thereupon they proposed that the central point source is a background object. The lack of any radio pulsations in our study down to a flux limit of 0.032 mJy, supports their theory that the central source is a background object.

3.6 Conclusions

We report the first pulsar discoveries in the SMC since the Manchester et al. (2006) survey. We discovered PSR J0043−73, a 937.42937 ms pulsar with DM = 115.1 pc cm^{-3}, as well as the fastest spinning pulsar to date in the SMC, PSR J0052−72 with P = 191.444328 ms and DM = 158.6 pc cm^{-3}. These discoveries increases the SMC radio pulsar population to seven, corresponding to a 40% increase in the population. To date no radio pulsar SNR association has been made in the SMC.

Acknowledgements

The Parkes radio telescope is part of the Australia Telescope which is funded by the Commonwealth of Australia for operation as a National Facility managed by CSIRO. NT, VMc, and DAHB acknowledges support of the National Research Foundation of South Africa (grants 98969, 93405, and 96094). BWS, VM and MC acknowledge funding from the European Research Council (ERC) under the European Union's Horizon 2020 research and innovation programme (grant agreement No. 694745).

3.7 Appendix

3.7.1 Pulsar candidates

Here follows the `prepfold` plots for two pulsar candidates found during the young pulsar search with `PRESTO`.

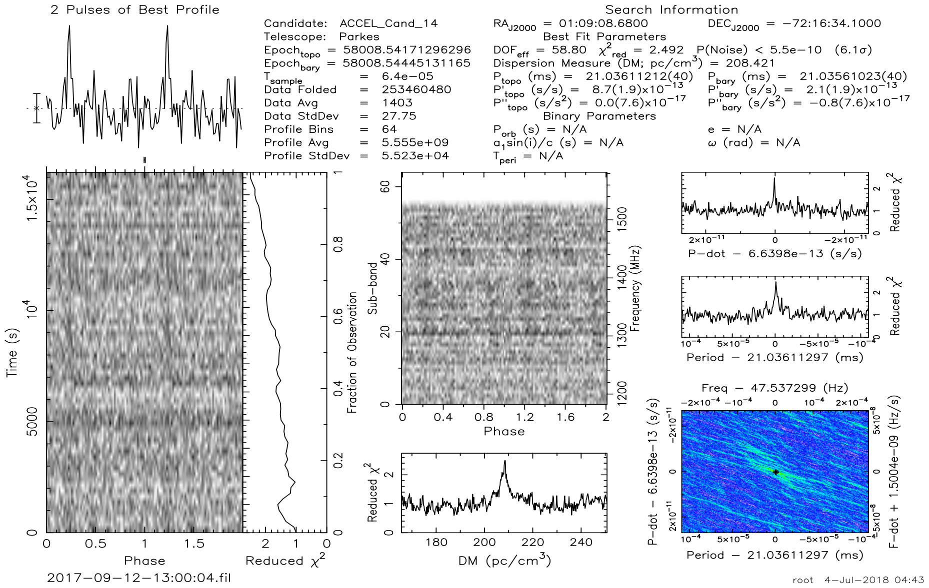

```
Candidate:  ACCEL_Cand_14
Telescope:  Parkes
Epoch_topo = 58008.54171296296
Epoch_bary = 58008.54445131165
T_sample         =  6.4e-05
Data Folded      =  253460480
Data Avg         =  1403
Data StdDev      =  27.75
Profile Bins     =  64
Profile Avg      =  5.555e+09
Profile StdDev   =  5.523e+04
```

```
Search Information
RA_J2000 = 01:09:08.6800                  DEC_J2000 = -72:16:34.1000
Best Fit Parameters
DOF_eff = 58.80  χ²_red = 2.492  P(Noise) < 5.5e-10  (6.1σ)
Dispersion Measure (DM; pc/cm³) = 208.421
P_topo (ms) =  21.03611212(40)      P_bary (ms) =  21.03561023(40)
P'_topo (s/s) =  8.7(1.9)x10^-13    P'_bary (s/s) =  2.1(1.9)x10^-13
P''_topo (s/s²) = 0.0(7.6)x10^-17   P''_bary (s/s²) = -0.8(7.6)x10^-17
Binary Parameters
P_orb (s) = N/A                     e = N/A
a_1sin(i)/c (s) = N/A               ω (rad) = N/A
T_peri = N/A
```

Figure 3.6: This candidate was detected during a SNR C3 pointing on 2017–09–12. The candidate was located in beam five.

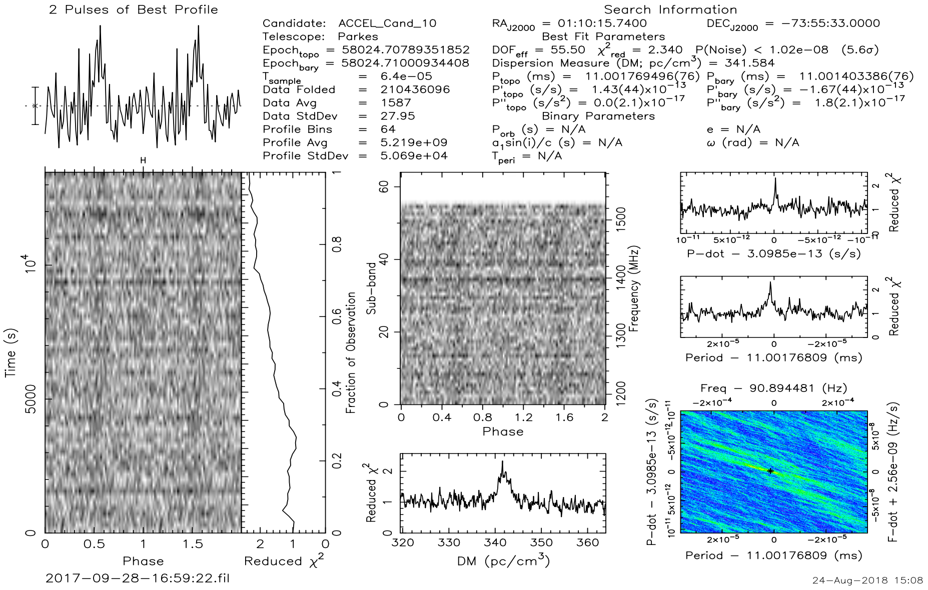

2 Pulses of Best Profile

Search Information

Candidate: ACCEL_Cand_10
Telescope: Parkes
$\mathrm{Epoch_{topo}}$ = 58024.70789351852
$\mathrm{Epoch_{bary}}$ = 58024.71000934408
$\mathrm{T_{sample}}$ = 6.4e−05
Data Folded = 210436096
Data Avg = 1587
Data StdDev = 27.95
Profile Bins = 64
Profile Avg = 5.219e+09
Profile StdDev = 5.069e+04

$\mathrm{RA_{J2000}}$ = 01:10:15.7400
$\mathrm{DEC_{J2000}}$ = −73:55:33.0000

Best Fit Parameters
$\mathrm{DOF_{eff}}$ = 55.50 χ^2_{red} = 2.340 P(Noise) < 1.02e−08 (5.6σ)
Dispersion Measure (DM; pc/cm^3) = 341.584
$\mathrm{P_{topo}}$ (ms) = 11.001769496(76) $\mathrm{P_{bary}}$ (ms) = 11.001403386(76)
$\mathrm{P'_{topo}}$ (s/s) = 1.43(44)x10^{-13} $\mathrm{P'_{bary}}$ (s/s) = −1.67(44)x10^{-13}
$\mathrm{P''_{topo}}$ (s/s^2) = 0.0(2.1)x10^{-17} $\mathrm{P''_{bary}}$ (s/s^2) = 1.8(2.1)x10^{-17}

Binary Parameters
$\mathrm{P_{orb}}$ (s) = N/A
e = N/A
$\mathrm{a_1 sin(i)/c}$ (s) = N/A
ω (rad) = N/A
$\mathrm{T_{peri}}$ = N/A

Figure 3.7: This candidate was detected during a SNR C9 pointing on 2017–09–28. The candidate was found in beam five.

Chapter 4

The radio pulsar population of the Small Magellanic Cloud

Abstract

We model the present day, observable, normal radio pulsar population of the Small Magellanic Cloud (SMC). The pulsars are generated with `SeBa`, a binary population synthesis code that evolves binaries and the constituent stellar objects up to remnant formation and beyond. We define a neutron star as a radio pulsar based on a selection of models defined by Galactic pulsars, and apply the detection thresholds of previous and future SMC pulsar surveys. The number of synthesised and recovered pulsars are exceptionally sensitive to the assumed star formation history and applied radio luminosity model, but is not affected extensively by the assumed common envelope model, metallicity, and neutron star kick velocity distribution. We estimate that the SMC formed $(1.6 \pm 0.3) \times 10^4$ normal pulsars during the last 100 Myrs. We study which pulsars may be observed by the Manchester et al. (2006) survey, by applying the survey's specific selection effects, and recover 4.0 ± 0.8 synthetic pulsars. This is in excellent agreement with their five observed pulsars. We also apply a proposed MeerKAT configuration for the upcoming SMC survey, and predict that the MeerKAT survey will detect 17.2 ± 2.5 pulsars.

4.1 Introduction

The Small Magellanic Cloud (SMC) is an excellent candidate to study a variety of stellar populations, since it is located out of the Galactic plane, providing minimal extinction, yet being close enough to resolve stars across the whole galaxy. Another advantage is the known distance to the SMC, necessary for the calculation of luminosities that lead to accurate classifications of stellar populations. The SMC is on average at a distance of 60 kpc (Graczyk et al. 2014), however it is believed to have a line of sight depth of ~10 kpc (Crowl et al. 2001). This uncertainty introduces a minimal uncertainty of ~30% for the calculated luminosities. For reasons such as these the SMC has been surveyed extensively at all wavelengths, producing representative samples of the various underlying stellar populations, within the constraints of the surveys.

The SMC contains a variety of neutron star (NS) populations that highlight various evolutionary stages in the lives of massive stars and massive binaries. The radio pulsar population of the SMC is of particular interest, since only seven pulsars have been discovered by previous surveys (McConnell et al. 1991, Crawford et al. 2001, Manchester et al. 2006, Titus et al. 2019). Although these surveys optimised survey sensitivity and coverage, they were only sensitive enough to detect the brightest pulsars due to the large distance to the SMC. In contrast to the small radio pulsar population, the SMC contains 137 high mass X-ray binaries (HMXBs) of which ∼60 are confirmed NS X-ray pulsars (Haberl & Sturm 2016, Antoniou et al. 2019). The previous X-ray surveys of the SMC (e.g. Yokogawa et al. 2000; Haberl & Pietsch 2004; Shtykovskiy & Gilfanov 2005; Sturm et al. 2013; Antoniou et al. 2019) were sensitive enough to probe accreting NSs in quiescence and outburst, unveiling a representative sample of the underlying X-ray binary population. Population synthesis studies can establish if the relatively small numbers of radio pulsars are an underlying property of the NS population of the SMC, or to what extent observational biases and constraints are affecting the observed radio pulsar population. The population synthesis results can be compared to previous radio pulsar surveys and population studies of the SMC (Ridley & Lorimer 2010), as well as predict the number of pulsars that future surveys should detect, like MeerKAT or SKA.

The star formation history of the SMC plays a critical role when simulating the observable normal radio pulsar[*] population. However, it is only the most recent star formation episodes (SFEs) that will contribute to the observable pulsar population, since the average lifetime of an isolated radio pulsar is ∼100 Myr (Faucher-Giguère & Kaspi 2006, Ridley & Lorimer 2010). During every SFE a population of massive stars will be born. Multiplicity studies of massive stars indicate that most massive stars are born in binaries (Kobulnicky & Fryer 2007, Kouwenhoven et al. 2007, Sana et al. 2012; 2014, Moe & Di Stefano 2017). Binarity will impact the evolution of the constituent stars if they exchange material. An isolated massive star will evolve to the giant phase, and produce a NS during a core collapse supernova (Type Ib/c; Heger et al. 2003). However massive stars in close binaries exchange material, forming at least one helium star, leading to a core collapse supernova and likely the formation of a NS (Yoon et al. 2010). NSs form via different evolutionary paths, and are born with a range of birth spin periods and magnetic fields. Moreover, if the NS is not accreting matter from a companion, it can enter a radio pulsar phase. The radio pulsar mechanism can switch on if the NS has a fast enough spin period, and a sufficiently strong surface magnetic field, resulting in highly beamed, coherent

---

[*] Normal pulsars refer to non-accreting, non-millisecond pulsars.

radio emission from the magnetic poles.

Given the prevalence of binarity in massive star populations, we conducted binary population synthesis studies to best simulate the events leading up to the formation of radio pulsars as well as the evolution of the pulsars. In this paper we present our population synthesis results of the SMC radio pulsar population and predict the number of pulsars MeerKAT will detect. In Section 4.2, we describe the simulation parameters and define a radio pulsar within the simulations. In Section 4.3 we present the results, and discuss their implications in Section 4.4. In Section 4.5 we draw our conclusions.

4.2 Method

We utilised the binary population synthesis code `SeBa` (Portegies Zwart & Verbunt 1996, Toonen et al. 2012, Toonen & Nelemans 2013) to model the evolution of massive binaries and the formation of isolated and radio pulsars in binaries. `SeBa` evolves the binaries from the zero age main sequence to remnant formation. Beyond remnant formation `SeBa` continues to evolve the individual remnants, as well as the binary interaction for the remaining binaries. The binary interaction accounts for mass loss, mass transfer, angular momentum loss, common-envelope (CE) phase, magnetic braking, gravitational radiation, and disruption, which is applied at every time step with the relevant recipes (see Portegies Zwart & Verbunt 1996; Portegies Zwart & Yungelson 1998). For this study pertaining to radio pulsars, we limit our selection of sources to detached and disrupted binaries containing a NS. A detached binary implies there is no mass transfer via Roche lobe overflow (RLOF), however mass transfer via wind accretion is still allowed. A disrupted binary is defined as a system that is no longer gravitationally bound as a consequence of a supernova explosion.

4.2.1 Initial Conditions of default model

We simulated 3 million binaries with `SeBa` to ensure a statistically significant population of radio pulsars. Here follows a list of the initial conditions required for our default model to simulate the population of binaries. For the CE evolution we used the $\gamma\alpha$ model (see Equation 4.1, Section 4.2.2) with a combined CE parameter $\alpha_{\rm CE}\lambda = 0.25$ (Toonen & Nelemans 2013), where $\gamma = 1.75$ (Portegies Zwart & Yungelson 1998, Toonen et al. 2012, van Haaften et al. 2015). The initial primary masses (M_1 stars with the potential of forming NSs) are drawn from a Kroupa initial mass function (IMF, Kroupa 2001) with exponent 2.3 for masses between 4.4 and 40 $\mathrm{M}_{\odot}$. Both mass limits were chosen to include all possible NS formation scenarios. The lower mass limit was calculated by simulating 500 000 binaries and determining the minimum primary mass required to form a NS. The secondary masses (M_2) are drawn from a uniform mass ratio distribution such that $0 < \frac{M_2}{M_1} < 1$ (Raghavan et al. 2010, Duchêne & Kraus 2013). The semi-major axis follows a uniform distribution in $\log a$ (Abt 1983) with a maximum cut off value of $1\times10^6\,R_\odot$. The initial eccentricity values are selected from a thermal distribution (Heggie 1975) ranging between zero and one. The natal NS kick velocity distribution is modelled by Verbunt et al. (2017), a combination of two Maxwellians with a mean of 75 km s^{-1} and 316 km s^{-1}. For the birth NS spin period, we assume a normal distribution with a mean of 300 ms and a standard deviation of 150 ms (Faucher-Giguère & Kaspi 2006), while the birth magnetic field in units of G is drawn from a lognormal distribution with a mean and standard deviation of 12.65 and 0.55 respectively (Faucher-Giguère & Kaspi 2006). The NS kick velocity, natal spin period and magnetic field distributions were determined from Galactic pulsars. We set the metallicity (Z) to 0.004*, and assume a 100% binary fraction.

4.2.2 Sensitivity to initial conditions

To assess the systematic uncertainty of sensitivity to the initial conditions we explore the effect various parameters and models have on the number of formed and detected radio pulsars. We vary the metallicity, CE model, combined CE parameter ($\alpha_{\rm CE}\lambda$), and the NS kick velocity distribution. For every combination of parameters and models we simulate 3 million binaries. A summary of all the simulations can be found in Table 4.1.

Common-envelope model

The CE phase is a short-lived phase in the life of a binary that occurs when an evolved donor extends beyond its Roche lobe, enabling unstable mass transfer leading to the formation of a CE (see Ivanova et al. 2013, and references therein). During the CE phase the binary orbit shrinks as angular momentum is transferred to the envelope, expelling material from the binary. Although the CE phase is critical for the formation of compact binaries, the processes governing the CE phase are poorly understood.

For population studies the CE evolution is typically modelled by a parametric model such as the $\alpha-$formalism that is based on the binary's energy budget (Paczynski 1976, Webbink 1984, de Kool et al. 1987, Livio & Soker 1988, de Kool 1990):

$$E_{\rm bin} = \frac{G M_{\rm d} M_{\rm c}}{\lambda R} = \alpha_{\rm CE} E_{\rm orbit}, \tag{4.1}$$

where G is Newton's gravitational constant, $M_{\rm d}$ the mass of the donor, $M_{\rm c}$ the mass of its core, R the donor's radius, while λ and $E_{\rm bin}$ refers to the structure parameter and binding energy of the envelope respectively. The orbital energy ($E_{\rm orbit}$) is the source that unbinds the envelope

---

*$Z_{SMC} = \frac{Z_\odot}{5} = \frac{0.02}{5} = 0.004$ (see Vagnozzi 2017 for $Z_\odot$ measurement).

Table 4.1: Summary of all the independent `SeBa` simulations with their corresponding parameters and models. The default model is printed in bold.

Model	Z	CE model	$\alpha_{\rm CE}\lambda$	NS kick velocity
V4CE2	0.004	$\gamma\alpha$ or $\alpha\alpha$	2.00	Verbunt et al. (2017)[a]
H4CE2	0.004	$\gamma\alpha$ or $\alpha\alpha$	2.00	Hobbs et al. (2005)[b]
V4CE25	**0.004**	$\boldsymbol{\gamma\alpha}$ or $\alpha\alpha$	**0.25**	**Verbunt et al. (2017)**
H4CE25	0.004	$\gamma\alpha$ or $\alpha\alpha$	0.25	Hobbs et al. (2005)
0.1V4CE2	0.004	$\gamma\alpha$ or $\alpha\alpha$	2.00	0.1 × Verbunt et al. (2017)[c]
0.1V4CE25	0.004	$\gamma\alpha$ or $\alpha\alpha$	0.25	0.1 × Verbunt et al. (2017)
V8CE2	0.008	$\gamma\alpha$ or $\alpha\alpha$	2.00	Verbunt et al. (2017)
H8CE2	0.008	$\gamma\alpha$ or $\alpha\alpha$	2.00	Hobbs et al. (2005)
V8CE25	0.008	$\gamma\alpha$ or $\alpha\alpha$	0.25	Verbunt et al. (2017)
H8CE25	0.008	$\gamma\alpha$ or $\alpha\alpha$	0.25	Hobbs et al. (2005)
0.1V8CE2	0.008	$\gamma\alpha$ or $\alpha\alpha$	2.00	0.1 × Verbunt et al. (2017)
0.1V8CE25	0.008	$\gamma\alpha$ or $\alpha\alpha$	0.25	0.1 × Verbunt et al. (2017)

[a] Verbunt et al. (2017): a combination of two Maxwellians with a mean of 75 km s^{-1} and 316 km s^{-1}.
[a] Hobbs et al. (2005): a single Maxwellian with mean of 265 kms^{-1}.
[c] 0.1 × Verbunt et al. (2017): reducing the NS kick velocity drawn from Verbunt et al. (2017) by a factor of 10.

with an efficiency of $\alpha_{\rm CE}$. This formalism is referred to as the $\alpha\alpha$ model in the paper. For the $\alpha\alpha$ model we set $\alpha_{\rm CE}\lambda = 0.25$ or $\alpha_{\rm CE}\lambda = 2$. The first was determined for systems that go through a single CE phase, forming white dwarf main sequence binaries (Zorotovic et al. 2010; 2014, Toonen & Nelemans 2013, Camacho et al. 2014), while the second relates to systems subjected to two CE phases leading to the formation of double white dwarf binaries (Nelemans et al. 2000, 2001b).

Another CE formalism is the $\gamma-$formalism that relates to angular momentum conservation of the binary (Nelemans et al. 2000):

$$\frac{J_{\rm init} - J_{\rm init}}{J_{\rm init}} = \gamma \frac{\Delta M_{\rm d}}{M_{\rm d} \;\; M_a}, \tag{4.2}$$

where $J_{\rm init}$ and $J_{\rm init}$ are the angular momentum of the binary prior to and following the CE phase respectively, while M_a refers to the mass of the companion. In our models we set $\gamma = 1.75$. This is applied unless the binary contains a compact object or the CE phase is triggered by a tidal instability rather than dynamically unstable Roche lobe overflow (see Toonen & Nelemans 2013). When this is not the case we implement the $\alpha\alpha$ CE model where $\alpha_{\rm CE}\lambda = 0.25$ or $\alpha_{\rm CE}\lambda = 2$ (Nelemans et al. 2001). We refer to this as the $\gamma\alpha$ model. For our default model, indicated in bold face in Table 4.1, we assume the $\gamma\alpha$ formalism and set $\alpha_{\rm CE}\lambda = 0.25$, since we are expecting the majority of the pulsars in binaries to have main sequence companions.

Neutron star kick velocities

A high mass star ending its life with a core-collapse (CC) supernova will form a NS, and impart a kick to the newly formed remnant. The mechanism responsible for NS kicks are not well defined, nonetheless they are thought to be related to asymmetric mass loss during SNe or, alternatively to anisotropic neutrino emission (Lai 2001, Hobbs et al. 2005, Janka 2012). NSs can also receive a "Blaauw-kick" (Blaauw 1961) when the progenitor experiences an abrupt mass loss phase, however these kicks are limited by close binary interactions that expel the donor's envelope prior to the SN (Huang 1963, Tutukov & Yungelson 1973, Leonard et al. 1994). Particularly, NS kicks are implied by the high spatial velocity of radio pulsars (Cordes et al. 1993, Hobbs et al. 2005, Lyne & Lorimer 1994, Verbunt et al. 2017) when compared to their progenitors (Gunn & Ostriker 1970).

For this paper we adopt three different NS kick velocity models. Our default model draws arbitrary velocities from the natal NS kick velocity distribution of Verbunt et al. (2017), which was determined from radio pulsar parallaxes and proper motions. The distribution is composed of a combination of two Maxwellians with $\sigma = 75\,\mathrm{km\,s^{-1}}$ and $\sigma = 316\,\mathrm{km\,s^{-1}}$. The bimodal distribution is linked to the reduced NS kick velocity of small iron core NSs and NSs that formed via electron capture SNe a (Podsiadlowski et al. 2004, van den Heuvel 2004, Knigge et al. 2011, Janka 2012, Tauris et al. 2015, Bray & Eldridge 2016). Studies of X-ray binaries found that these NSs can have extremely low NS kick velocities (Pfahl et al. 2002, van den Heuvel 2004, Linden et al. 2009, Antoniou et al. 2010, Antoniou & Zezas 2016) that are of the order of a few $\mathrm{km\,s^{-1}}$. To account for such low velocities we construct a second model by reducing the velocities drawn from the Verbunt et al. (2017) distribution by a factor of 10. For the third model we consider the distribution of Hobbs et al. (2005) which is a single Maxwellian with a one-dimensional (1D) root mean square (rms) of $\sigma = 265\,\mathrm{km\,s^{-1}}$ inferred from the proper motion of radio pulsars.

4.2.3 Radio pulsar models

A radio pulsar is modelled as a rotating magnetic dipole in a vacuum, radiating energy through dipole spin-down emission. The energy loss results in the generation of a magnetospheric plasma and consequently the acceleration of charged particles producing radio emission (see Gurevich & Istomin 2007 and references therein). The majority of all known radio pulsars have spin periods (P) less than 10 s, and period derivatives ($\dot{P}$) between 10^{-22} and $10^{-10}\,\mathrm{ss^{-1}}$ (see Figure 1.4). The $\dot{P}$ of the NS is dependent on its surface magnetic field (B), moment of inertia (I), radius (R), and P:

$$\dot{P} = \frac{8\pi^2 R^6}{3c^3 I}\frac{B^2}{P}, \tag{4.3}$$

where c is the speed of light. As such we define a simulated radio pulsar as a NS within the $P-\dot{P}$ parameter space of the observed pulsar population.

Radio Emission Mechanism

The acceleration of electron-positron pairs is crucial for the generation of radio pulsar emission. The radiation terminates when the pulsar's rotating magnetosphere no longer generates the potential difference required for pair production (Sturrock 1971, Chen & Ruderman 1993). When the emission terminates the radio pulsar becomes radio quiet. This corresponds to a death line on the $P-\dot{P}$ diagram beyond which the pulsar mechanism switches off, and consequently the pulsar is no longer observed. Bhattacharya et al. (1992) calculated a theoretical death line of the form

$$\frac{B}{P^2} = 0.17 \times 10^{12}\ \mathrm{G\,s^{-1}}, \tag{4.4}$$

where B is the NS's surface magnetic field, and P the NS's spin period. This relation is well supported by the distribution of known pulsars on the $P-\dot{P}$ diagram (Faucher-Giguère & Kaspi 2006). For our synthetic pulsars we use Equation 4.4 to distinguish between active and radio quiet pulsars.

Observational Effects

The most important observational effects that can hinder the detection of a radio pulsar in the SMC are the pulsar's beaming fraction and brightness. Previous work (Lyne et al. 1975, Vivekanand & Narayan 1981, Proszynski & Przybycien 1984) found that the radio luminosity for Galactic pulsars has a power law dependence on P and $\dot{P}$. Considering a power law of the form

$$\log(L) = \log\left(L_0 P^{\epsilon_P} \dot{P}_{15}^{\epsilon_{\dot{P}}}\right) + L_{\mathrm{corr}}, \tag{4.5}$$

where $L_0 = 0.18\ \mathrm{mJy\,kpc^2}$. The units of P is seconds, while $\dot{P}$ has units of $10^{-15}\ \mathrm{ss^{-1}}$. The two exponents relating to P and $\dot{P}$ are determined empirically, with values of $\epsilon_P = -1.5$ and $\epsilon_{\dot{P}} = 0.5$ (Lorimer et al. 1993, Faucher-Giguère & Kaspi 2006, Bates et al. 2014). The radio luminosity of a pulsar may be affected by physical variations in the modelled luminosity, distance uncertainties, as well as viewing geometries. To account for these variations the dithering term, L_{corr} is added. L_{corr} is modelled by a normal distribution, centred at zero, with $\sigma_{L_{\mathrm{corr}}} = 0.8$ (Lorimer et al. 1993) determined empirically. Once L is calculated the flux density (S) for each pulsar is given by dividing L with d^2, where $d = 60\,\mathrm{kpc}$ is the average distance to the SMC. This conversion from luminosity does not account for any beaming or geometrical effects, and is commonly referred to as the "pseudo-luminosity" (Arzoumanian et al. 2002, Lorimer et al. 2006).

Following the flux calculation of every pulsar, we determine the beaming fraction of pulsars in a particular spin period bin. Tauris & Manchester (1998) defined an empirical relationship between a pulsar's spin period and the beaming fraction for pulsars where $P > 0.1$ s:

$$f_{\mathrm{TM}}(P) = 0.09\left[\log\left(\frac{P}{s}\right) - 1\right]^2 + 0.03. \tag{4.6}$$

Since a small portion of our simulated pulsars have $P \leq 0.1$ s we depict the beaming fraction for pulsars in this regime by a linear relationship. The relationship is defined by a beaming fraction of 0.9 to 0.39 for $0.001 \leq P(\mathrm{s}) \leq 0.1$. The lower limit was chosen from $f_{TM}(0.1) = 0.39$, while the upper limit of 0.9 was determined from millisecond pulsars by Kramer et al. (1998). From these limits we extend the Tauris & Manchester (1998) beaming fraction linearly with

$$f_{\mathrm{TMe}}(P) = -0.255\ \log\left(\frac{P}{s}\right) + 0.135, \tag{4.7}$$

where $0.001 \leq P(\mathrm{s}) \leq 0.1$. Finally, the total number of pulsars in a period bin is given by multiplying the number of pulsars with the beaming fraction. Furthermore, to test how sensitive the number of detected pulsars is to the default empirical radio luminosity (Equation 4.5, $\sigma_{L_{\mathrm{corr}}} = 0.8$) and the beaming fraction model (Equation 4.6 & 4.7), we consider a second model in each case. For the radio luminosity the second model is defined by adapting $\sigma_{L_{\mathrm{corr}}}$ from 0.8 to 2, simply to test how sensitive the number of detected pulsars is to $\sigma_{L_{\mathrm{corr}}}$. The second empirical beaming fraction model was derived by Lyne & Manchester (1988):

$$f_{\mathrm{LM}}(P) = \frac{4}{\pi}\sin\left(6.5^{\circ} P^{-1/3}\right), \tag{4.8}$$

and is valid for spin periods down to 0.005 s. For pulsars with $P < 0.005$ s we set $f_{\mathrm{LM}}(0.005) = 0.78$.

4.2.4 Star formation model

To account for the star formation history (SFH) of the SMC, we normalise our simulation with respect to the simulated mass and the mass available for each SFE (M_{SFE}). The mass available for star formation (SF) is calculated for two star formation histories (SFHs) determined by Harris & Zaritsky (2004) and Antoniou et al. (2010). Harris & Zaritsky (2004) composed a global averaged photometric SFH (HZ04) of the SMC using the Magellanic Clouds Photometric Survey (MCPS, Zaritsky et al. 2002, 2004). From Figure 7 in Harris & Zaritsky (2004) we deduced a star formation rate (SFR) of $0.28\,\mathrm{M}_{\odot}\,\mathrm{yr}^{-1}$ that lasted for 31 Myr for the most recent

SFE that occurred 60 Myr ago. The star formation was averaged across time and spatial bins for the entire SMC. The SFEs for the last 100 Myr were not resolved, implying that there could be unresolved, intense star formation bursts. Harris & Zaritsky (2004) also calculated the metallicity evolution with every SFE, and found that the 60 Myr SFE has a metallicity of $Z = 0.008$. This is a factor of two larger than is usually assumed. Later on Antoniou et al. (2010) derived the SFH (A10) of regions in the SMC containing X-ray binaries from the spatially resolved HZ04 SFH. The A10 SFH resolved the SFH of the last 100 Myr into four star formation bursts (see Table 1 in Antoniou et al. 2010), and were quoted in $M_\odot\,yr^{-1}\,arcmin^{-2}$. While we realize this SFH is specific to the regions harbouring HMXBs, we invoked this SFH for the entire SMC ($6.7\,deg^2$), to observe the effects of a globally higher star formation rate. As in the previous study they found evidence for a SFE, 67 Myr ago, but with an average SFR of $0.72\,M_\odot\,yr^{-1}$, followed by a SFE 42 Myr ago with a SFR $1.72\,M_\odot\,yr^{-1}$. They concluded that the most recent SFEs occured 17 Myr and 11 Myr ago with SFRs of $0.38\,M_\odot\,yr^{-1}$ and $0.85\,M_\odot\,yr^{-1}$ respectively. The mass available for star formation for a given SFH is calculated by multiplying the duration (Δt) of the SFEs with the corresponding SFRs (Table 4.2).

The normalisation also depends on the simulated mass of the primordial binaries ($M_{\rm total}$):

$$M_{\rm total} = \overbrace{\left[\frac{N_{\rm b}}{f_{\rm param}} \times M_b\right]}^{\text{Binaries}} + \overbrace{\left[\frac{N_{\rm b}}{f_{\rm param}} \times \left(\frac{1 - f_{\rm bin}}{f_{\rm bin}}\right) \times M_{\rm p}\right]}^{\text{Single stars}}, \tag{4.9}$$

where $N_{\rm b}$ is the 3 million simulated binaries, while $M_b = 0.74\,M_\odot$ and $M_{\rm p} = 0.49\,M_\odot$ represent the average, simulated binary and primary mass respectively, and $f_{\rm bin}$ refers to the binary fraction. The total simulation mass also accounts for the fraction of the total SMC stellar population we simulated ($f_{\rm param}$) by assuming the population consists of stars in a mass range from $0.1 - 100\,M_\odot$. Since the primaries consist of stars with masses between 4.4 and $40\,M_\odot$, only 0.74% of the SMC's stellar population was simulated, i.e $f_{\rm param} = 0.0074$. The total simulated mass depends critically on the binary fraction. As we assume a 100% binary fraction the *single star* term in Equation 4.9 becomes zero. The scaling factor c is given by:

$$c = \frac{M_{\rm SFE}}{M_{\rm total}}. \tag{4.10}$$

The total number of simulated pulsars normalised with respect to the mass available for star formation is determined by multiplying c with the number of simulated pulsars. Table 4.2 lists the SFH parameters calculated by HZ04 and A10, as well as c for every SFE. For the default model we adopt the A10 SFH.

Table 4.2: SFH parameters of the SMC as reported by Harris & Zaritsky (2004) and Antoniou et al. (2010), as well as the calculated SFE mass scaling factor c.

SF[a] Peak (Myr)	SFE[b] (Myr)	SFR ($M_\odot$ yr^{-1})	Δt [c] (Myr)	M_{SFR} ($M_\odot$)	c (Number)
Harris & Zaritsky (2004)					
60	53 – 84	0.28	31	8.7×10^6	0.029
Antoniou et al. (2010)					
11	7 – 15	0.85	8	6.8×10^6	0.023
17	9.5 – 24.5	0.38	15	5.7×10^6	0.019
42	25 – 59	1.72	34	58.5×10^6	0.196
68	41 – 95	0.72	54	38.9×10^6	0.130

[a] SF: Star formation.
[b] SFE: The onset and termination of each SFE.
[c] Δt: SFE duration.

4.2.5 Survey detection limits

Besides the total number of pulsars currently present in the SMC, we also determine the number of synthetic pulsars that can be detected by past and future SMC surveys. We model the specific selection effects of the Manchester et al. (2006), and a future SMC MeerKAT survey. The sensitivity of a survey depends on the instrument used, as well as the observational setup. The Manchester survey was conducted with the 21 cm multi-beam receiver (Staveley-Smith et al. 1996b) on the Parkes radio telescope. The gain for the centre beam is 0.69 K Jy^{-1}, and system temperature is 24 K. A potential MeerKAT survey configuration combines 40 dishes in the core of the array, resulting in a gain of 1.6 K Jy^{-1} and system temperature of 17 K. The proposed SMC MeerKAT survey is assumed to observe an area equivalent to the Manchester survey. Prior to the Manchester survey, Crawford et al. (2001) carried out an equally sensitive survey. However, the Manchester survey was more complete, since it covered a larger region of the SMC, and the pulsar searches were conducted across a larger dispersion measure range. For these reasons we will discuss the simulation results with respect to the Manchester survey, and not the Crawford survey. Table 4.3 lists the observational parameters that were used to generate the survey sensitivity curves. The sensitivity limits set the threshold for the number of pulsars that are detected by a particular survey, and are taken at the centre of each spin period bin.

Table 4.3: Observational setup of SMC radio pulsar surveys, as well as the limiting flux densities at 1400 MHz for $P \geq 50$ ms.

Survey	$T_{\rm int}{}^{a}$ (s)	$t_{\rm samp}{}^{b}$ (μs)	$\Delta\nu^{c}$ (MHz)	$N_{\Delta\nu}{}^{d}$ (Number)	S_{1400} (mJy)
Crawford et al. (2001)	8 400	250	288	96	0.066
Manchester et al. (2006)	8 400	1 000	288	96	0.067
MeerKAT	7 200	64	800	4096	0.012

${}^{a}T_{int}$: Observation integration time.
${}^{b}t_{samp}$: Observation sampling time.
${}^{c}\Delta\nu$: Number of frequency channels.
${}^{d}N_{\Delta\nu}$: Number of frequency channels.

4.3 Results

4.3.1 Default model

When assuming the default model (see Section 4.2.1) the SMC is predicted to have formed 1.5×10^4 observable* radio pulsars, and 1.8×10^5 pulsars in total. Of these pulsars we predict that the Manchester survey would detect 4.8 synthesised pulsars, while the future MeerKAT survey is predicted to detect 19.6 pulsars. Figure 4.1 and 4.2 compares the brightness and period distributions of pulsars in binaries, as well as isolated pulsars. These figures illustrate the low radio flux of most synthesised pulsars, rendering them undetectable by the previous survey limits, as well as the MeerKAT survey. However, the spin period distribution of pulsars peaks at ~1s. So, it is the combined impact of the prevalence of pulsars around the 1s spin period together with the increased brightness of the faster spinning pulsars (i.e. > 0.1s) that explains the observed period and luminosity distribution of the pulsars detected by the Manchester survey. (See Section 4.4.1 for further detail.)

4.3.2 Sensitivity to initial conditions

We carried out 96 simulations for two SFH to determine the effect the various parameters have on the total number of synthetic pulsars, as well as the number of pulsars recovered by the Manchester and MeerKAT surveys. The assumed SFH and radio luminosity model are the main parameters that have a significant effect on the synthesised radio pulsar population of the SMC.

The models where the A10 SFH was assumed with the empirical luminosity model ($\sigma_{\rm Lcorr} = 0.8$), while varying the CE model, CE parameter, metallicity, and beaming fraction resulted in a

---

*Pulsars beaming towards us.

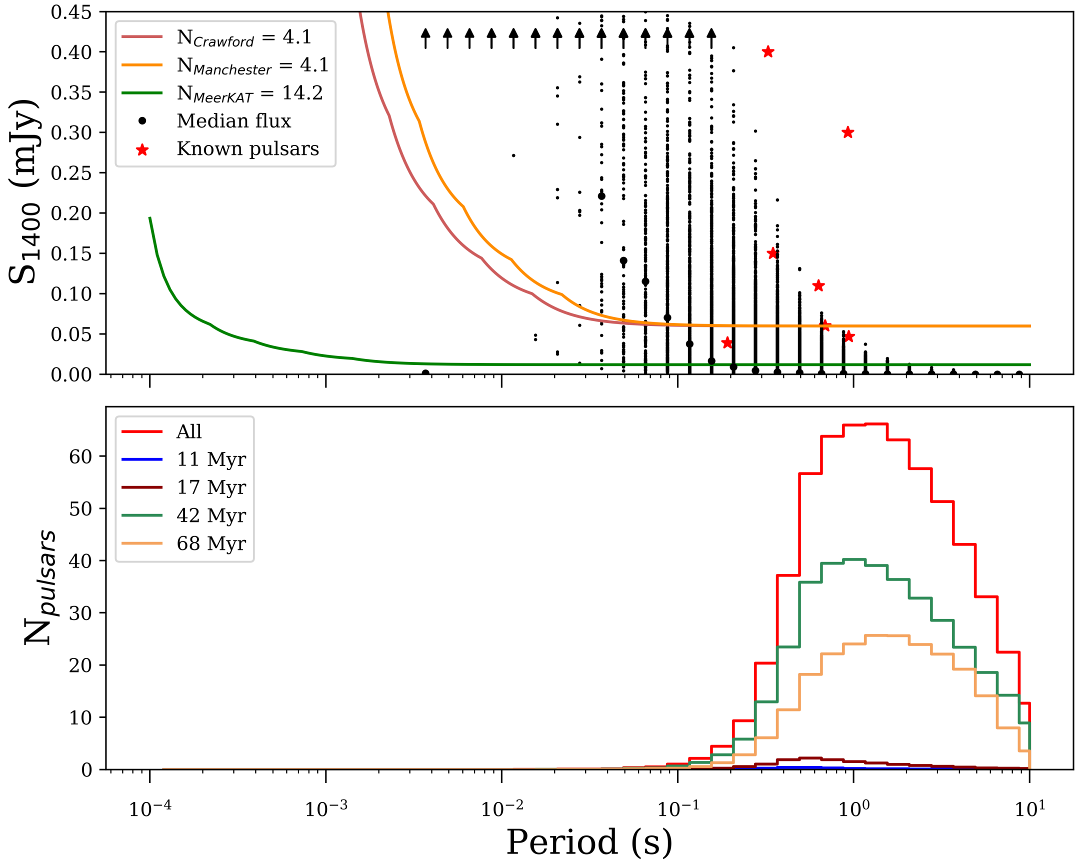

Figure 4.1: Default model of pulsars in binaries, adopting the Tauris & Manchester (1998) beaming fraction and, $\sigma_{L_{corr}} = 0.8$ luminosity model. The top panel exhibits the various survey sensitivity curves with the corresponding number of detected synthetic pulsars in the legend, as well as the brightness distribution of the pulsars. The small black points represent the brightness of individual pulsars, while the large black dots show the median flux of pulsars in a period bin. The black arrows indicate points that are off the plot. The red stars denote the known pulsar population. The bottom panel shows the period distribution of all pulsars in binaries in the SMC that formed during the respective SFEs.

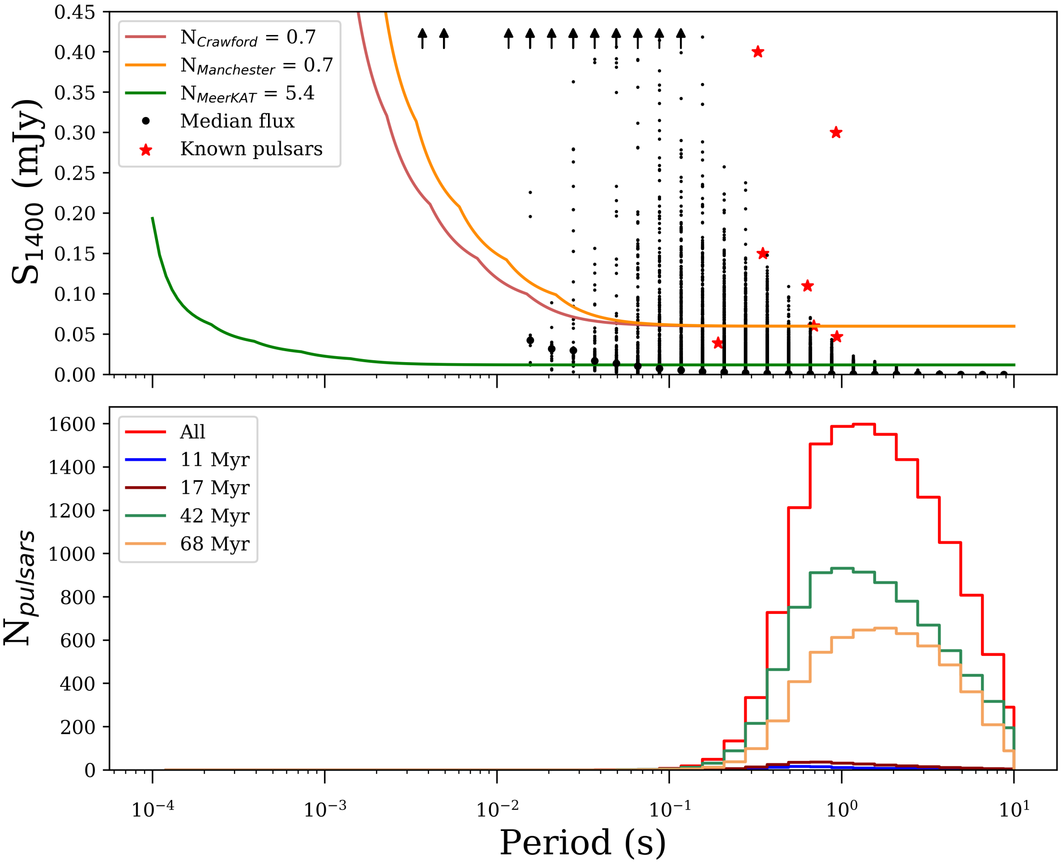

Figure 4.2: Default model of isolated pulsars, adopting the Tauris & Manchester (1998) beaming fraction and, $\sigma_{L_{corr}} = 0.8$ luminosity model. The top panel exhibits the various survey sensitivity curves with the corresponding number of detected synthetic pulsars in the legend, as well as the brightness distribution of the pulsars. The small black points represent the brightness of individual pulsars, while the large black dots show the median flux of pulsars in a period bin. The black arrows indicate points that are off the plot. The red stars denote the known pulsar population. The bottom panel shows the period distribution of all isolated pulsars in the SMC that formed during the respective SFEs.

range of synthesised pulsars (see Appendix 4.6.1). A minimum of 1.2×10^4 and a maximum of 2.2×10^4 pulsars are synthesised. Of these synthesised pulsars, the Manchester survey is predicted to detect 2.8 – 6.0 pulsars, while the future MeerKAT survey is predicted to detect 12.3 – 23.0 pulsars.

Star formation history

The number of synthesised and detected pulsars is exceptionally sensitive to the assumed SFH. The default A10 SFH produces ~12 times more pulsars when compared to the HZ04 SFH. This is directly related to the mass available for star formation. The A10 SFH provides 110×10^6 $M_\odot$ for SF, while the HZ04 SFH results in 8.7×10^6 $M_\odot$. Consequently, the A10 SFH has 12.6 times more mass available for star formation than the HZ04 SFH, and in turn ~12 times more pulsars are synthesised. The assumed SFH also has consequences for the number of recovered pulsars. The A10 SFH results in the recovery of 14.5 and 59.4 times more synthesised pulsars for the Manchester and MeerKAT survey when compared to the HZ04 SFH. The HZ04 SFH yields an insignificant population of pulsars ($\sim1\times10^3$), thus we will only report the results of the A10 SFH. The results of the 96 simulations for the A10 SFH is summarised in Appendix 4.6.1.

Radio luminosity model

The number of recovered pulsars is contingent on the assumed radio luminosity model. The alternate luminosity model ($\sigma_{L_{corr}} = 2.0$) allows for brighter synthesised pulsars when compared to the empirical, default model ($\sigma_{L_{\mathrm{corr}}} = 0.8$). Consequently, more pulsars are recovered when the survey selection effects are applied with the alternate luminosity model. In particular the alternate radio luminosity model results in the detection of 16.0 synthesised pulsars with the Manchester survey, while the MeerKAT survey is predicted to detect 112.6 pulsars. This corresponds to an increase by a factor of 3.3 and 5.7 for the Manchester and MeerKAT surveys respectively, when adopting the alternate luminosity model instead of the empirical, default model's radio luminosity.

4.3.3 Consistent population properties

The simulations are extremely robust in terms of the CE model ($\gamma\alpha$ vs $\alpha\alpha$), CE parameter, metallicity, and beaming fraction, i.e across all these models there are no categorical differences in the total number of synthesised or recovered pulsars. However, the applied SFH and radio luminosity model have a significant impact on both the number of synthesised and recovered pulsars. As such, we group the results by the A10 SFH as well as the empirical radio luminosity model ($\sigma_{L_{\mathrm{corr}}} = 0.8$), and determine the various medians with corresponding standard deviations as error estimates.

On average the SMC synthesised $(1.6 \pm 0.3) \times 10^4$ detectable radio pulsars in the last ~100 Myr. This population excludes old, recycled MSPs, and only includes pulsars beaming towards us. By applying the Manchester survey detection limits we recover 4.0 ± 0.8 synthetic pulsars on average, while the SMC MeerKAT survey is predicted to detect 17.2 ± 2.5 pulsars.

4.3.4 Pulsars in binaries

The NS kick velocity distribution does not have a significant impact on the number of synthesised or recovered pulsars. However, it predicts different fractions of synthesised pulsars in binaries. When applying NS kick velocity distributions from Hobbs et al. (2005) and Verbunt et al. (2017) an average of 2.4% and 5.5% of the pulsar population is predicted to occur in binaries, respectively. Conversely, when adopting the alternative model where we reduced the kick velocities from Verbunt et al. (2017) by a factor of 10 an average of 19% of the synthesised pulsar population is retained within a binary. The pulsars in binaries with high mass companions ($M > 5\,M_\odot$) are primordial high mass X-ray binaries (HMXBs). When considering the default model 4% of pulsars are predicted to be in binaries, implying ~160 synthesised pulsars are in binaries with high mass companions with orbital periods ($P_{\rm orb}$) below 1000 days. Alternatively when applying the Hobbs et al. (2005) distribution, the pulsar binary fraction is 2% predicting ~60 high mass binary pulsars.

Although a relatively small number of synthesised pulsars occur in binaries, the simulations predict that ~80% of the synthesised pulsars that are detected by the Manchester survey are in binaries. This prediction is inherent to the synthesised population of bright binaries with spin periods below 0.1 s (Figure 4.1). These pulsars are young and typically short-lived, before the pulsar mechanism is quenched by binary interactions. Pulsars within very compact binaries, and/or with massive companions are quenched shortly after formation when mass transfer ensues. These pulsars have less time to spin down, and consequently are brighter on average than the isolated pulsars with spin periods below 0.1 s.

The orbital period ($P_{\rm orb}$) and eccentricity (e) of the pulsars in binaries have a weak positive correlation (Figure 4.3). The binaries shown in the figure include 95% of the simulated binary population ($P_{\rm orb} \leq 5\,000$ days). The orbital period distribution has five peaks, the peaks below $P_{\rm orb} \sim 300$ days are associated with the SFEs of 11 & 17 Myr ago, while the remaining two peaks ($P_{\rm orb} \sim 400$ & 1200 days) present the evolved binaries from the SFEs that occurred 42 & 68 Myr ago. The evolved binary pulsars occur in wider binaries where minimal mass transfer occurs, extending the life time of the radio pulsars. There is a large number of binaries with a nearly circular orbit, after which the eccentricity distribution follows a Poisson-like distribution.

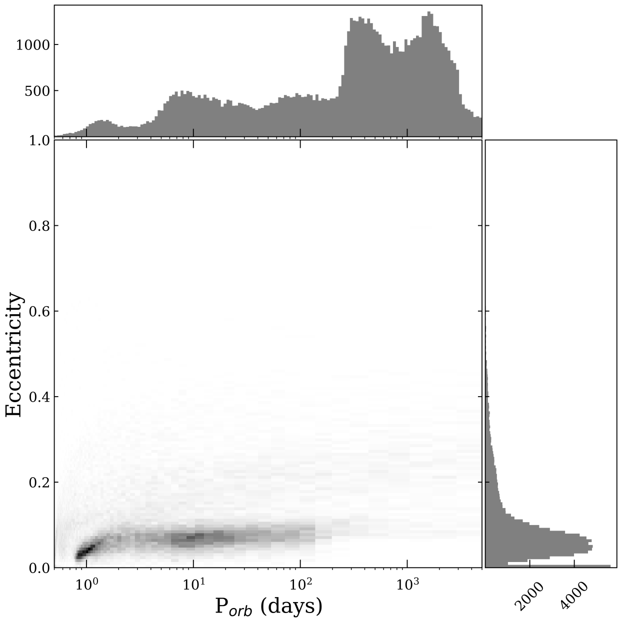

Figure 4.3: Intensity plot showing the relationship between the orbital period ($P_{\rm orb}$) and eccentricity of simulated pulsars in binaries. The individual orbital period and eccentricity distributions are also depicted on the relevant axes.

The peak at $e \sim 0$ is associated with more evolved binaries from the 42 and 68 Myr SFEs. The most recent SFEs (11 & 17 Myr ago) have exponential eccentricity distributions with ~18% of their population having $e > 0.2$, while the older SFEs (42 & 68 Myr ago) have fewer eccentric orbits with only ~7% of systems exceeding an eccentricity of 0.2.

4.4 Discussion

4.4.1 SMC radio pulsar population

In this study we utilise binary population synthesis techniques to estimate the size of the SMC radio pulsar population, and apply various survey selection effects in an attempt to recover the observed population, and characterise the efficiency of the future SMC MeerKAT survey. We predict that $(1.6 \pm 0.3) \times 10^4$ normal radio pulsars were formed in the SMC during the last ~100 Myr. This population excludes recycled, old MSPs, and only includes pulsars beaming towards us. This is in agreement with Ridley & Lorimer (2010), who predict a population of $(1.09 \pm 0.16) \times 10^4$ normal pulsars in the SMC. This agreement is striking, since our method was based on binary evolution and dependent on the SFH of the SMC, while Ridley & Lorimer (2010) utilised a Monte Carlo method (Lorimer et al. 2006) that seeded pulsars until the Manchester selection effects recovered five observed pulsars. Ridley & Lorimer (2010) also predict that 67.2% of all pulsars born in the SMC will escape within the average lifetime of a pulsar, assuming that the SMC pulsars receive similar NS kicks as Galactic NSs (Hobbs et al. 2005, Verbunt et al. 2017). The high fraction of escaped pulsars is related to the relatively small escape velocity of the SMC ($\approx 120\,\mathrm{km\,s^{-1}}$). Although a large fraction of pulsars may escape the SMC, we may still be able to detect a reasonable portion of the 67.2% of escaped pulsars with our surveys if the pulsars are travelling along our line of sight. To quantify this we would need to carry out more detailed simulations. If such a large portion of pulsars are predicted to escape the SMC we would expect more pulsars near the edges of the SMC. Currently this does not seem to be the case (see McConnell et al. 1991, Crawford et al. 2001, Manchester et al. 2006, Titus et al. 2019), however more pulsars need to be discovered to make inferences on the spatial distribution of the SMC pulsars. Furthermore, Ridley & Lorimer (2010) assumes a NS kick velocity distribution derived from Galactic pulsars, which may not be the case for the SMC pulsars, and can also affect the number of escaped pulsars. The discovery of more radio pulsars and their characterisation are necessary to improve the models we base our simulations on.

We study how many pulsars may be observed by the Manchester survey, by applying the survey's specific selection effects and recover 4.0 ± 0.8 synthetic pulsars, which compares well to the five pulsars observed with the Manchester et al. (2006) survey. The proposed SMC MeerKAT survey is ~6 times more sensitive than the Manchester survey, however it is predicted to detect only 17.2 ± 2.5 pulsars. The large distance to the SMC reduces the flux of the radio pulsars to such an extent that MeerKAT will only detect the brightest pulsars. To make a comparison between the observed and synthesised spin period distribution we convolve the simulated flux and spin period distributions (top and bottom panels of Figures 4.1 and 4.2) to create a normalised, bias corrected spin period distribution (Figure 4.4). Currently there are only seven known pulsars in the SMC. Such a small number of pulsars is insufficient to make extensive comparisons, however Figure 4.4 shows that the observed pulsars are coincident with the peaks of the binary and isolated pulsar period distributions. The isolated pulsars have a spin period distribution that peaks around 1 s, and extends to 10 s. The pulsars in binaries account for only a few percent of all the simulated pulsars, and have a spin period distribution peaking at ~0.3 s. Unlike the isolated pulsars, very few pulsars in binaries have spin periods beyond ~1 s. Initially, rapidly spinning pulsars are prevented from accreting material by the propeller mechanism, however once they have spun down sufficiently the NS can accrete material and enter the HMXB phase. The SMC in particular harbours a number of accreting NSs with spin periods shorter than 10 s (see Haberl & Sturm 2016, and references therein). Moreover, the simulations predict a population of ~60 – 160 NSs in binaries with massive companions. These systems are primordial HMXBs, and compare well with the known population of ~140 HMXBs in the SMC.

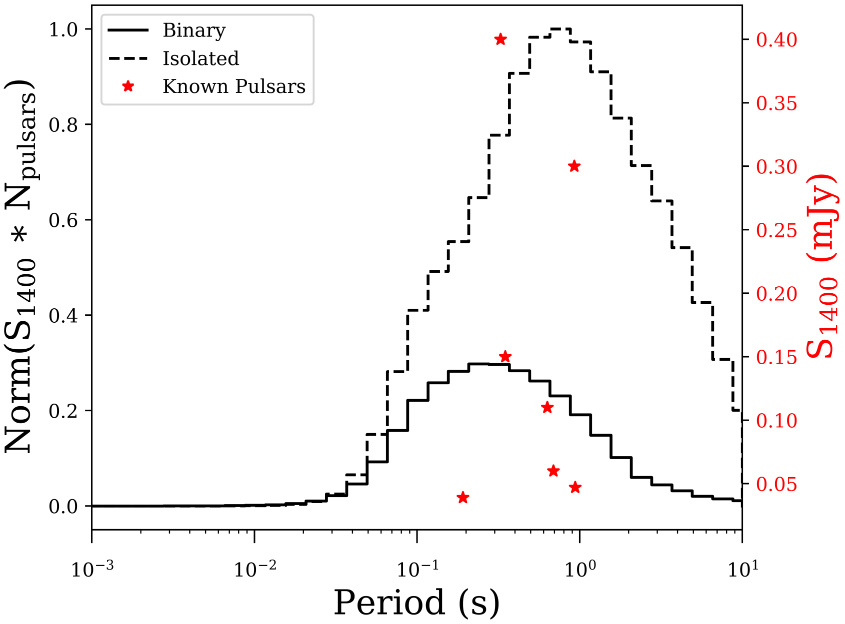

Figure 4.4: The normalised, bias corrected spin period distribution of pulsars in binaries and isolated pulsars. This figure is a result of convolving the flux and period distributions, i.e. the top and bottom panels of Figure 4.1 and 4.2.

Another notable difference is that pulsars in binaries are brighter than isolated pulsars with spin periods below ~0.1 s (see Figure 4.1 & 4.2). As a result the simulations suggest that less sensitive surveys are more likely to detect pulsars in binaries, and that as many as 80% of the Manchester pulsars are predicted to be in binaries. Thus far one of the five pulsars has been identified as a pulsar in a binary with a B star in a 51 day orbit (Kaspi et al. 1994). Due to the distance to the SMC extensive timing studies of the known pulsars have not been possible, thus the possibility that they are in wide orbits cannot be ruled out. With the upcoming MeerKAT survey, timing studies are likely to identify new pulsars in binaries. Especially since the bulk of the synthetic pulsars in binaries have orbital periods below $\sim 10^3$ days with fairly low eccentricities (Figure 4.3) for which realistic observing campaigns can be launched to search for the binaries. Apart from timing studies it is also possible to search for pulsars in binaries with acceleration searches. Ridley et al. (2013) carried out acceleration searches that were sensitive to pulsars in binaries with spin periods greater than 23.5 ms on the archival Manchester et al. (2006) data, but did not discovery any new pulsars in binaries. However, acceleration searches are most effective for close binaries, i.e. those more likely for MSPs, and not wide binaries.

4.4.2 Constraints on assumed models

In the following sections we place constraints on the SMC SFH, and the empirically determined radio luminosity model.

Star formation history

The A10 SFH successfully reproduced the predicted number of normal pulsars in the SMC, as well as the observed pulsar population. This is in contrast with the HZ04 SFH, that neither produces the predicted number of pulsars nor recovers the observed pulsar population. In fact the HZ04 SFH produces a virtually undetectable pulsar population. The HZ04 is a global, spatially resolved, time averaged SFH, and hence does not account for short bursts of SF. It also does not resolve the SFH of the last 100 Myr, which is when the majority of the pulsars would have formed. The HZ04 may be more suitably applied to older stellar populations where a high temporal resolution is not required. For our pulsar population it is essential to apply a SFH that is resolved throughout the last ~100 Myr, making the A10 SFH more appropriate. The A10 SFH is also limited and not ideal, since it was not calculated for the entire SMC, but for regions containing X-ray binaries, which we then assumed for the entire SMC. Regardless of which SFH is more appropriate, the simulations require a SFH that provides sufficient mass to synthesise enough pulsars for the Manchester survey to recover the five observed pulsars. Thus, we require a SFH that provides at least as much mass as the modified A10 SFH (110×10^6 $M_\odot$).

Radio luminosity model

The default model which adopts the empirical radio luminosity model ($\sigma_{L_{\mathrm{corr}}} = 0.8$) produces a sufficient number of pulsars to recover the five observed pulsars with a ~20% error when the Manchester selection effects are applied. Reproducing the observed population with such accuracy provides confidence for the method, its results, and the predicted number of pulsars MeerKAT will detect. The radio luminosity dispersion of the Galactic pulsars is well modelled for $\sigma_{L_{\mathrm{corr}}} = 0.8$. There is no observational evidence that the SMC pulsars will deviate from this relation. Moreover, when adopting the alternate radio luminosity model ($\sigma_{L_{\mathrm{corr}}} = 2$), it does not result in the recovery of the five observed pulsars, instead it overestimates the population by a factor of three. The alternate model is not supported by observations, it was a theoretical test to determine how sensitive the simulations are to the assumed luminosity model. Consequently, there is presently no clear indication that the SMC pulsar radio luminosities differ when compared to the Galactic pulsar population luminosities.

4.5 Conclusion

We modelled the present day radio pulsar population of the SMC (excluding millisecond pulsars). On average the number of synthesised and recovered pulsars were not affected by metallicity, CE evolution, NS kick velocity distribution or the beaming fraction model, but are strongly dependent on the recent star formation rate and the pulsar luminosity model. The simulations predict a population of $(1.6 \pm 0.3) \times 10^4$ normal radio pulsars. When applying the selection effects of the Manchester et al. (2006) survey we recover 4.0 ± 0.8 synthetic pulsars, which is in agreement with the five observed pulsars. Furthermore, the future SMC MeerKAT survey is predicted to detect 17.2 ± 2.5 pulsars. This implies that the proposed SMC MeerKAT survey will not be sensitive enough to detect a significant portion of the SMC pulsar population. That being said, MeerKAT will provide a valuable test to the predicted number of detectable pulsars, and contribute to our understanding of massive binary evolution.

Acknowledgements

NT, VMcB, and DAHB acknowledges support of the National Research Foundation of South Africa (grants 98969, 93405, and 96094). ST acknowledges support from the Netherlands Research Council NWO (grant VENI [nr. 639.041.645]). BWS acknowledge funding from the European Research Council (ERC) under the European Union's Horizon 2020 research and innovation programme (grant agreement No. 694745).

4.6 Appendix

4.6.1 Simulation tables

Here follows the results of all the simulations where the Antoniou et al. (2010) SFH was assumed.

Table 4.4: Simulation results for the Tauris & Manchester (1998) beaming fraction, and $\sigma_{\mathrm{Lcorr}} = 0.8$ radio luminosity model.

Model	Total Pulsars		Detached		Disrupted		Crawford et al. (2001)		Manchester et al. (2006)		MeerKAT	
CE	$\gamma\alpha$	$\alpha\alpha$	$\gamma\alpha$	$\alpha\alpha$	$\gamma\alpha$	$\alpha\alpha$	$\gamma\alpha$	$\alpha\alpha$	$\gamma\alpha$	$\alpha\alpha$	$\gamma\alpha$	$\alpha\alpha$
V4CE2	14889	14866	5	5	95	95	4.08	4.00	4.05	3.96	17.30	17.26
H4CE2	15234	15082	2	2	98	98	3.54	3.58	3.49	3.57	16.57	16.36
V4CE25	14717	14053	4	4	96	96	4.83	4.57	4.80	4.53	19.61	18.81
H4CE25	15005	14227	2	2	98	98	4.72	4.32	4.69	4.28	18.93	18.11
0.1V4CE2	13707	13395	22	22	78	78	5.33	5.21	5.28	5.19	21.18	19.66
0.1V4CE25	13374	12439	19	17	81	83	5.78	5.20	5.73	5.16	22.84	20.73
V8CE2	15071	14693	5	5	95	95	4.32	3.97	4.28	3.95	18.48	17.58
H8CE2	15247	14893	2	2	98	98	3.81	3.54	3.78	3.50	17.35	16.92
V8CE25	14468	13747	4	4	96	96	4.09	3.66	4.06	3.63	16.22	15.00
H8CE25	14691	13933	2	2	98	98	3.74	3.38	3.72	3.35	15.76	13.93
0.1V8CE2	12957	13303	20	23	80	77	5.29	5.69	5.26	5.66	19.74	22.06
0.1V8CE25	13484	12092	23	17	77	83	6.01	4.48	5.97	4.44	23.04	17.11

Table 4.5: Simulation results for the Tauris & Manchester (1998) beaming fraction, and $\sigma_{\mathrm{Lcorr}} = 2.0$ radio luminosity model.

Model	Total Pulsars		Detached		Disrupted		Crawford et al. (2001)		Manchester et al. (2006)		MeerKAT	
CE	$\gamma\alpha$	$\alpha\alpha$	$\gamma\alpha$	$\alpha\alpha$	$\gamma\alpha$	$\alpha\alpha$	$\gamma\alpha$	$\alpha\alpha$	$\gamma\alpha$	$\alpha\alpha$	$\gamma\alpha$	$\alpha\alpha$
V4CE2	14889	14866	5	5	95	95	14.25	14.23	14.16	14.12	111.11	111.36
H4CE2	15234	15082	2	2	98	98	13.52	13.42	13.40	13.27	111.49	110.33
V4CE25	14717	14053	4	4	96	96	16.10	15.34	15.95	15.23	112.64	111.23
H4CE25	15005	14227	2	2	98	98	15.61	14.64	15.51	14.54	110.86	109.06
0.1V4CE2	13707	13395	22	22	78	78	17.68	16.62	17.56	16.51	112.86	107.74
0.1V4CE25	13374	12439	19	17	81	83	19.00	16.93	18.88	16.81	114.79	111.07
V8CE2	15071	14693	5	5	95	95	15.28	14.40	15.17	14.30	109.72	107.25
H8CE2	15247	14893	2	2	98	98	14.32	13.86	14.22	13.73	106.81	104.70
V8CE25	14468	13747	4	4	96	96	13.47	12.18	13.34	12.09	100.64	97.30
H8CE25	14691	13933	2	2	98	98	12.87	11.38	12.77	11.29	100.17	94.39
0.1V8CE2	12957	13303	20	23	80	77	16.65	18.64	16.54	18.54	104.04	106.21
0.1V8CE25	13484	12092	23	17	77	83	19.45	14.21	19.35	14.13	109.88	97.01

Table 4.6: Simulation results for the Lyne & Manchester (1988) beaming fraction, and $\sigma_{\mathrm{Lcorr}} = 0.8$ radio luminosity model.

Model	Total Pulsars		Detached		Disrupted		Crawford et al. (2001)		Manchester et al. (2006)		MeerKAT	
CE	$\gamma\alpha$	$\alpha\alpha$	$\gamma\alpha$	$\alpha\alpha$	$\gamma\alpha$	$\alpha\alpha$	$\gamma\alpha$	$\alpha\alpha$	$\gamma\alpha$	$\alpha\alpha$	$\gamma\alpha$	$\alpha\alpha$
V4CE2	21365	21323	5	5	95	95	3.44	3.38	3.41	3.35	15.33	15.29
H4CE2	21861	21635	2	2	98	98	2.99	3.02	2.95	3.01	14.70	14.51
V4CE25	21116	20159	4	4	96	96	4.08	3.86	4.05	3.83	17.29	16.55
H4CE25	21538	20422	2	2	98	98	3.98	3.64	3.96	3.62	16.67	15.92
0.1V4CE2	19671	19219	22	22	78	78	4.52	4.42	4.48	4.40	18.82	17.45
0.1V4CE25	19155	17802	19	16	81	84	4.88	4.39	4.84	4.36	20.15	18.23
V8CE2	21676	21122	5	5	95	95	3.64	3.34	3.61	3.33	16.40	15.62
H8CE2	21939	21422	2	2	98	98	3.21	3.00	3.18	2.96	15.39	15.04
V8CE25	20800	19777	4	4	96	96	3.46	3.10	3.44	3.08	14.34	13.24
H8CE25	21137	20052	2	2	98	98	3.16	2.86	3.14	2.84	13.92	12.30
0.1V8CE2	18596	19121	19	23	81	77	4.48	4.82	4.45	4.79	17.46	19.60
0.1V8CE25	19395	17362	23	17	77	83	5.10	3.81	5.07	3.77	20.51	15.11

Table 4.7: Simulation results for the Lyne & Manchester (1988) beaming fraction, and $\sigma_{\mathrm{Lcorr}} = 2.0$ radio luminosity model.

Model	Total Pulsars		Detached		Disrupted		Crawford et al. (2001)		Manchester et al. (2006)		MeerKAT	
CE	$\gamma\alpha$	$\alpha\alpha$	$\gamma\alpha$	$\alpha\alpha$	$\gamma\alpha$	$\alpha\alpha$	$\gamma\alpha$	$\alpha\alpha$	$\gamma\alpha$	$\alpha\alpha$	$\gamma\alpha$	$\alpha\alpha$
V4CE2	21365	21323	5	5	95	95	12.63	12.61	12.55	12.52	97.34	97.51
H4CE2	21861	21635	2	2	98	98	12.00	11.90	11.90	11.77	97.63	96.63
V4CE25	21116	20159	4	4	96	96	14.15	13.46	14.03	13.37	98.66	97.81
H4CE25	21538	20422	2	2	98	98	13.71	12.86	13.62	12.77	97.03	95.74
0.1V4CE2	19671	19219	22	22	78	78	15.72	14.74	15.63	14.65	99.39	94.86
0.1V4CE25	19155	17802	19	16	81	84	16.72	14.86	16.61	14.76	100.99	97.98
V8CE2	21676	21122	5	5	95	95	13.55	12.78	13.46	12.70	96.36	94.19
H8CE2	21939	21422	2	2	98	98	12.69	12.30	12.61	12.20	93.82	91.93
V8CE25	20800	19777	4	4	96	96	11.91	10.75	11.80	10.67	88.25	85.43
H8CE25	21137	20052	2	2	98	98	11.36	10.04	11.28	9.97	87.71	82.85
0.1V8CE2	18596	19121	19	23	81	77	14.71	16.56	14.62	16.47	91.59	93.80
0.1V8CE25	19395	17362	23	17	77	83	17.29	12.56	17.21	12.49	97.13	85.52

Chapter 5

Conclusion and future work

In this thesis I explored various evolutionary stages of massive binaries in the MCs through observational and theoretical studies. I investigate the evolutionary channels relating to NSs in particular, and compare the HMXB and radio pulsar populations of the LMC and SMC.

5.1 High mass X-ray binaries

In Chapter 2, I carried out an optical follow up study of BeXB candidates identified by the XMM-Newton X-ray survey of the LMC, and identified nine new BeXBs. This increased the confirmed population of known BeXBs in the LMC to 26. I also explored the optical characteristics of these new BeXBs to determine the spectral class of the companions, as well as identify any orbital periods with a timing study. The detailed spectral study showed that all the companions have spectral types of B3 or earlier, while the timing study revealed orbital periods ranging from ~5 – 600 days. Both the SMC and LMC have now been surveyed to a limiting point source sensitivity of $\sim 10^{33}$ erg s^{-1} in the X-rays with complementary optical timing and spectral studies, characterising the optical companions, as well as the orbital periods of the binaries. The uniform X-ray surveys reduce the observational selection effects and biases, and allow for a meaningful comparison of the HMXB populations of the LMC and SMC.

The SMC harbours ~140 HMXBs (candidate and confirmed, Antoniou et al. 2019), while the more massive LMC contains 33 confirmed[†], and eight candidate HMXBs - a total of 41 HMXBs. The fraction of HMXBs to stellar mass in the SMC (10^{-7} M$_{\odot}^{-1}$) is an order of magnitude higher than the LMC (10^{-8} M$_{\odot}^{-1}$), indicating the high efficiency with which the SMC has been forming HMXBs when compared to the LMC. Previous work (Grimm et al. 2003, Shtykovskiy & Gilfanov 2005, Antoniou et al. 2018) has shown the discrepancy in population

---

[†] Latest HMXB discovered by Maitra et al. (2019).

size is likely related to the SFHs of the MCs, which highlights the duration of a particular SFE, as well as the respective star formation rates that determine the mass available for star formation.

The Be phenomenon may be in part a result of massive binary evolution, one scenario in particular suggests that OB stars evolve to OBe stars as a result of mass transfer, during which they get spun up, and form an outflowing circumstellar disc. Optical photometric studies show that the circumstellar discs of OBe stars take ~25 - 80 Myr to form (McSwain & Gies 2005), they also found that they are more likely to form in close binaries as a result of mass transfer. This implies that a SFE that occurred between 25 - 80 Myr ago will maximise the observed BeXB population. The SMC's SFH (Harris & Zaritsky 2004, Antoniou et al. 2010) suggests that a SFE occurred ~60 Myr ago, coinciding with the formation time of circumstellar discs of OBe stars, enabling the formation of BeXBs. Two recent SFEs occurred in the LMC, ~12 Myr ago and ~100 Myr ago (Harris & Zaritsky 2009, Antoniou & Zezas 2016). The most recent LMC SFE (~12 Myr) would have produced massive binaries, however they are mostly too young to have entered the BeXB phase, while SGXBs can form on such a short time scale. To date only two SGXBs have been confirmed in the LMC, making BeXBs the most prevalent HMXB class in the LMC. Conversely, the massive binaries that were formed during the ~100 Myr SFE would have evolved past both the BeXB and SGXB phase. None of the LMC SFEs take place at the time scales required for the formation of circumstellar discs nor the average lifetime of HMXBs, and thus fewer observable HMXBs are expected in the LMC. Both the relatively small population of HMXB in the LMC, and large population of HMXB in the SMC may be in part due to their independent SFHs, and not necessarily an observational bias.

Environmental effects such as metallicity may also have implications for a galaxy's NS population. The SMC has a low metallicity ($Z = 0.004$) that can enable less massive stars to form NSs, since less mass is lost due to line-driven winds (Poelarends 2007). The SMC has a HMXB population three times larger than the LMC, despite having a lower mass. This can partially be related to metallicity discrepancy between the SMC and LMC. Lower metallicities have also been associated with lower NS kick velocities (Pfahl et al. 2002, van den Heuvel 2004, Linden et al. 2009, Antoniou et al. 2010), leading to fewer disrupted binaries, and consequently more HMXBs form. In Chapter 4 (population studies) we showed that a smaller NS kick reduces the number of disrupted binaries significantly. However, our SMC population studies produced a primordial HMXB population (see Section 4.4.1) that compares well with the observed SMC HMXB population by assuming canonical NS kick velocity distributions (see Hobbs et al. 2005, Verbunt et al. 2017). We also found no significant differences in the number of synthesised NSs for a low metallicity ($Z = 0.004$) when compared to a higher metallicity ($Z = 0.008$) which is similar to the metallicity of the LMC ($Z = 0.01^*$.). Consequently, the effect a galaxy's metallicity has on the number of observed HMXBs is still poorly constrained.

5.2 Radio pulsars

The large population of HMXBs in the SMC implies a large NS population, however this is not reflected by the SMC's radio pulsar population. In Chapter 3 I carried out the deepest, most sensitive pulsar searches for six SNRs (and pulsar wind nebulae) in the SMC with the Parkes radio telescope in an attempt to uncover more radio pulsars, and for better characterisation of the radio pulsar population. The targeted survey revealed two new radio pulsars (PSR J0043−73, PSR J0052−72), increasing the population size to seven. The new pulsars have similar DMs and spin periods when compared to the known population. PSR J0052−72 is currently the fastest spinning pulsar in the SMC. These were the first pulsars discovered in the SMC in more than a decade. Neither of the pulsars were associated with SNRs, they were serendipitous discoveries. None of the known SMC radio pulsars have been associated with either SNRs or pulsar wind nebulae. Some young radio pulsars are very bright (e.g. the Vela and Crab pulsars), but this is not the case for all young pulsars. Camilo (2003) completed a census of SNR-pulsar associations (Kaspi & Helfand 2002, Kaspi et al. 1996, Gorham et al., Lorimer et al. 1998, Manchester et al. 2001) and found that in some cases the pulsars associated with SNRs can be faint. If the pulsars in the SMC SNRs are intrinsically faint we would not be able to detect them with the previous generation radio telescopes at the distance of the SMC. However targeted searches with MeerKAT may be able to detect these elusive radio pulsars. The radio pulsar populations of the SMC and LMC have very similar spin period distributions ranging from ~100 – 1000 ms, with the exceptions being the two LMC pulsars, PSR J0537−6910 and PSR J0540−6919 that have spin periods of 16 and 50 ms respectively. However, comprehensive comparisons of the SMC and LMC radio pulsar populations are not possible, since previous surveys were only sensitive to the brightest MC pulsars, discovering only a few pulsars. If the MCs have a similar luminosity distribution to the Galaxy then surveys have only been sensitive to ~4% of the MC pulsar population (See Figure 1.8).

In Chapter 4, I estimate the SMC radio pulsar population and quantify previous and future survey selection effects by conducting population studies with a binary population synthesis code. This is the first application of binary population studies to radio pulsars, and can provide insights with regards to binary radio pulsars. Our estimate of the SMC radio pulsar population (~15 000 pulsars) agrees with previous estimates utilising an independent Monte-Carlo method (Ridley & Lorimer 2010). In addition to the population size, we studied the number of pulsars

---

[*] $Z_{LMC} = \frac{Z_\odot}{2} = \frac{0.02}{2} = 0.01$ (see Vagnozzi 2017 for $Z_\odot$ measurement)

that may be observed by the Manchester et al. (2006) survey by applying the survey's specific selection effects, and recovered ~5 synthesised radio pulsars. This is in excellent agreement with the five pulsars detected by the Manchester survey. Producing results in agreement with observations provides confidence in this new method of population studies for radio pulsars. Using this method we applied the selection effects of the MeerKAT SMC survey, and estimate that MeerKAT will detect ~20 radio pulsars. This is a surprisingly low number, since the proposed MeerKAT survey is ~6 times more sensitive than the previous Manchester survey. With this increase in sensitivity we predict it will only detect a small portion of the SMC radio pulsar population as a result of the SMC's large distance. Nonetheless, the MeerKAT survey of the SMC will provide an excellent test for the predictions made in Chapter 4, and contribute to our understanding of massive binary evolution. The small population of detected radio pulsars in the SMC is primarily attributed to the large distance to the SMC, and not likely a property of the radio pulsar population.

5.2.1 Future work

The observed NS population of the SMC and LMC seems to be linked to their SFHs, and affect the evolutionary phase or state within which they are observed. X-ray surveys of both the MCs, sensitive enough to detect quiescent HMXBs, imply we have detected representative samples of their respective HMXB populations. For the SMC this is supported from a theoretical point of view by the population studies we conducted in Section 4.4.1. The next step involves similar population studies of the LMC to estimate its radio pulsar population size, as well as the primordial HMXB population size. In addition to the population estimates we will also include simulations to estimate the fraction of radio pulsars that will escape the LMC. The LMC population synthesis study will follow the same method outlined in Chapter 4, while applying the LMC SFH, as well as consider additional metallicities for the `SeBa` simulations. This will provide a second case study for binary population synthesis methods applied to radio pulsars, and predict the number of radio pulsars the LMC MeerKAT survey will detect. The LMC MeerKAT survey will be more sensitive than the SMC MeerKAT survey, since it is 10 kpc closer. As such we expect the LMC MeerKAT survey to be sensitive to a larger portion of its radio pulsar population. If this method produces consistent results comparable to observations it can act as a useful tool to asses the efficiency of future radio pulsar surveys, and consequently determine optimised survey parameters.

Simulating the normal radio pulsar (i.e. non-recycled) population is simpler than simulating the HMXB population. This is because, for the the radio pulsars, no mass transfer is allowed after the SN. Simulating HMXB populations with binary population synthesis codes are complicated by both the eccentric orbits and circumstellar discs of BeXBs, which are currently not accounted for. To extend the population studies of radio pulsars to BeXBs in particular, we will have to adapt the code to account for periodic mass transfer onto a NS in an eccentric orbit, from the circumstellar disc of an OBe companion. Once the code has been adapted we will carry out extended population studies to include both the radio pulsar and HMXB phase. Synthesising the HMXB population will predict X-ray luminosity, orbital period, and eccentricity distributions that can be compared to the known HMXB populations of the MCs (Townsend et al. 2011). Extending the simulations can potentially explain the observed radio pulsar and HMXB populations of the MCs, as well as the environmental impact on the observed populations.

5.3 Concluding statement

The MCs offer a unique environment to study resolved stellar populations and their evolution with unprecedented detail. This in conjunction with the known distance to the MCs, reduces the observational biases and uncertainties making the LMC and SMC excellent test beds for stellar population studies.

Now that both the LMC and SMC HMXB populations have been characterised there is sufficient observational data to compare with detailed population synthesis models. However, the unique mass transfer mechanism of BeXBs introduces complexities to the modelling. Current population synthesis codes like SeBa does not addressed these complexities, and would need to be addressed before the BeXB population can be modelled.

The radio pulsar population of the MCs have not been studied observationally to the same extent as the HMXB population. To date, we have only detected a small portion of the pulsar population. This is due to previous instrumental limitations. With MeerKAT and SKA the situation will be improved, and allow for better characterisation of the radio pulsar population, and consequently an improvement on models of the populations.

Previous and future surveys grant the possibility to understand massive binary evolution from an observational perspective, as well as a premise for testing our models by applying the selection effects of particular surveys. Ultimately, pairing past survey results with simulations can help to establish practical guidelines for future surveys, and provide insights on the expected massive binary population sizes.

Bibliography

Abt H. A., 1983, ARA&A, 21, 343

Alsaberi R. Z. E. et al., 2019, MNRAS, 486, 2507

Antoniou V., Hatzidimitriou D., Zezas A., Reig P., 2009, ApJ, 707, 1080

Antoniou V., Zezas A., 2016, MNRAS, 459, 528

Antoniou V., Zezas A., Drake J. J., Badenes C., Haberl F., Hong J., Plucinsky P. P., the SMC XVP Collaboration Team 2018, arXiv e-prints, p. arXiv:1812.11070

Antoniou V. et al., 2019, ApJ, 887, 20

Antoniou V., Zezas A., Hatzidimitriou D., Kalogera V., 2010, ApJ, 716, L140

Arzoumanian Z., Chernoff D. F., Cordes J. M., 2002, ApJ, 568, 289

Badenes C., Maoz D., Draine B. T., 2010, MNRAS, 407, 1301

Bates S. D., Lorimer D. R., Rane A., Swiggum J., 2014, MNRAS, 439, 2893

Besla G., 2015, arXiv e-prints, p. arXiv:1511.03346

Bhattacharya D., Wijers R. A. M. J., Hartman J. W., Verbunt F., 1992, A&A, 254, 198

Bird A. J., Coe M. J., McBride V. A., Udalski A., 2012, MNRAS, 423, 3663

Blaauw A., 1961, Bull. Astron. Inst. Netherlands, 15, 265

Bray J. C., Eldridge J. J., 2016, MNRAS, 461, 3747

Buckley D. A. H., Swart G. P., Meiring J. G., 2006, Completion and commissioning of the Southern African Large Telescope. p. 62670Z

Burgh E. B., Nordsieck K. H., Kobulnicky H. A., Williams T. B., O'Donoghue D., Smith M. P., Percival J. W., 2003, Prime Focus Imaging Spectrograph for the Southern African Large Telescope: optical design. pp 1463–1471

Camacho J., Torres S., García-Berro E., Zorotovic M., Schreiber M. R., Rebassa-Mansergas A., Nebot Gómez-Morán A., Gänsicke B. T., 2014, A&A, 566, A86

Camilo F., 2003, Deep Searches for Young Pulsars. p. 145

Camilo F., Manchester R. N., Gaensler B. M., Lorimer D. R., 2002, ApJ, 579, L25

Carpano S., Haberl F., Sturm R., 2017, A&A, 602, A81

Casares J., Negueruela I., Ribó M., Ribas I., Paredes J. M., Herrero A., Simón-Díaz S., 2014, Nature, 505, 378

Charles P. A., Coe M. J., 2006, Optical, ultraviolet and infrared observations of X-ray binaries. pp 215–265

Chaty S., Fortin F., García F., Fogantini F., 2019, in Oskinova L. M., Bozzo E., Bulik T., Gies D. R., eds, IAU Symposium Vol. 346, IAU Symposium. pp 161–169

Chen K., Ruderman M., 1993, ApJ, 402, 264

Coe M. J., Edge W. R. T., Galache J. L., McBride V. A., 2005, MNRAS, 356, 502

Coe M. J., Finger M., Bartlett E. S., Udalski A., 2015, MNRAS, 447, 1630

Coe M. J., Kirk J., 2015, MNRAS, 452, 969

Cole A. A., 2005, in American Astronomical Society Meeting Abstracts. p. 132.06

Cordes J. M., Romani R. W., Lundgren S. C., 1993, Nature, 362, 133

Crause L. A. et al., 2016, SpUpNIC (Spectrograph Upgrade: Newly Improved Cassegrain) on the South African Astronomical Observatory's 74-inch telescope. p. 990827

Crawford E. J., Filipović M. D., McEntaffer R. L., Brantseg T., Heitritter K., Roper Q., Haberl F., Urošević D., 2014, AJ, 148, 99

Crawford F., Kaspi V. M., Manchester R. N., Lyne A. G., Camilo F., D'Amico N., 2001, ApJ, 553, 367

Crawford S. M. et al., 2010, PySALT: the SALT science pipeline. p. 773725

Crowl H. H., Sarajedini A., Piatti A. E., Geisler D., Bica E., Clariá J. J., Santos João F. C. J., 2001, AJ, 122, 220

de Kool M., 1990, ApJ, 358, 189

de Kool M., van den Heuvel E. P. J., Pylyser E., 1987, A&A, 183, 47

Diaz J., Bekki K., 2011, MNRAS, 413, 2015

Diaz J. D., Bekki K., 2012, ApJ, 750, 36

Dickey J. M., Lockman F. J., 1990, ARA&A, 28, 215

Dopita M. A., Tuohy I. R., Mathewson D. S., 1981, ApJ, 248, L105

Dray L. M., 2006, MNRAS, 370, 2079

Dubus G., 2013, A&A Rev., 21, 64

Dubus G., Guillard N., Petrucci P.-O., Martin P., 2017, A&A, 608, A59

Duchêne G., Kraus A., 2013, ARA&A, 51, 269

Eldridge J. J., Langer N., Tout C. A., 2011, MNRAS, 414, 3501

Evans C. J., Howarth I. D., Irwin M. J., Burnley A. W., Harries T. J., 2004, MNRAS, 353, 601

Evans C. J., van Loon J. T., Hainich R., Bailey M., 2015, A&A, 584, A5

Fabregat J., Torrejón J. M., 2000, A&A, 357, 451

Faucher-Giguère C.-A., Kaspi V. M., 2006, ApJ, 643, 332

Filipović M. D. et al., 2008, A&A, 485, 63

Filipović M. D., Payne J. L., Reid W., Danforth C. W., Staveley-Smith L., Jones P. A., White G. L., 2005, MNRAS, 364, 217

Frew D. J., Parker Q. A., 2010, Publ. Astron. Soc. Australia, 27, 129

Fryer C. L., Kalogera V., 2001, ApJ, 554, 548

Fu L., Li X.-D., 2012, ApJ, 757, 171

Gaensler B. M., Slane P. O., 2006, ARA&A, 44, 17

Georgy C., Meynet G., Walder R., Folini D., Maeder A., 2009, A&A, 502, 611

Gies D. R., Bolton C. T., 1986, ApJ, 304, 371

Goldreich P., Julian W. H., 1969, ApJ, 157, 869

González-Galán A., Oskinova L. M., Popov S. B., Haberl F., Kühnel M., Gallagher J., Schurch M. P. E., Guerrero M. A., 2018, MNRAS, 475, 2809

Gorham P. W., Ray P. S., Anderson S. B., Kulkarni S. R., Prince T. A., 1996, ApJ, 458, 257

Graczyk D. et al., 2014, ApJ, 780, 59

Green D. A., 2014, Bulletin of the Astronomical Society of India, 42, 47

Grimm H. J., Gilfanov M., Sunyaev R., 2003, MNRAS, 339, 793

Gunn J. E., Ostriker J. P., 1970, ApJ, 160, 979

Gurevich A. V., Istomin Y. N., 2007, MNRAS, 377, 1663

Gvaramadze V. V., Kniazev A. Y., Oskinova L. M., 2019, MNRAS, 485, L6

Haberl F., Dennerl K., Pietsch W., 2003, A&A, 406, 471

Haberl F., Pietsch W., 1999, A&AS, 139, 277

Haberl F., Pietsch W., 2004, A&A, 414, 667

Haberl F., Sturm R., 2016, A&A, 586, A81

Haberl F. et al., 2012, A&A, 545, A128

Habets G. M. H. J., 1986, A&A, 167, 61

Harris J., Zaritsky D., 2002, StarFISH: A Robust Synthetic Color-Magnitude Diagram Package. p. 600

Harris J., Zaritsky D., 2004, AJ, 127, 1531

Harris J., Zaritsky D., 2009, AJ, 138, 1243

Haschke R., Grebel E. K., Duffau S., 2011, AJ, 141, 158

Heger A., Fryer C. L., Woosley S. E., Langer N., Hartmann D. H., 2003, ApJ, 591, 288

Heggie D. C., 1975, MNRAS, 173, 729

Hénault-Brunet V. et al., 2012, MNRAS, 420, L13

Hewish A., Bell S. J., Pilkington J. D. H., Scott P. F., Collins R. A., 1968, Nature, 217, 709

Ho W. C. G., Andersson N., 2017, MNRAS, 464, L65

Hobbs G., Lorimer D. R., Lyne A. G., Kramer M., 2005, MNRAS, 360, 974

Huang S.-S., 1963, ApJ, 138, 471

Hughes J. P., Smith R. C., 1994, AJ, 107, 1363

Hutchings J. B., Crampton D., Cowley A. P., 1983, ApJ, 275, L43

Hutchings J. B., Crampton D., Cowley A. P., Bianchi L., Thompson I. B., 1987, AJ, 94, 340

Ikhsanov N. R., 2012, MNRAS, 424, L39

Illarionov A. F., Sunyaev R. A., 1975, A&A, 39, 185

Israel G. L. et al., 2000, ApJ, 531, L131

Ivanova N. et al., 2013, A&A Rev., 21, 59

Janka H.-T., 2012, Annual Review of Nuclear and Particle Science, 62, 407

Jansen F. et al., 2001, A&A, 365, L1

Johnston S., Manchester R. N., Lyne A. G., Bailes M., Kaspi V. M., Qiao G., D'Amico N., 1992, ApJ, 387, L37

Kahabka P., 2002, A&A, 388, 100

Kaper L., 2001, High-Mass X-Ray Binaries and OB-runaway Stars. p. 125

Kaspi V. M., Helfand D. J., 2002, Constraining the Birth Events of Neutron Stars. p. 3

Kaspi V. M., Johnston S., Bell J. F., Manchester R. N., Bailes M., Bessell M., Lyne A. G., D'Amico N., 1994, ApJ, 423, 44

Kaspi V. M., Manchester R. N., Johnston S., Lyne A. G., D'Amico N., 1996, AJ, 111, 2028

Keane E. F., Kramer M., 2008, MNRAS, 391, 2009

Keith M. J. et al., 2010, MNRAS, 409, 619

Keller S. C., Bessell M. S., Da Costa G. S., 2000, Be Stars in the Magellanic Clouds. p. 75

Kennel C. F., Coroniti F. V., 1984, ApJ, 283, 694

Kennicutt Robert C. J., 1989, ApJ, 344, 685

Knigge C., Coe M. J., Podsiadlowski P., 2011, Nature, 479, 372

Kobulnicky H. A., Fryer C. L., 2007, ApJ, 670, 747

Kouwenhoven M. B. N., Brown A. G. A., Portegies Zwart S. F., Kaper L., 2007, A&A, 474, 77

Kramer M., Xilouris K. M., Lorimer D. R., Doroshenko O., Jessner A., Wielebinski R., Wolszczan A., Camilo F., 1998, ApJ, 501, 270

Krimm H. A. et al., 2009, The Astronomer's Telegram, 2011, 1

Kroupa P., 2001, MNRAS, 322, 231

Lai D., 2001, Neutron Star Kicks and Asymmetric Supernovae. p. 424

Leahy D. A., Leahy J. C., 2015, Computational Astrophysics and Cosmology, 2, 4

Lee J.-J., Park S., Hughes J. P., Slane P. O., Burrows D. N., 2011, ApJ, 731, L8

Lehmer B. D. et al., 2019, ApJS, 243, 3

Leonard P. J. T., Hills J. G., Dewey R. J., 1994, ApJ, 423, L19

Linden T., Kalogera V., Sepinsky J. F., Prestwich A., Zezas A., Gallagher J. S., 2010, ApJ, 725, 1984

Linden T., Sepinsky J. F., Kalogera V., Belczynski K., 2009, ApJ, 699, 1573

Lipunov V. M., 1992, Astrophysics of Neutron Stars

Liu J. et al., 2019, Nature, 575, 618

Liu Q. Z., van Paradijs J., van den Heuvel E. P. J., 2005, A&A, 442, 1135

Livio M., Soker N., 1988, ApJ, 329, 764

Loren R. B., Vanden Bout P. A., Davis J. H., 1973, ApJ, 185, L67

Lorimer D. R., Bailes M., Dewey R. J., Harrison P. A., 1993, MNRAS, 263, 403

Lorimer D. R. et al., 2006, MNRAS, 372, 777

Lorimer D. R., Kramer M., 2012, Handbook of Pulsar Astronomy

Lorimer D. R., Lyne A. G., Camilo F., 1998, A&A, 331, 1002

Luck R. E., Moffett T. J., Barnes Thomas G. I., Gieren W. P., 1998, AJ, 115, 605

Lyne A. G., Lorimer D. R., 1994, Nature, 369, 127

Lyne A. G., Manchester R. N., 1988, MNRAS, 234, 477

Lyne A. G., Ritchings R. T., Smith F. G., 1975, MNRAS, 171, 579

Lyne A. G., Stappers B. W., Keith M. J., Ray P. S., Kerr M., Camilo F., Johnson T. J., 2015, MNRAS, 451, 581

McMahon P., 2008, Msc., University of Cape Town

Maggi P. et al., 2019, A&A, 631, A127

Maggi P. et al., 2016, A&A, 585, A162

Maggi P., Haberl F., Sturm R., Pietsch W., Rau A., Greiner J., Udalski A., Sasaki M., 2013, A&A, 554, A1

Maitra C., Ballet J., Filipović M. D., Haberl F., Tiengo A., Grieve K., Roper Q., 2015, A&A, 584, A41

Maitra C. et al., 2019, MNRAS, 490, 5494

Manchester R. N., Fan G., Lyne A. G., Kaspi V. M., Crawford F., 2006, ApJ, 649, 235

Manchester R. N., Hobbs G. B., Teoh A., Hobbs M., 2005, VizieR Online Data Catalog, p. VII/245

Manchester R. N. et al., 2001, MNRAS, 328, 17

Manousakis A., Walter R., Audard M., Lanz T., 2009, A&A, 498, 217

Maravelias G., Zezas A., Antoniou V., Hatzidimitriou D., 2014, MNRAS, 438, 2005

Marshall F. E., Gotthelf E. V., Zhang W., Middleditch J., Wang Q. D., 1998, ApJ, 499, L179

Masetti N. et al., 2006, A&A, 459, 21

Massi M., Migliari S., Chernyakova M., 2017, MNRAS, 468, 3689

McBride V. A., Coe M. J., Negueruela I., Schurch M. P. E., McGowan K. E., 2008, MNRAS, 388, 1198

McConnell D., McCulloch P. M., Hamilton P. A., Ables J. G., Hall P. J., Jacka C. E., Hunt A. J., 1991, MNRAS, 249, 654

McCulloch P. M., Hamilton P. A., Ables J. G., Hunt A. J., 1983, Nature, 303, 307

McSwain M. V., Gies D. R., 2005, ApJS, 161, 118

Meixner M. et al., 2006, AJ, 132, 2268

Mineo S., Gilfanov M., Lehmer B. D., Morrison G. E., Sunyaev R., 2014, MNRAS, 437, 1698

Mineo S., Gilfanov M., Sunyaev R., 2012, MNRAS, 419, 2095

Moe M., Di Stefano R., 2017, ApJS, 230, 15

Moriya T. J. et al., 2017, MNRAS, 466, 2085

Negueruela I., Coe M. J., 2002, A&A, 385, 517

Nelemans G., Verbunt F., Yungelson L. R., Portegies Zwart S. F., 2000, A&A, 360, 1011

Nelemans G., Yungelson L. R., Portegies Zwart S. F., Verbunt F., 2001, A&A, 365, 491

Orosz J. A., McClintock J. E., Aufdenberg J. P., Remillard R. A., Reid M. J., Narayan R., Gou L., 2011, ApJ, 742, 84

Pacini F., Salvati M., 1973, ApJ, 186, 249

Packet W., 1981, A&A, 102, 17

Paczynski B., 1976, in Eggleton P., Mitton S., Whelan J., eds, IAU Symposium Vol. 73, Structure and Evolution of Close Binary Systems. p. 75

Padmanabhan T., 2001, Theoretical Astrophysics, Volume 2: Stars and Stellar Systems

Paredes J. M., Bordas P., 2019, arXiv e-prints, p. arXiv:1902.09898

Pavlovskii K., Ivanova N., Belczynski K., Van K. X., 2017, MNRAS, 465, 2092

Payne J. L., White G. L., Filipović M. D., Pannuti T. G., 2007, MNRAS, 376, 1793

Pfahl E., Rappaport S., Podsiadlowski P., Spruit H., 2002, ApJ, 574, 364

Pietrzyński G. et al., 2019, Nature, 567, 200

Podsiadlowski P., Cannon R. C., Rees M. J., 1995, MNRAS, 274, 485

Podsiadlowski P., Langer N., Poelarends A. J. T., Rappaport S., Heger A., Pfahl E., 2004, ApJ, 612, 1044

Poelarends A. J. T., 2007, PhD thesis, Utrecht University

Portegies Zwart S. F., Verbunt F., 1996, A&A, 309, 179

Portegies Zwart S. F., Yungelson L. R., 1998, A&A, 332, 173

Porter J. M., Rivinius T., 2003, PASP, 115, 1153

Pringle J. E., Rees M. J., 1972, A&A, 21, 1

Proszynski M., Przybycien D., 1984, in Reynolds S. P., Stinebring D. R., eds, Birth and Evolution of Neutron Stars: Issues Raised by Millisecond Pulsars. p. 151

Raghavan D. et al., 2010, ApJS, 190, 1

Ransom S. M., Eikenberry S. S., Middleditch J., 2002, ApJ, 124, 1788

Ravi V. et al., 2016, Science, 354, 1249

Rees M. J., Gunn J. E., 1974, MNRAS, 167, 1

Ridley J. P., Crawford F., Lorimer D. R., Bailey S. R., Madden J. H., Anella R., Chennamangalam J., 2013, MNRAS, 433, 138

Ridley J. P., Lorimer D. R., 2010, MNRAS, 406, L80

Rivinius T., Carciofi A. C., Martayan C., 2013, A&A Rev., 21, 69

Roper Q., McEntaffer R. L., DeRoo C., Filipovic M., Wong G. F., Crawford E. J., 2015, ApJ, 803, 106

Ruderman M. A., Sutherland P. G., 1975, ApJ, 196, 51

Safi-Harb S., Ogelman H., Finley J. P., 1995, ApJ, 439, 722

Sana H. et al., 2012, in Drissen L., Robert C., St-Louis N., Moffat A. F. J., eds, Astronomical Society of the Pacific Conference Series Vol. 465, Proceedings of a Scientific Meeting in Honor of Anthony F. J. Moffat. p. 284

Sana H. et al., 2014, ApJS, 215, 15

Seward F. D., Harnden F. R. J., Helfand D. J., 1984, ApJ, 287, L19

Seward F. D., Mitchell M., 1981, ApJ, 243, 736

Shattow G., Loeb A., 2009, MNRAS, 392, L21

Shtykovskiy P., Gilfanov M., 2005, A&A, 431, 597

Skrutskie M. F. et al., 2006, AJ, 131, 1163

Smith R. C., MCELS Team 1999, in Chu Y.-H., Suntzeff N., Hesser J., Bohlender D., eds, IAU Symposium Vol. 190, New Views of the Magellanic Clouds. p. 28

Staelin D. H., 1969, in IEEE Proceedings. p. 724

Stanimirovic S., Staveley-Smith L., Dickey J. M., Sault R. J., Snowden S. L., 1999, MNRAS, 302, 417

Staveley-Smith L. et al., 1996a, Publ. Astron. Soc. Australia, 13, 243

Staveley-Smith L. et al., 1996b, Publ. Astron. Soc. Australia, 13, 243

Strüder L. et al., 2001, A&A, 365, L18

Sturm R. et al., 2013, A&A, 558, A3

Sturrock P. A., 1971, ApJ, 164, 529

Sukhbold T., Ertl T., Woosley S. E., Brown J. M., Janka H. T., 2016, ApJ, 821, 38

Suwa Y., Yoshida T., Shibata M., Umeda H., Takahashi K., 2015, MNRAS, 454, 3073

Talbot R. J. J., 1980, ApJ, 235, 821

Tauris T. M. et al., 2017, ApJ, 846, 170

Tauris T. M., Langer N., Moriya T. J., Podsiadlowski P., Yoon S. C., Blinnikov S. I., 2013, ApJ, 778, L23

Tauris T. M., Langer N., Podsiadlowski P., 2015, MNRAS, 451, 2123

Tauris T. M., Manchester R. N., 1998, MNRAS, 298, 625

Titus N. et al., 2019, MNRAS, 487, 4332

Toonen S., Nelemans G., 2013, A&A, 557, A87

Toonen S., Nelemans G., Portegies Zwart S., 2012, A&A, 546, A70

Townsend L. J., Coe M. J., Corbet R. H. D., Hill A. B., 2011, MNRAS, 416, 1556

Turner M. J. L. et al., 2001, A&A, 365, L27

Tutukov A., Yungelson L., 1973, Nauchnye Informatsii, 27, 70

Udalski A., Szymański M. K., Szymański G., 2015, Acta Astron., 65, 1

Vagnozzi S., 2017, arXiv e-prints, p. arXiv:1703.10834

van den Heuvel E. P. J., 1976, Mem. Soc. Astron. Italiana, 47, 453

van den Heuvel E. P. J., 2004, in Schoenfelder V., Lichti G., Winkler C., eds, ESA Special Publication Vol. 552, 5th INTEGRAL Workshop on the INTEGRAL Universe. p. 185

van den Heuvel E. P. J., Portegies Zwart S. F., de Mink S. E., 2017, MNRAS, 471, 4256

van der Heyden K. J., Bleeker J. A. M., Kaastra J. S., 2004, A&A, 421, 1031

van Dokkum P. G., 2001, PASP, 113, 1420

van Haaften L. M., Nelemans G., Voss R., van der Sluys M. V., Toonen S., 2015, A&A, 579, A33

van Heerden E., Karastergiou A., Roberts S. J., 2017, MNRAS, 467, 1661

Vanderplas J., , 2015, Gatspy: General Tools For Astronomical Time Series In Python

Vasilopoulos G., Haberl F., Delvaux C., Sturm R., Udalski A., 2016, MNRAS, 461, 1875

Vasilopoulos G., Maitra C., Haberl F., Hatzidimitriou D., Petropoulou M., 2018, MNRAS, 475, 220

Verbunt F., Igoshev A., Cator E., 2017, A&A, 608, A57

Vivekanand M., Narayan R., 1981, Journal of Astrophysics and Astronomy, 2, 315

Vogt F. P. A., Bartlett E. S., Seitenzahl I. R., Dopita M. A., Ghavamian P., Ruiter A. J., Terry J. P., 2018, Nature Astronomy, 2, 465

Walborn N. R., Fitzpatrick E. L., 1990, PASP, 102, 379

Walborn N. R. et al., 2014, A&A, 564, A40

Walker A. R., 2012, Ap&SS, 341, 43

Walter R., Lutovinov A. A., Bozzo E., Tsygankov S. S., 2015, A&A Rev., 23, 2

Wang N., Johnston S., Manchester R. N., 2004, MNRAS, 351, 599

Wang Q., Helfand D. J., 1991, in Haynes R., Milne D., eds, IAU Symposium Vol. 148, The Magellanic Clouds. p. 224

Webbink R. F., 1984, ApJ, 277, 355

Wong T., Blitz L., 2002, ApJ, 569, 157

Yokogawa J., Imanishi K., Tsujimoto M., Nishiuchi M., Koyama K., Nagase F., Corbet R. H. D., 2000, ApJS, 128, 491

Yoon S. C., Woosley S. E., Langer N., 2010, ApJ, 725, 940

Yusof N. et al., 2013, MNRAS, 433, 1114

Zaritsky D., Harris J., Thompson I. B., Grebel E. K., 2004, AJ, 128, 1606

Zaritsky D., Harris J., Thompson I. B., Grebel E. K., Massey P., 2002, AJ, 123, 855

Zhang X., Lin D. N. C., Burkert A., Oser L., 2012, ApJ, 759, 99

Zombeck M. V., 1990, Handbook of space astronomy and astrophysics

Zorec J., Briot D., 1997, A&A, 318, 443

Zorotovic M., Schreiber M. R., Gänsicke B. T., Nebot Gómez-Morán A., 2010, A&A, 520, A86

Zorotovic M., Schreiber M. R., García-Berro E., Camacho J., Torres S., Rebassa-Mansergas A., Gänsicke B. T., 2014, A&A, 568, A68